ROBOTIC IMPLANT MODIFICATION FOR NEUROPLASTIC SURGERY

by

Shuya (Joshua) Liu

A dissertation submitted to Johns Hopkins University in conformity with the requirements for the degree of Doctor of Philosophy

Baltimore, Maryland

August, 2021

Abstract

Neuroplastic surgery, which combines neurosurgery with plastic surgery, is a novel field that has not been rigorously studied. It has crucial clinical potentials in implanting instrumented devices for brain imaging, targeted drug delivery, deep brain stimulation, shunt placement, and so on. A specific application of neuroplastic surgery is single-stage cranioplasty. Current practice involves resizing a prefabricated oversized customized cranial implant (CCI). This method provides intraoperative flexibility for skull resection. However, surgeons need to manually resize the CCI to fit the craniofacial bone defect based on their judgment and estimation. This manual modification can be time-consuming and imprecise, resulting in large bone gaps between the skull and the resized implant. This work investigates the possibility of applying robotic and computer-integrated techniques to improve the procedure.

This dissertation describes the development and examination of several systems to address the challenges that emerged from the CCI resizing process: (i) To assist the manual modification, a portable projection mapping device (PPMD) provides precise real-time visual guidance for surgeons to outline the defect boundary on the oversized CCI. (ii) Even with the assistance of a projection system, the subsequent manual resizing may still be imprecise

and prone to failure. This work introduces an automated workflow for intraoperative CCI modification using a robotic system. (iii) A 2-scan method accomplishes the patient-to-CT registration using a handheld 3D scanner, and addresses the challenges posed by the soft tissues and the surgical draping requirement using reattachable fiducial markers. (iv) A toolpath algorithm generates a cutting toolpath for the robot to resize the implant based on the defect geometry. (v) Due to certain limitations associated with mechanical cutting, this work presents a 5-axis CO_2 laser cutting system that achieves fast and precise implant modification, ideal for fabricating instrumented implants.

The evaluation of the automated workflow shows a significant improvement in CCI resizing accuracy. This indicates lower risk of implant failure causing post-surgical complications. Furthermore, the functions provided by these systems can be expanded to other neuroplastic applications.

Primary Reader and Advisor

Mehran Armand
Professor
Department of Orthopedic Surgery and Mechanical Engineering
Johns Hopkins University

Secondary Readers

Axel Krieger
Assistant Professor
Department of Mechanical Engineering
Johns Hopkins University

Chad Gordon
Professor
Department of Plastic and Reconstructive Surgery
Johns Hopkins University School of Medicine

Acknowledgments

The research described in this dissertation would not be possible without the numerous supports I have received from many people. I want to first express my tremendous gratitude to my advisor, Dr. Mehran Armand, for his enormous support and guidance throughout my PhD years. He has provided me the precious opportunity to learn many new things and taught me many crucial research skills.

I also wish to sincerely thank Dr. Axel Krieger for graciously accepting to be on my defense committee and for dedicating his time to reading this dissertation. Special thanks to Dr. Chad Gordon, the pioneer of neuroplastic surgery, for his clinical insights and dedication, which motivated me to identify the challenges in this field and dedicate myself to improving this procedure using computer-integrated and robotic technologies. Also, many thanks to Dr. Russell Taylor of the Department of Computer Science for his remarkable suggestions to this work during the Biomechanical and Image-Guided Surgical Systems (BIGSS) Laboratory group meetings.

Many thanks go to Wei-Lun Huang, who has closely collaborated with me and contributed to the development of this work. At the same time, I would also like to thank the current and former lab members, Justin Ma,

Cong Gao, Mahsan Bakhtiarinejad, Alireza Chamani, Henry Phalen, Yihao Liu, Golchehr Amirkhani, Dr. Amirhossein Farvardin, Dr. Shahriar Sefati, Dr. Farshid Alambeigi, Dr. Robert Grupp, Dr. Ryan Murphy, Jerry Fang, Austin Shin, and members from other labs, Dr. Jiaxiang Tao, Rick Han, Sing Chun Lee, Alejandro Martin-Gomez, and Wenhao Gu, for their support and help.

I also want to recognize Davood Tashayyod of Lumo Imaging, Dr. Nati Ben-Shalom of Neuroplastic and Reconstructive Surgery, Dr. Iulian Iordachita of Mechanical Engineering, and Demetries Boston of Johns Hopkins Bayview Medical Center for their generous help and support on my research.

Most importantly, I want to give thanks to my Lord and Savior Jesus, who gives me life, watches over me, and leads me all the way. I want to thank my dear brothers and sisters at Worthy Life Baptist Church for caring for me as a family. I want to especially express gratitude to my pastors, Pastor Peter Lee, Pastor James Lee, and Pastor James Kim, for their prayers and concrete guidance in my life.

Lastly but certainly not least, words cannot express my deep gratitude to my loving parents. They have raised me, accompanied me, and provided for me in every aspect of my life. I will not be here today without their love and sacrifice.

Shuya (Joshua) Liu

August 2021

Table of Contents

List of Tables

List of Figures

List of Acronyms

AR	Augmented Reality
CAD/CAM	Computer-aided Design/Manufacturing
CCI	Customized Cranial Implant
CT	Computed Tomography
DoF	Degree of Freedom
ETS	Electromagnetic Tracking Systems
GUI	Graphic User Interface
HMD	Head-mounted Display
ICP	Iterative Closest Point
OTS	Optical Tracking System
PEEK	Polyether Ether Ketone
PMMA	Poly Methyl Methacrylate
PPMD	Portable Projection Mapping Device
RMS	Root Mean Square
ROS	Robotic Operating System
SAR	Spatical Augmented Reality
TCP	Tool Center Point
TSDF	Truncated Signed Distance Function

Chapter 1

Introduction

1.1 Motivation

Patients undergoing neurosurgical procedures are usually left with permanent deformities on their skulls, face, scalp dura and so on. To fix these deformities, patients usually need neuroplastic surgery during which surgeons utilizes synthetic and bio-compatible materials, such as Poly Methyl Methacrylate (PMMA) or Polyether Ether Ketone (PEEK), to replace the bone at the defected area [1, 2]. Neuroplastic surgery is also useful for implanting medical devices for targeted drug delivery, deep brain stimulation, shunt placement and so on [3]. A specific application of neuroplastic surgery is cranioplasty, which focuses on skull reconstruction [4, 5].

The main challenge for cranioplasty is the unknown skull resection. Usually, after craniotomy, autologous bones are often discarded because of osteomyelitis, tumor, or resorption. Therefore, surgeons usually repair skull

defects using Customized Cranial Implants (CCIs) [6–8]. Due to the unknown skull resection, the traditional procedure usually requires an additional surgery after the initial neurosurgery, during which the bone flap is removed [9]. The surgeon needs to work with an implant manufacturer using Computer-aided Design/Manufacturing (CAD/CAM) techniques to design a patient-specific CCI. The generated CCI, matching the patient's original skull resection geometry, then fills the bony voids in the cranial skeleton during the second surgery.

To simplify the procedure and minimize the risk of prolonged brain exposure, single-stage cranioplasty, which comes up with an appropriate CCI immediately after the skull resection, has become clinically more desirable [10, 11]. One conventional approach is to perform intraoperative modification of a prefabricated oversized CCI immediately following craniotomy [12]. However, the current approach requires a surgeon to manually resize an oversized CCI based on his/her judgment and estimation of a cranial defect's shape, which can be imprecise and often time-consuming. This can result in large bone gaps, which may cause post-surgical complications. Therefore, precisely and efficiently resizing the oversized CCI has become a major challenge.

This dissertation details a number of systems developed to improve the CCI resizing accuracy. An Augmented Reality (AR) based projection system is first developed to help surgeons accurately outline the boundary of the defect on the oversized CCI. However, this approach still depends on individual surgeon's skill to manually resize CCIs. As medical robots are rapidly transforming conventional surgical procedures, a robotic workstation is developed

to automate and improve the resizing accuracy of the intraoperative CCI modification. While the developed robotic system demonstrates higher resizing accuracy than the manual approach, many drawbacks emerged from using mechanical cutter, such as the limited robot workspace, creating noise/dust, and incapability of cutting smooth and sharp edges. Therefore, a 5-axis laser cutting system is designed and developed for precise CCIs resizing without direct contact, reducing the risk of any contamination.

3D scanning is our primary approach used in acquiring defect geometry alongside the optical tracking method. A key factor determining the resizing accuracy of these systems is associated with the accuracy of the registrations between different 3D spaces: 1) the patient space, containing the defect geometry; 2) the CT space, containing the original CCI; 3) the spaces containing the physical CCI, which can be projector space, robot space or the laser space. This registration procedure has been extensively used throughout this dissertation. The experimental tests showed that these developed systems have considerably improved the resizing accuracy and provided faster CCI modification compared to the manual method. Because of the accurate registration method, the robotic and laser cutting systems described in this dissertation can give accurate CCI resizing regardless of the complexity of the local skull geometry.

1.2 Objectives and Scope

The goal of this research is to develop surgical systems for fast and precise CCI resizing, and to provide new techniques for single-stage skull reconstruction. While this research focuses on single-stage cranioplasty, the developed

systems may apply to a variety of surgical procedures as discussed in the following Chapters.

As mentioned in the previous section, the accuracy of intraoperative modification of an oversized CCI depends on a surgeon's estimation of defect geometry. This is often imprecise and results in large bone gaps between the resized implant and the defect. To visually guide the surgeon during this process, we introduce a Portable Projection Mapping Device (PPMD). The PPMD consists of a real-time Optical Tracking System (OTS) with sub-millimeter tracking accuracy that can track multiple digitizing instruments and reference markers attached on the skull. After performing patient-to-CT registration utilizing the anatomical features, the surgeon outlines the skull resection area with a digitizing instrument to acquire the defect boundary. The defect boundary is then projected directly on the oversized CCI to guide the subsequent manual modification. The proposed PPMD and its associated pipeline enable intraoperative CCI modification with 3D projection feedback to surgeons for the very first time.

The PPMD system is also applicable to many other medical AR applications when projection mapping is preferred over wearable Head-mounted Displays (HMDs). Nevertheless, this technique only provides visual feedback, as it still relies on surgeons to perform the manual cutting. To automate the cutting process, a robotic system is developed to achieve automated and more precise CCI resizing. The system utilizes 3D scanning technique to acquire a patient's defect geometry. Based on the acquired defect information, a cutting toolpath is generated for the robot to automatically resize the oversized CCI

to fit the skull defect. The preliminary experiments on partial plastic skulls demonstrated higher resizing accuracy by the developed system compared to an expert surgeon's performance.

The preliminary success of the robotic system implies its clinical values in future single-stage cranioplasty. To emphasize its practical significance, the system is further developed to address the registration challenge in clinical settings when soft tissues exist and surgical draping is required. A 2-scan method is proposed for patient-to-CT registration using reattachable fiducial markers. First, prior to draping, the patient's head is 3D scanned with markers attached on the skin. After skull resection, the defect geometry is acquired by performing another 3D scanning. Although the drape would only leave the surgical site visible, the key to successful patient-to-CT registration is the designed markers that could be repeatedly reattached at the same locations above the drape. Next, the toolpath algorithm generates a robot cutting toolpath based on the 3D scanned defect model considering the defect's beveled edge. Lastly, the robot performs robotic 3D scanning to localize the implant and automatically resizes the implant to match the size of the defect. We evaluated the implant resizing accuracy of the proposed paradigm against the resizing accuracy of the manual approach by an expert surgeon on plastic skulls and cadavers. The results showed that the proposed system significantly decreased the bone gap distance between the resized CCI and the defect, indicating lower risk of post-surgical complication and more satisfied aesthetic restoration.

The proposed robotic system shows promise for clinical applications. However, the mechanical cutting system has certain limitations, as mentioned above. Moreover, mechanical cutters may cause contamination if not properly sterilized. To address these challenges posed by the mechanical cutting system, a 5-axis CO_2 laser cutting system is developed. It is also discovered that laser cutting can provide an even higher accuracy than the robotic cutting system, under the similar registration method. The author's registration method, combined with the accurate laser cutting system has shown great potential in various neuroplastic applications, such as non-screw fixation, fabricating instrumented implants.

1.3 Thesis Overview

In this work, the author describes the developed AR and automated systems. With extensive design and testing, it is demonstrated that the proposed automated workflow for single-stage cranioplasty significantly improves the resizing accuracy over the conventional workflow. The breakdown for each Chapter is described as follows:

Chapter 2 provides the reader an overview of the clinical background associated with single-stage cranioplasty. A selected number of relevant literature are reviewed describing the progress of different methods used in single-stage cranioplasty. Based on the current research, the major shortcomings of the existing techniques for CCI resizing is identified.

A novel Portable Projection Mapping Device (PPMD) is presented in Chapter 3. The PPMD system integrates projection AR into clinical settings, allowing the surgeons to visualize the defect contour directly on the oversized CCI. Chapter 3 describes this system in detail and demonstrates its tracking and projection mapping accuracy. The PPMD system guides the surgeon to precisely outline the defect contour on the oversized CCI.

However, the system described in Chapter 3 still requires manual resizing. To automate the resizing process, a robotic workstation for resizing CCIs is developed and introduced in Chapter 4. The advantages of using 3D scanning to acquire precise defect geometry, and the key challenge of registering the defect to the implant is addressed. A toolpath algorithm is developed for generating robot's Tool Center Points (TCPs). The system is then tested on six partial skulls with defects generated at different locations. The resizing accuracy of the system compared to the conventional manual approach and the OTS approach is then evaluated and showed significant improvement resulting in smaller bone gaps between the resized CCI and the defect.

The robotic system developed in Chapter 4 indicates the potential of an automated CCI resizing process. However, the preliminary system was only tested on partial plastic skulls. The patient-to-CT registration with soft tissue was not addressed. Also, the draping requirement during the surgery makes the patient-to-CT registration by 3D scanning extremely difficult. Chapter 5 discusses further system improvement and addresses the registration challenge by using a 2-scan method and utilizing reattachable fiducial markers. The toolpath algorithm described in Chapter 4 is further improved, and a

robotic 3D scanning is implemented to localize the CCI automatically. We conducted cadaver tests to demonstrate the system's feasibility in clinical applications.

The test results from Chapter 4 and 5 demonstrated the potential value of the robotic system in clinical applications. Although the automated intra-operative CCI modification workflow produces higher resizing accuracy, the robot accomplishes the process via mechanical cutting tools. The mechanical cutter cannot cutting sharp edges while creating much noise and dust in the operating room. Therefore, Chapter 6 discusses the development of a 5-axis laser cutting system to provide faster and smoother cuttings. Preliminary tests by 3-axis demonstrated minimal bone gaps between the resized CCI and the defect, indicating improved skull reconstruction.

The laser cutting system has shown a more accurate, cleaner and faster CCI resizing compared to the robotic mechanical cutting. In Chapter 6, the kinematics of the 5-axis laser cutting system is analyzed. However, the test was done on a simple defect model that only required 3-axis cutting. A more complicated skull defect usually requires all 5-axis cutting to achieve a close fit between the skull and the resized CCI. Therefore, in Chapter 7, the author implements the full 5-axis control of the laser system to resize CCIs for more complicated defect geometries. The Chapter also introduces an implant localization method for registering regular implants to the system, eliminating the need of additional registration tabs to be designed on the implants. A higher power laser replacing the previous one achieves faster and more efficient cutting.

Chapter 8 concludes the work, summarizing all the developed systems and their clinical significance in improving neuroplastic surgery. The Chapter also describes the limitations of these studies and identifies future research to further expand and materialize their clinical applications.

1.4 Contributions

The author's contributions are summarized as follows:

- Development of a Portable Projection Mapping Device (PPMD) to provide medical Augmented Reality (AR) for surgical navigation and visual guidance, allowing surgeons to perform patient-to-CT registration and precisely outline the defect boundary on the oversized CCI.
- Development of an open-source optical tracking algorithm with Robotic Operating System (ROS) implementation to track multiple instruments within sub-millimeter tracking accuracy.
- Introducing a fast and non-contact approach for acquiring intraoperative cranial defect geometries using a handheld 3D scanner.
- Integration of a robotic system for intraoperative CCI modification.
- Introducing a modified Iterative Closest Point (ICP) algorithm for patient-to-CT registration that addresses the challenge posed by the soft tissues.
- Introducing a 2-scan method for registering the 3D scanned cranial defect model to the CT space using reattachable fiducial markers to

address the challenge posed by the surgical draping requirement in clinical scenarios.

- Development of a toolpath algorithm for generating robot cutting toolpath that defines the robot's TCPs to attain precise CCI resizing.
- Proposing an automated workflow for resizing oversized CCI, providing automatic implant localization functionality via robotic 3D scanning.
- Evaluation of the resizing accuracy of the developed systems by phantom and cadaver experiments, and compared the results to the conventional manual approach.
- Development of a 5-axis CO_2 laser cutting system for intraoperative CCI resizing.
- Demonstration of higher resizing accuracy using the developed systems than the conventional manual implant resizing, and their potential applications for neuroplastic surgery.

Chapter 2

Background

2.1 Motivation

This chapter intends to provide the readers with relevant background information for the following chapters. This chapter begins by introducing the conventional cranioplasty procedure and the more recent neuroplastic surgery. The second part of this chapter reviews some existing techniques for single-stage cranioplasty. However, many challenges arise while performing single-stage cranioplasty, which motivated the author to design and develop a series of medical devices and robotic systems to improve the procedure. The third part of this chapter lists the technical background about medical augmented reality and intraoperative data acquisition.

2.2 Medical Background

Neuroplastic surgery is a procedure to repair the bone defect in the craniofacial skeleton [1, 3]. A non-congenital cranial defect may result from trauma or a previous procedure. For instance, neurosurgery often requires craniotomy,

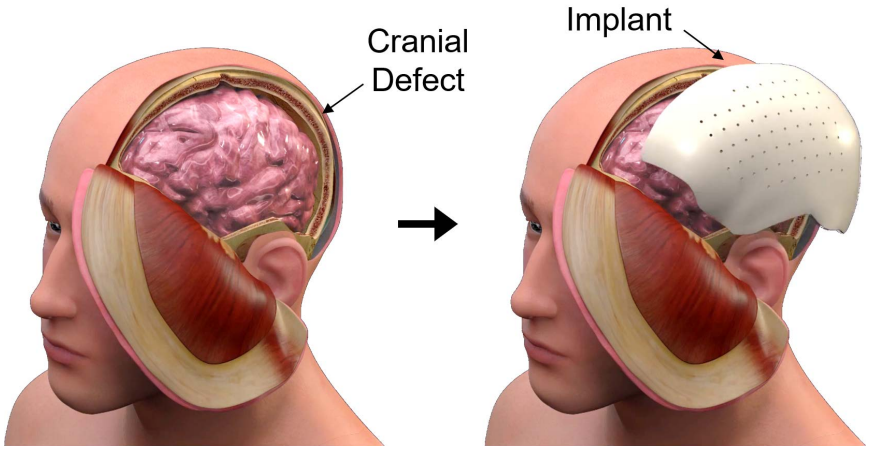

Figure 2.1: Cranioplasty with a patient-specific cranial implant Image courtesy of https://highimpact.com/exhibits/cranioplasty.

partial resection of the skull, for surgeons to gain access to the brain in order to diagnose or treat diseases such as tumors, aneurysms, epilepsy or infections. The surgery creates a bony void in the skull. Without the protection for the brain, the void poses a great risk of post-surgical brain injuries. Thus, a neuroplastic procedure such as cranioplasty is often desired to repair the skull deformities, restoring patients' aesthetics and neurological functions [5, 10].

Conventional cranioplasty reuses the patient's original bone if it remains functional or uses titanium mesh to cover the defect hole if the defect area is small [2]. An alternative approach is to perform delayed cranioplasty, in the case of decompressive craniectomy, using a patient-specific implant customized made from a bio-compatible synthetic material [9, 13, 14]. The customized implant is usually designed based on the patient's postoperative CT images to obtain an ideal match between the implant and the defect, as shown in Figure 2.1 [15]. While the customized implant mimics the same size and shape of the original skull, it requires a secondary surgery which leads

to longer recovery time and increases the risk of post-surgical infection [16]. Hence, single-stage cranioplasty is proposed as the technique of choice where possible [17].

Single-stage cranioplasty aims to repair skull deformities immediately following neurosurgical procedures within one single operation; therefore, decreasing operative times [11, 12]. The single-stage skull reconstruction has become more popular as it shortens the surgical and recovery time. The common practice of single-stage cranioplasty fills the skull defect using a prefabricated CCI, but challenges emerge in fitting the implant exactly to the defect in order to provide a perfect seal to the skull.

2.3 Related Work

With the fast development of CAD/CAM and Computed Tomography (CT), patient-specific alloplastic CCIs, customized-made from synthetic bio-materials have been widely used for skull reconstructions [18–20]. There are commonly three basic materials used for CCI fabrication: Titanium, Poly Methyl Methacrylate (PMMA), Polyether Ether Ketone (PEEK).

Titanium mesh is a metallic alloy that has a high strength. Studies have shown that CCI made of titanium has low risk of infection [21, 22]. But the material is expensive and causing artifacts on imaging [23, 24]. PMMA and PEEK are the two most widely materials used for alloplastic reconstruction. Overall, PMMA and PEEK have similar properties in terms of strength, and both materials can be customized in a patient-specific manner using CAD/CAM technique [25]. However, PEEK was only introduced recently, whereas PMMA

is more reliable as it has been used for CCI fabrication since 1940s even up to today [6, 26, 27]. In addition, patient-specific prefabricated CCIs made of PMMA are delivered sterile, directly to the operating room; CCIs made of PEEK require additional on-site sterilization [25, 28, 29].

Due to the long production time, CAD/CAM-based alloplastic CCIs have mainly been used for delayed cranioplasty. To achieve single-stage skull reconstruction, the patient-specific CCIs are prefabricated and sterilized so that the surgeons would receive the CCIs before the procedure. During the procedure, the surgeon then performs craniotomy in accordance to the size of the CCI.

Earlier practices of single-stage cranioplasty utilized a resection template to guide the skull resection to match a given CCI, as shown in Figure 2.2 [30, 31]. Robot-assisted craniotomy was also introduced to achieve precise skull resection [32]. Recent techniques adopted surgical navigation to assist surgeons to attain efficient and accurate skull resections [33–35]. It is worth noting that sometimes, the amount of bone removal may be revised during the surgery due to surgical needs. However, all the above-mentioned approaches are limited by the preoperative plan in order to match the size of a given implant, restricting any intraoperative plan change.

One method for flexible skull resection while achieving single-stage reconstruction is to form alloplastic CCIs intraoperatively using PMMA cement by pouring the resin into a mold created from the patient's autologous bone [36, 37]. Although this intraoperative molding technique is cost-effective, it is

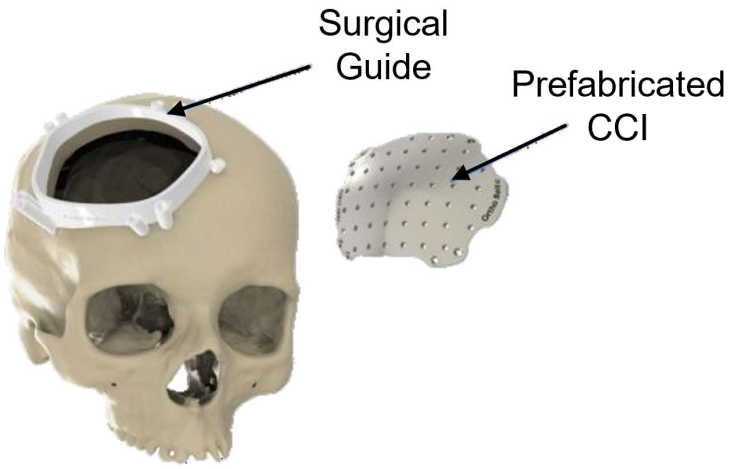

Figure 2.2: Craniotomy using a patient-specific surgical guide Image courtesy of http://balticimplants.eu/patient-specific-medical-devices/cranial-implants/.

time-consuming and unusable if the removed bone flaps are already contaminated with infections. Moreover, the exothermic reactions during the PMMA curing may cause allergic reactions. While additive manufacturing such as 3D printing has been widely used to generate CCIs, it is impractical to 3D print CCI during the surgery due to its long fabrication time and the sterilization requirement [38–40].

Another clinical approach for single-stage cranioplasty is to perform intraoperative manual modification of an oversized CCI to fit the skull defect [11, 12]. The oversized CCIs are prefabricated based on the patient's preoperative CT images that matches the 3D geometry of the original intact skull. During single-stage cranioplasty, the surgeon draws the defect contour with a marker pen directly on the prefabricated oversized CCI then trims the CCI to fit the size of the defect (Figure 2.3). However, it remains challenging for surgeons to gauge and to trace the cranial defect contour by eyeballing.

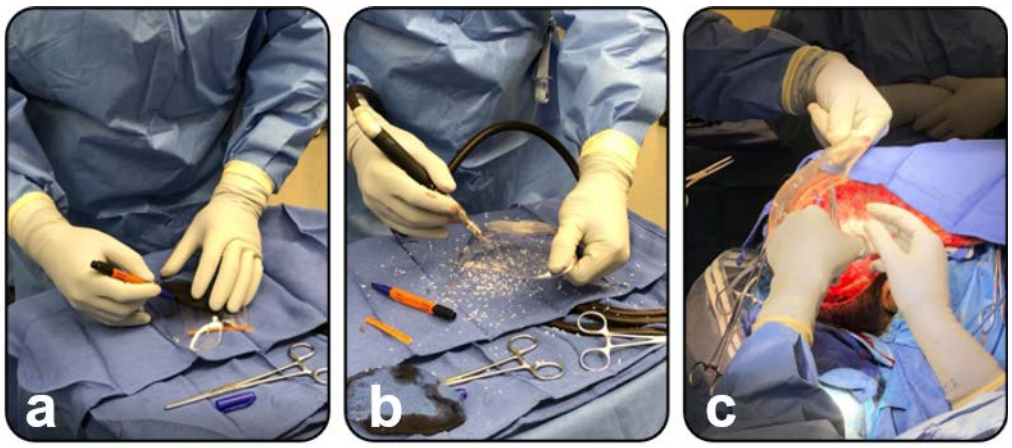

Figure 2.3: Intraoperative manual CCI modification a) The surgeon marks the defect contour on the oversized CCI. b) The surgeon manually trims the oversized CCI. c) The resized implant is fitted to the defect.

The imprecise defect contour estimation usually requires a surgeon to preform multiple iterations to resize the implant until it can roughly fit into the defect. The whole resizing procedure takes about 10-80 minutes [12]. Even after the implant is trimmed down to fit into the defect, it often results in large bone gaps due to over-cutting. A study shows that for pediatric cranioplasty a bone gap of > 6 *mm* results in significantly higher implant failure [41]. To minimize this risk, the large bone gaps are covered by additional thin titanium meshes. Although these titanium meshes mitigates implant failure in some degrees, it is not as durable as the actual CCI, which matches the original skull thickness.

To improve the accuracy of defect-contour tracing, surgeons can use a computer-assisted workstation to guide their manual modification of over-sized CCIs [42, 43]. This workstation identifies the region of the resected skull using an optical tracking navigation system, then projects the outline of the

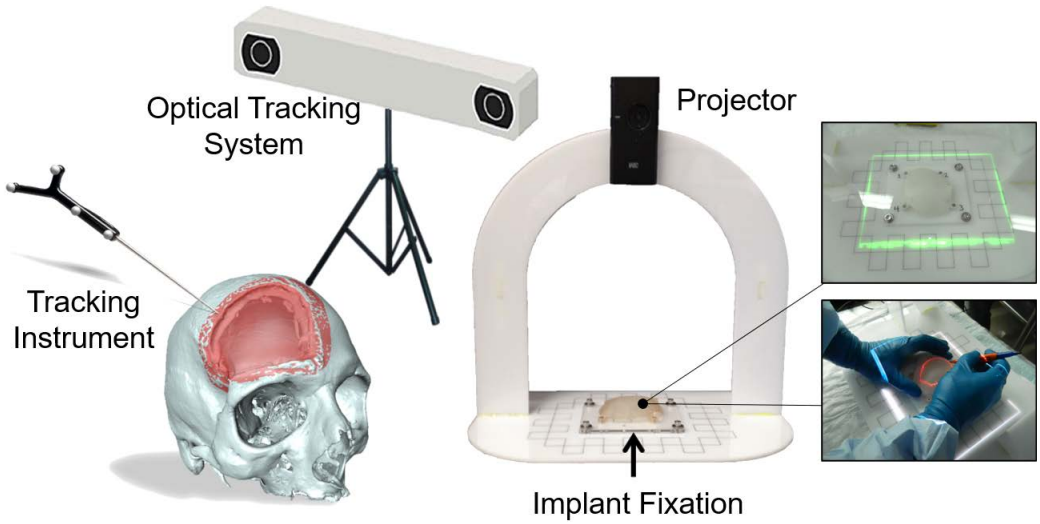

Figure 2.4: Computer-assisted single-stage cranioplasty The computer-assisted single-stage cranioplasty utilizes a optical tracking system and a projector to project defect contour on the oversized CCI for the subsequent manual modification. Image courtesy of Murphy etc. [42].

resection onto the oversized CCI (Figure 2.4). This approach minimized the bone gaps between the skull and the resized implant, and the amount of time spent compared to the manual approach.

The approaches mentioned above are the current research within the scope of this thesis on single-stage cranioplasty. The computer-assisted workstation proposed by Murphy et al. is the first system that helps surgeons to outline the defect contour on a prefabricated patient-specific oversized CCI [42]. However, the system requires a specific implant fixation to be designed for each implant. Moreover, this setup is unable to provide accurate defect contour projection on CCIs with complex curvatures. To address the limitations, an integrated handheld projection system is introduced in Chapter 3.

2.4 Technical Background

2.4.1 Medical Augmented Reality

Augmented reality is a form of computer-generated perceptual information, such as graphics or sound, based on the real-world environment. The pioneering Augmented Reality (AR) technology was introduced through an HMD developed by Ivan Sutherland in the mid-1990s [44]. Nowadays, the AR industries are fast expanding. However, HMDs have several disadvantages. Most notably, they are sensitive to latency and have a limited field of view. Also, the rendered scene is only visible to individual users.

Projection mapping, also known as video mapping or Spatical Augmented Reality (SAR), is also an AR technique that turns objects' surfaces into display targets for graphic or video projection. With this technology, real world objects could be enhanced with different visual effects without the need of HMDs. In addition, it allows for a larger field of view with reduced latency that can simultaneously provide multiple users a shared experience.

Nowadays, the AR industry has grown so popular even in the medical field. Many AR applications have been developed, allowing surgeons to directly view the augmented information in the operating field instead of a separate monitor [45–47]. For dynamic senses, projection mapping on movable 3D objects (Pmomo) enables user an interactive AR experience [48]. Although the Pmomo system presents a novel concept, the system relied on a depth camera for tracking objects which can be susceptible to low speed and accuracy.

Numerous procedures have adopted surgical navigation systems, such as

Electromagnetic Tracking Systems (ETS) or Optical Tracking System (OTS), to precisely track the locations of surgical instruments. Surgeons can use a digitizing instrument to acquire intraoperative patient data, such as locating the anatomical features to perform patient-to-CT registration. Although OTS may suffer from occlusion of the line of sight, OTS has been proven to have better accuracy than ETS [49]. However, commercial tracking systems are usually expensive and bulky, limiting their practicality for setup and reconfiguration. A low-cost OTS can be created using Kinect sensors [50]. Nevertheless, such system is still stationary and vulnerable to occlusion.

In this work, the author introduces a Portable Projection Mapping Device (PPMD), which integrates a miniature OTS for surgical navigation into a portable projector to provide surgeons real-time visual guidance for outlining the defect boundary on the oversized CCI, as described in Chapter 3.

2.4.2 Acquisition of Defect Geometries

One of the key components of computer-assisted technology to perform single-stage cranioplasty is precise registration of the patient's skull defect information to the CT space where the oversized CCI is designed. To achieve this goal, the easiest way is to acquire an intraoperative CT scan. However, this is usually not recommended due to the amount of radiation after the removal of the skull bone fragment.

As mentioned in the previous Section, an alternative is to use surgical navigation systems such as OTS to guide their procedures. The first step is to register the patient in the OTS camera space to the preoperative skull model

in the CT space, known as patient-to-CT registration. During this process, the surgeon attaches a reference marker on the patient's skull and then uses a digitizing instrument to contact certain anatomical features defined in the CT model. A spatial transformation can be calculated via point set registration to align the patient in the OTS camera space to its CT space. Therefore, as the surgeon traces the patient's skull defect with a tracked instrument, the defect's boundary can be identified in the CT space. The registered defect information can be projected on the oversized CCI to guide the surgeon to precisely outline the defect boundary [42].

With the advent of 3D scanning technology, many medical applications use 3D scanners to capture the outer shape of an object for 3D measurement [51]. Although 3D scanning has been widely used to generate digital 3D models, it has not been extensively used in cranial or craniofacial reconstruction surgeries. In this work, the author investigates using 3D scanning for intraoperative data acquisition to capture the 3D geometries of the cranial defect in a fast and non-contact fashion.

2.5 Summary

This chapter provides the readers with the medical background and a brief review of related works concerning neuroplastic surgery, specifically single-stage cranioplasty. The challenges and limitations related to single-stage cranioplasty using prefabricated oversized CCIs were also discussed. The chapter also provides the reader the technical background associated with medical augmented reality and intraoperative data acquisition, which leads

to the development of several computer-integrated and robotic systems as described in the subsequent Chapters.

Chapter 3

A Portable Projection Mapping Device for Intraoperative Guidance

3.1 Motivation

As single-stage cranioplasty becomes more prominent in clinical settings, the fitting accuracy characterized by the CCI resizing accuracy has become a major challenge. Several approaches have been developed to help to improve the fitting accuracy between the implant and the skull defect [30, 31, 33–35]. However, all these methods are based on performing planned craniotomy, restricting intraoperative plan change. An alternative approach utilizes intraoperative manual modification of a prefabricated oversized implant. The oversized implant profile provides flexibility during skull resection, but the resizing process heavily depends on the skills of individual surgeons [12]. During the CCI resizing process, the surgeon needs to eyeball the defect geometry and manually cut the oversized implant based on visual judgment, which is imprecise and time consuming.

To improve this shortcoming, Murphy et al. [42] proposed a computer-assisted workstation to project the defect contour on the implant so that the surgeon can visualize the defect boundary on the oversized CCI. This system utilized an optical navigation system to track a surgical instrument and collect the defect contour information. Afterward, the defect boundary was projected on the oversized implant for the surgeon to outline the contour. Lastly, the CCI was manually resized by a handheld burr (Figure 2.4). However, this system has several drawbacks. First, the system relied on user's adjustment to register the implant to the projector. Second, the static projector cannot provide accurate projection for CCIs with complex geometries (Figure 3.1). Third, the setup was complicated, and each implant required a customized fixation to be made.

This Chapter presents a Portable Projection Mapping Device (PPMD) for precise overlay of cranial defect boundary on an oversized CCI. This device combines 3D projection technique with a miniature OTS. Surgeons can use this system for surgical navigation to acquire the defect boundary by tracing the skull resection using a digitizing instrument. Afterward, the system projects the defect boundary on the oversized CCI for the surgeon to outline the defect boundary. Moreover, the PPMD system enables the surgeon to verify the registration by overlaying the CT model or the oversized CCI on the physical skull. The system is cost-effective, providing surgeons an effective method to outline the defect boundary on the oversized CCI.

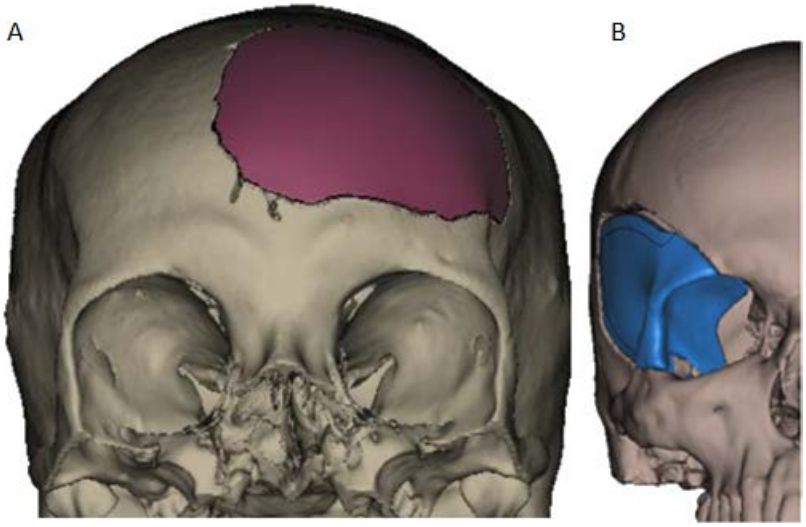

Figure 3.1: Craniofacial deformities enclosed by implants A: A CCI of planar geometry. Implant (pink) does not have sharp curvatures or steep surface drops, and the defect boundary can be outlined via static 2D projection. B: A CCI of complex geometry. Implant (blue) has a complex shape with sharp features, and the defect boundary cannot be accurately projected via 2D projection.

3.2 Contribution

The author's contributions in this Chapter include:

- Designing a portable projection mapping system for medical Augmented Reality (AR) and demonstrating the system's feasibility in single-stage cranioplasty.
- Developing a miniature OTS and a tracking algorithm with implementation in ROS to track multiple surgical instruments in real-time.
- Developing a patient-to-CT registration Graphic User Interface (GUI) and evaluating the tracking and projection mapping accuracy.

Mr. Wei-Lun Huang helped the author in performing camera-projector

calibration, implementing part of the tracking algorithm and assisting the evaluation experiments. The work in this Chapter was published in the Proceedings of SPIE Optical Architectures for Displays and Sensing in Augmented, Virtual, and Mixed Reality (AR, VR, MR) (2020) and won the second place at the optical design challenge [52]. The author has also filed a PCT patent application titled *"Portable Projection Mapping Device and Projection Mapping System for Providing Spatial and Temporal Mapping of Images and/or Videos"*.

3.3 Methods

3.3.1 System Design

The PPMD system consists of a laser projector (Laser Beam Pro C200) and an RGB-D camera converted into a stereo infrared camera (Intel RealSense D435i camera). The Intel Realsense D435i camera contains an RGB camera with a resolution of 1920 x 1080 of frame rate at 30 fps, and an active stereo IR camera with a resolution of up to 1280 x 720 of frame rate at 90 fps, providing depth stream. The PPMD can be handheld or mounted on a tripod. Similar to commercial tracking systems, such as NDI Polaris, the PPMD system utilizes the stereo vision of the RealSense D435i camera as its optical tracking unit due to its higher frame rate and robustness to interference of ambient light. A pair of 850 *nm* narrow bandpass filters are installed on the depth camera to convert it into a stereo infrared camera as shown in Figure 3.2. An infrared LED emitter is installed in the middle between the two IR camera units, emitting 850 *nm* infrared light. As each surgical instrument is attached with a few retro-reflective spheres in a specific pattern, the retro-reflective spheres reflect

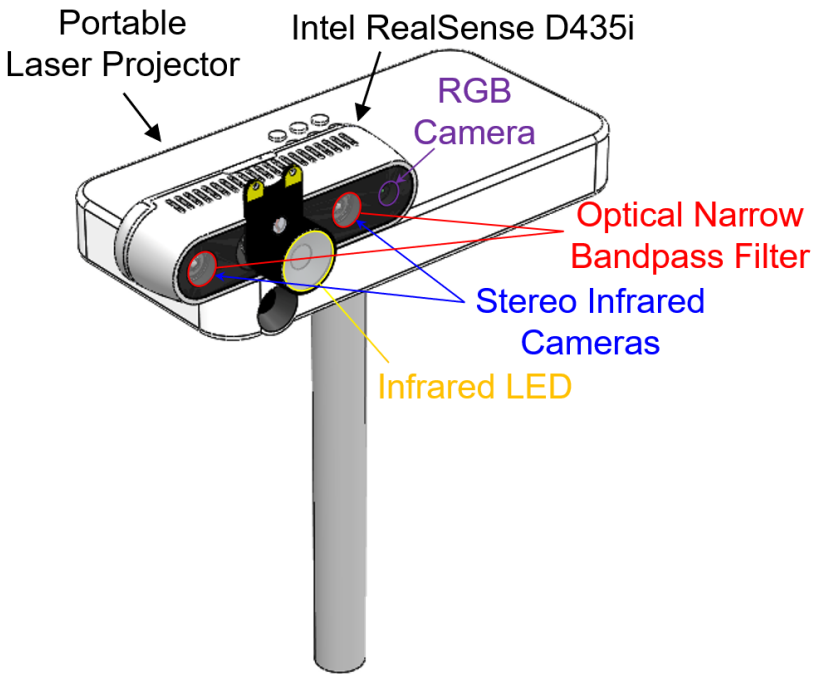

Figure 3.2: PPMD system components The system consisted of a laser projector, an RGB camera, a pair of stereo infrared cameras with optical narrow bandpass filter and an infrared LED light source.

the infrared light back to the LED source.

An overview of of applying PPMD in single-stage cranioplasty is shown in Figure 3.3. The red area on the plastic skull represents the skull defect. After the patient-to-CT registration, the location of the CCI can be determined and visualized on the skull by projection mapping (the blue area). The defect contour can be outlined with a digitizing instrument and displayed in real-time (the green line). The traced defect boundary can be transformed to the CT space. Since the oversized CCI is designed from the CT model, the acquired defect boundary indicates the amount of modification on CCI by reducing its size in order to fit the defect. Therefore, the surgeon can use this proposed PPMD system to visualize the defect boundary on the CCI to guide their

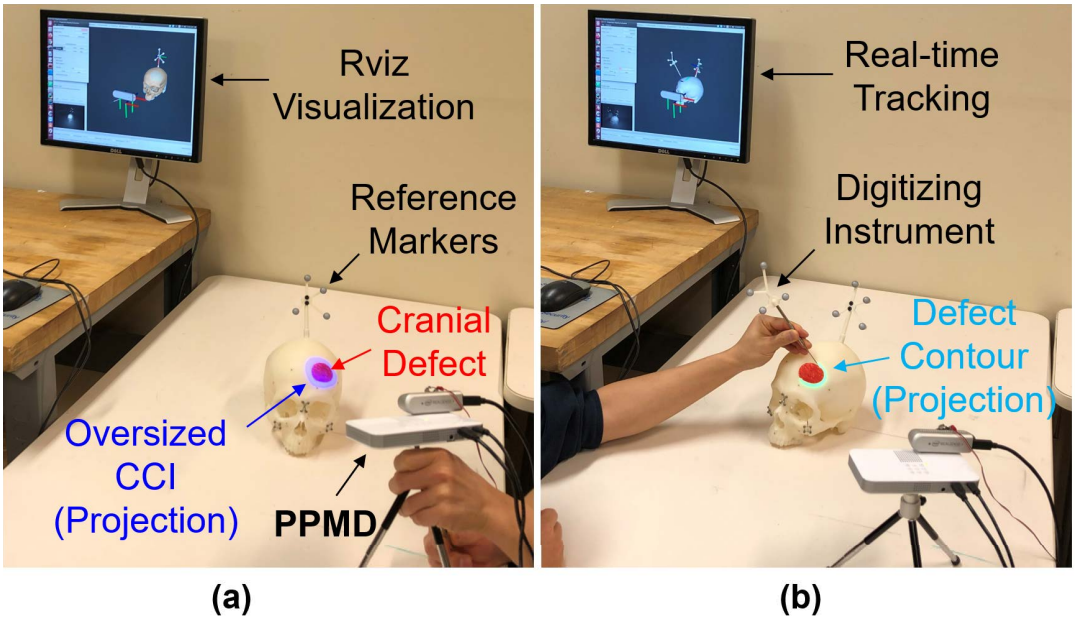

Figure 3.3: Single-stage cranioplasty demonstration (a) An oversized implant was mapped from the CT space to the patient space after registration, and was projected on top of the skull. (b) The cranial defect contour was acquired by tracing it with a digitizing instrument. Real-time instruments tracking and visualization were shown.

manual modification.

The PPMD system enables surgeons to visualize patient data directly on the patient's body during surgical procedures. The pipeline of the system is shown in Figure 3.4. Prior to using the system, it is necessary to run a one-time camera-projector calibration to calculate the unique intrinsic parameters of the camera and projector as well as the extrinsic parameters that represent the transformation between the camera and projector.

To recognize and track the surgical instruments, the system requires the configuration of the surgical instrument defined by a set of retro-reflective markers. In our experiment, we designed two tracking instruments: a reference marker and a digitizer. During single-stage cranioplasty, the reference

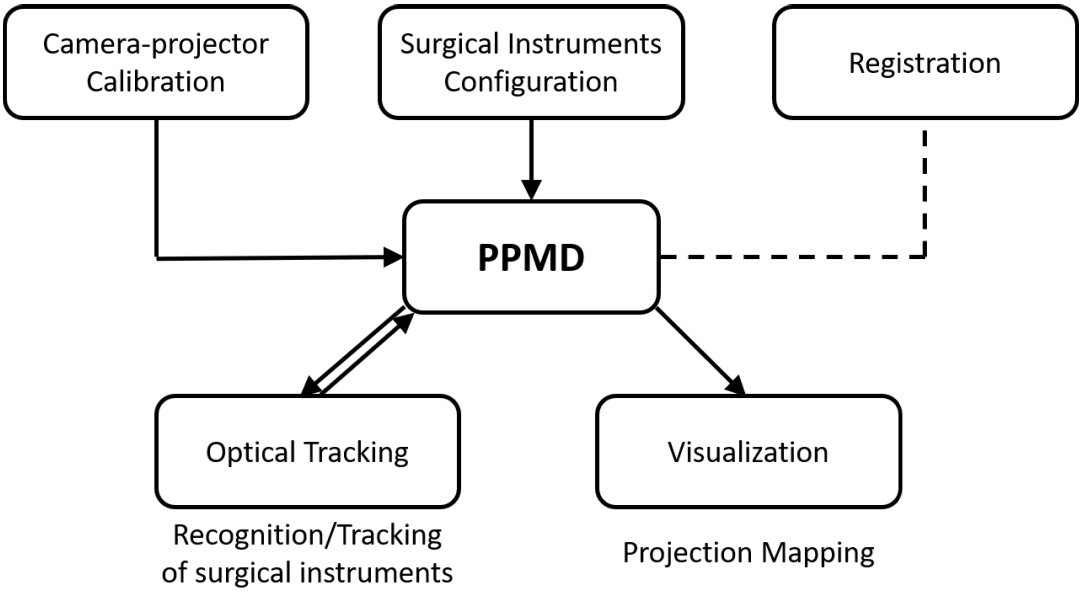

Figure 3.4: The PPMD's high-level block diagram The diagram shows the pipeline of the PPMD system.

instrument is attached to the skull to track the patient's head. The digitizing instrument acts as a free-hand probe to interact with the system. The system tracks and computes the poses of the instruments in real-time. As such, any point in 3D space of the real-world can be determined with respect to the reference frame coordinate system. Therefore, after completing the registration between the patient head and the CT model, the surgeon can visualize the CT skull model directly overlaid on the patient's head, as shown in Figure 3.5. Furthermore, using the digitizing instrument, the surgeon can interact with the system to virtually draw on the patient's head for surgical planning or intraoperative data collection.

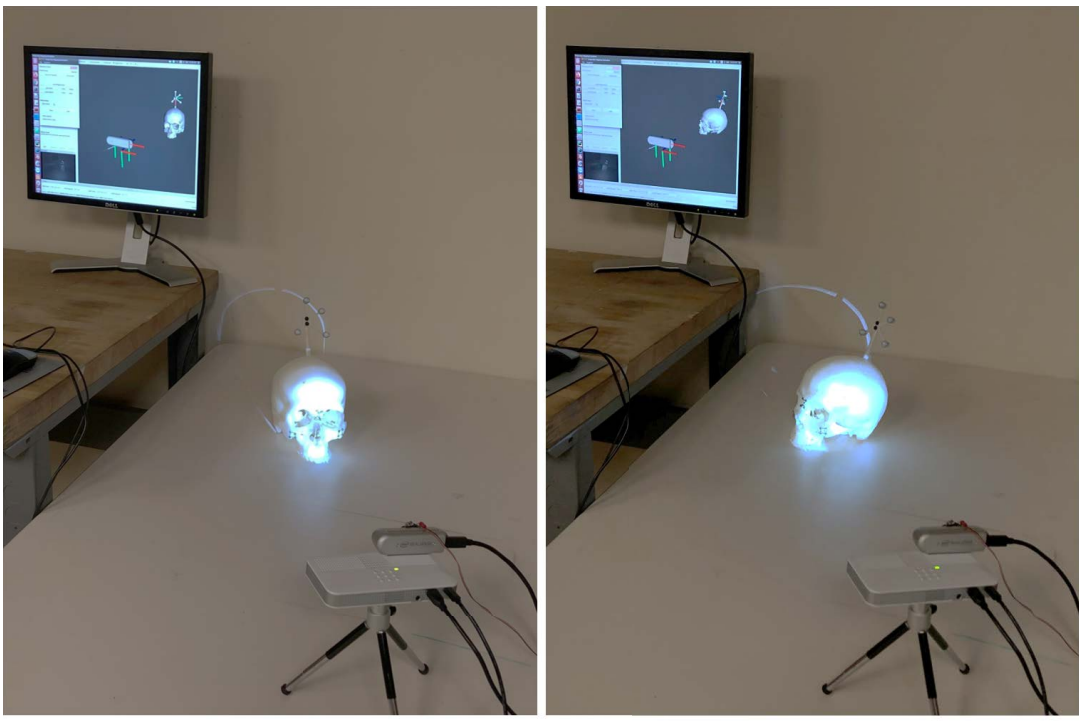

Figure 3.5: Overlaying the CT skull model on patient The registered CT skull model was overlaid on the physical skull via projection mapping. Surgeon can roughly determine the registration accuracy based on the model alignment.

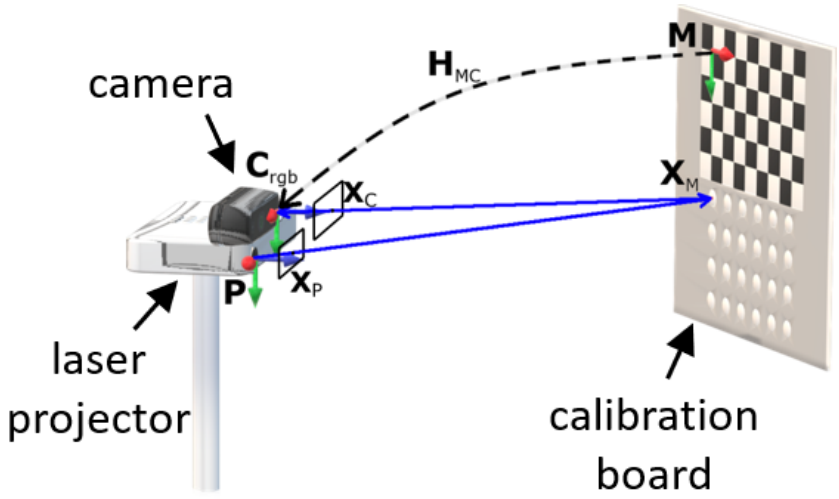

Figure 3.6: Camera-projector calibration The camera projector calibration finds the transformation of the project frame {**P**} from the camera frame {$\mathbf{C_{rgb}}$}. A calibration board is used during this process, and the projector projects a grid pattern on the calibration board.

3.3.2 Camera-Projector calibration

A camera-projector calibration is required when the location of the camera relative to the projector has been changed or is unknown. This process is required only once as long as the hardware configuration is not changed after the calibration. The calibration, however, can be updated very quickly and easily with the calibration tool developed in our application.

Camera-projector calibration consists of camera calibration, projector calibration, and a stereo calibration between the camera and projector. We employ the pin-hole model for both camera and projector calibration and then apply Zhang's method, in which the projector is treated as an inverse camera [53, 54]. As shown in Figure 3.6, we define three coordinate systems: {**M**} represents the model space of the chessboard, {$\mathbf{C_{rgb}}$} is the RGB camera frame, and {**P**}

is the projector frame. We first calibrate the camera to obtain its intrinsic parameters as well as the extrinsic parameters describing the transformation between camera and chessboard, $\mathbf{H_{MC}}$ in homogeneous form. Next, the projector projects a grid pattern, where the grid coordinates in projector space are already defined as $\mathbf{X_P}$, onto the plane of the chessboard. With the coordinates of the projected grid in the camera frame $\mathbf{X_{C_{rgb}}}$, the coordinates of the projected grid in model space $\mathbf{X_M}$ can be computed by ray casting from the origin in camera space and using the intrinsic parameters of the camera and $\mathbf{H_{MC}}$. With $\mathbf{X_P}$ and $\mathbf{X_M}$, the projector can be calibrated to find its intrinsic parameters with a PnP algorithm on planar object by considering the projector as a camera. Finally, stereo calibration can be performed using the grid coordinates in the camera space $\mathbf{X_{C_{rgb}}}$, in projector space $\mathbf{X_P}$, and in model space $\mathbf{X_M}$ to find the extrinsic transformation from camera to projector.

The camera-projector calibration application is developed using visualization toolkits (VTK[1]) and Qt [2]. Once the user launches the application, two windows will appear. One window renders an array of circle dots for the projector to display. The projector is set as an external display to the computer at resolution 1280 x 720. Once the user drags the window containing the array of circles to the projector display, the application enters full screen mode (Figure 3.7). The second window contains a camera view of the RGB camera along with all the calibration parameters, such as number of circles, circle size, etc. Once the user clicks the calibrate button, the application starts capturing images at a time interval specified by the user. The number of images collected

[1] https://vtk.org/
[2] https://www.qt.io/

for the calibration process depends on the clarity and size of the pattern shown in the image. As a rule of thumb, a minimum of 10-20 images should achieve an acceptable calibration result.

We use the principle of stereo camera calibration to calculate the transformation from the RGB camera to projector. Since we use the Intel RealSense D435i, the product manual provides manufacturing dimensions and the distance between the IR cameras and the RGB camera. With the transformation from the RGB camera to the projector acquired from calibration and the known transformations from the IR cameras to the RGB camera, the transformation from the IR cameras to the projector can be readily calculated. From the IR cameras, the pose of the retro-reflective markers $\mathbf{H_{CR}}$ is known as shown in Figure 3.9; therefore, the transformation of the reference frame to the projector can be calculated. From the registration result for the transformation from the model frame of the skull {**M**} to the reference frame {**R**} and with the registration module mentioned in Sec 3.3.4, the PPMD system finds the relative pose of the projector with respect to the skull model frame {**M**}.

3.3.3 Surgical instrument configuration, recognition, and tracking

A surgical instrument is a configuration of a set of the retro-reflective sphere markers with their positions defined in its CAD model coordinate system [55]. In our setups, we designed two instruments, a reference and a digitizing probe, with retro-reflective markers based on NDI instrument design recommendations. For the digitizing probe, the pivot calibration tool provided by NDI Polaris was used to find the coordinates of the retro-sphere markers in

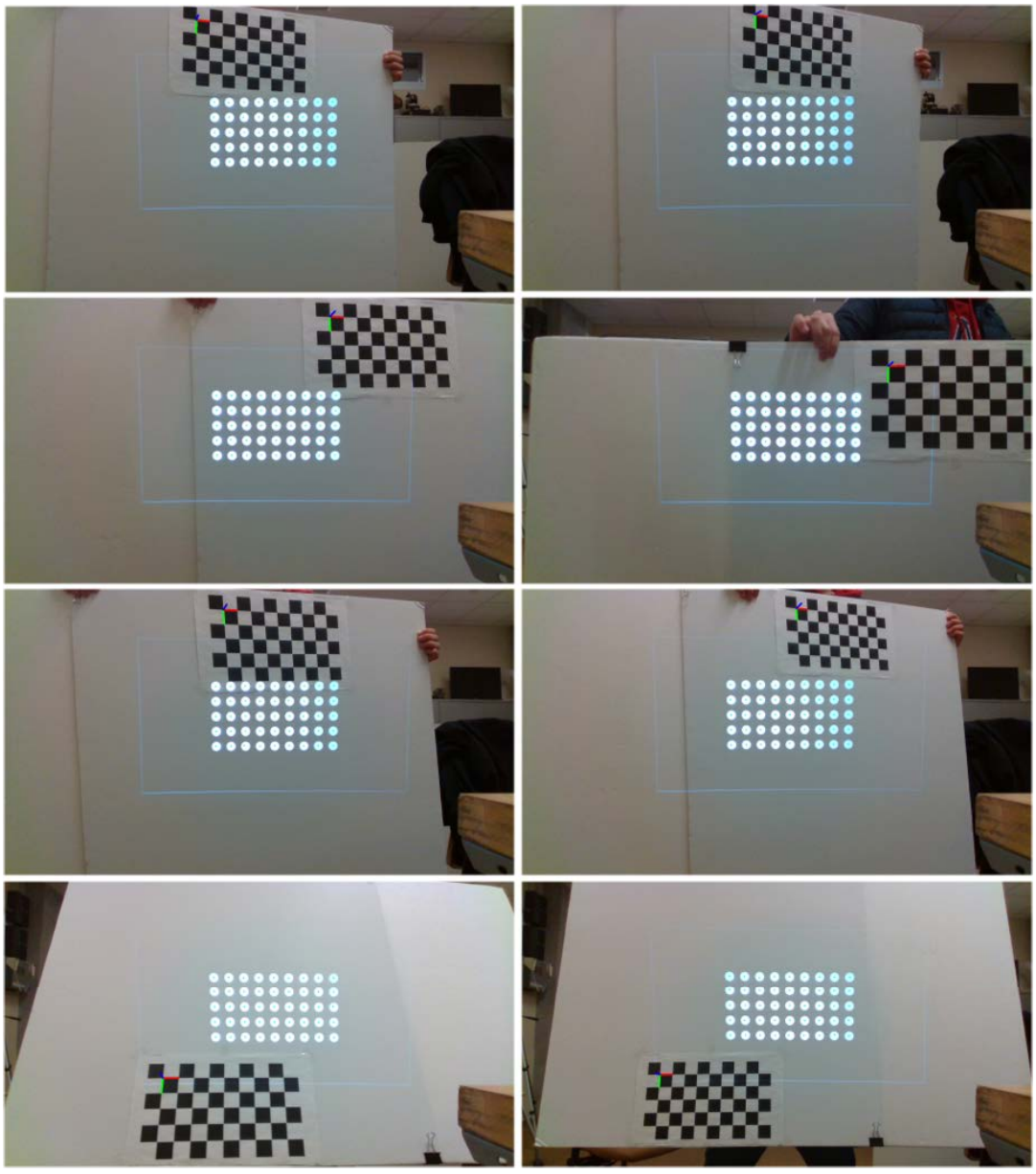

Figure 3.7: Camera projector calibration During camera projector calibration, the user moves the calibration board to different poses for camera to capture images.

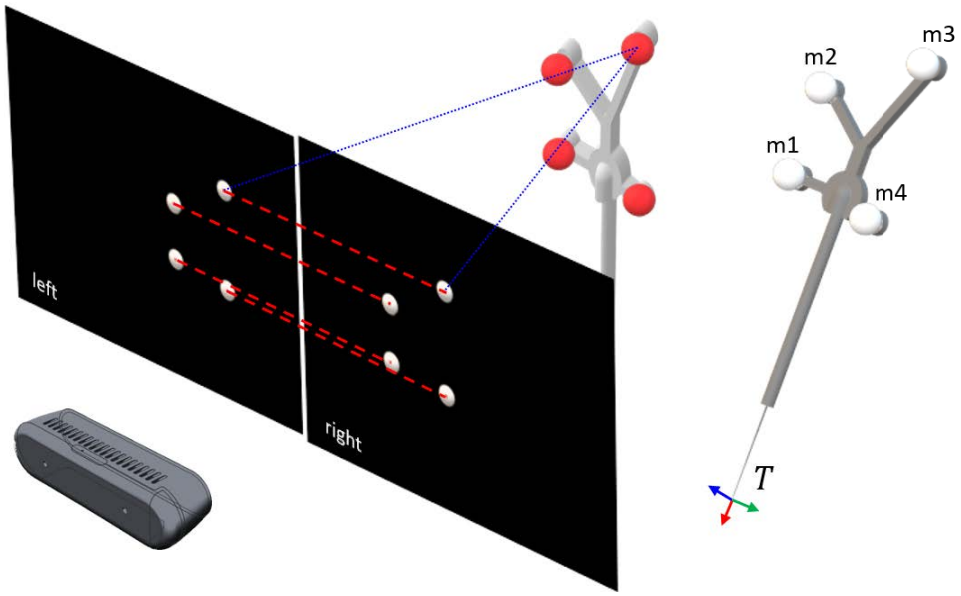

Figure 3.8: Stereo vision triangulation The 3D coordinates of the retro-reflective markers were reconstructed via stereo vision triangulation.

the coordinate system attached to the tip of the digitizing probe, as shown in Figure 3.9, as frame {**T**}. The digitizing probe is a six-degree-of-freedom (6-DOF) interaction device consisting of four retro-spheres (m1, m2, m3, m4).

When tracking systems are used based on stereo vision, surgical instruments are treated as rigid bodies. A rigid body is a fixed geometrical arrangement of at least three markers as feature points for tracking [55]. After PPMD is calibrated and the realtime tracking procedure is launched, the optical tracking node is invoked, and several parameters will be initialized, such as IR camera intrinsic parameters and instrument configurations. Afterwards, the following online steps can be performed to recognize instruments and obtain their 6-DOF poses: binocular image capture, marker extraction, marker

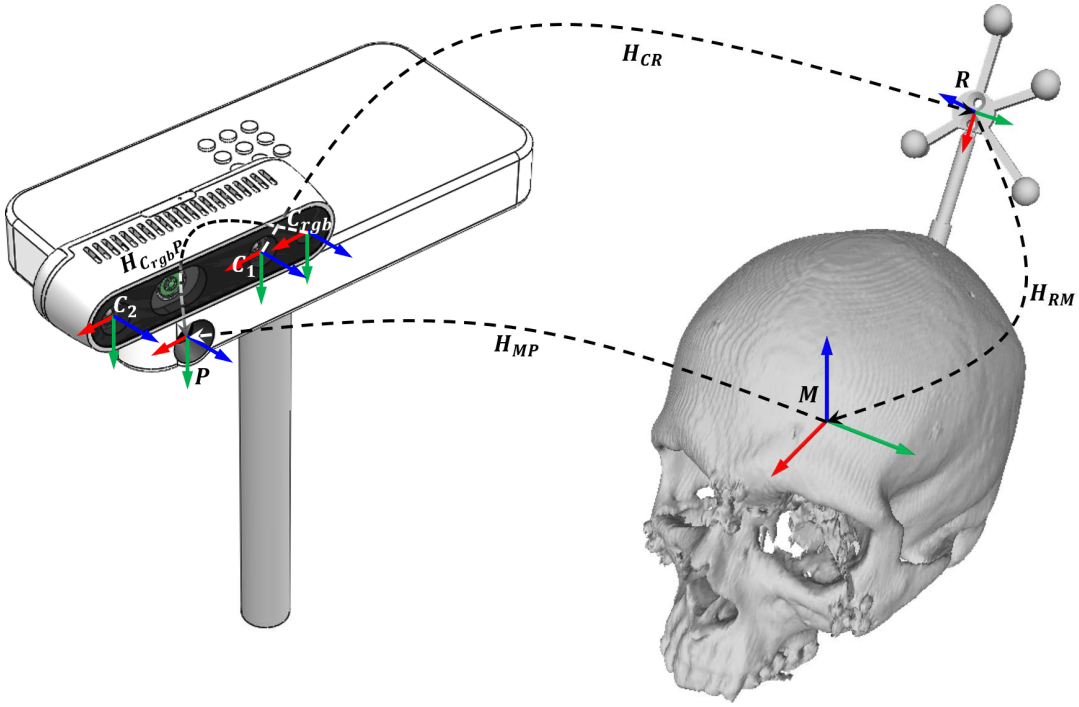

Figure 3.9: Frame transformations The skull model is registered to the projector space and is tracked by the OTS camera via the attached reference marker {**R**}. The transformations between the IR cameras and RGB camera are provided by the factory parameters.

matching, 3D coordinate reconstruction of markers, model fitting, and 3D registration [56, 57]. A description of each step is listed below, and a diagram illustrating the workflow of the recognition and tracking algorithm developed in ROS is shown in Figure 3.10. Intel RealSense provides an open-source ROS wrapper. The software is available on GitHub [3] under an Apache License, Version 2.0.

1. **binocular image capture:** The optical tracking node subscribes to the image topic published by Realsense D435i camera and receives synchronized images from the stereo IR cameras. Since we have installed an

[3]RealSense ROS Wrapper: https://github.com/IntelRealSense/realsense-ros

IR emitter and filter on PPMD, only the markers will be highlighted in the images, while the rest of the image will be darkened. When new images arrive, the optical tracking callback function is triggered to track the markers.

2. **marker extraction:** With the processed grayscale images, we can use blob detection to determine the 2D image coordinates of the centroid of the highlighted area. In an optical tracking system, an accurate extraction of the pixel coordinates of the marker's center is crucial because they are used to calculate the 3D coordinates of the marker positions in the camera frame. We used OpenCV's blob detection, which allows users to tune several parameters, such as threshold, area, circularity, and convexity of blobs, to optimize the performance of marker extraction for different scenarios.

3. **marker matching:** The correspondence of markers detected at the same location in the left and right images must be established prior to 3D coordinate reconstruction. For a marker m in the left image, we need to determine its correspondence m' in the right image. This is done by searching along the epipolar line of m in the right image, where m' lies on. As there is only a translational shift along the horizontal axis between the left and right IR cameras in RealSense D435i, the epipolar line of m is a horizontal line of the same pixel coordinate in the right image, and vice versa (Figure 3.8). The detected markers in the left and right images are sorted according to their positions vertically and then horizontally. Hence, the correspondence of the markers can be

established by matching their sorted orders.

4. **3D coordinate reconstruction of markers:** Once markers are matched pairwise in the left and right images, the 3D coordinates of the detected markers can be reconstructed via triangulation. The markers' 3D coordinates are derived from their 2D coordinates in the two image planes knowing the intrinsic parameters of stereo IR cameras and the extrinsic parameters representing the transformation between them.

5. **model fitting:** Given a set of 3D reconstructed markers, the instrument recognition problem can be defined as matching a subset of the 3D reconstructed markers to the markers defined in Section 3.3.3. Assuming N reconstructed markers and K markers in a surgical instrument, a brute force method is used to compute a best-fitting distance matrix to a predefined pattern distance matrix from a subset of $\frac{N!}{(N-K)!}$ permutations of $K \times K$ matrices, where the distance matrix is a $K \times K$ symmetric matrix constructed by measuring the 3D distance between each marker pair of the pattern. For multiple surgical instruments, the time complexity is $O(N!)$, assuming the computation of difference between two $K \times K$ distance matrices can be performed in constant time. Sun et al. has suggested methods to find out the matching for single instrument based on distance matrix and a variation to settle the potential occlusion problem [55]. On the other hand, Cai et al. has provided solutions on tracking multiple instruments by using two intersecting lines and marker codes, where the two intersecting lines can determine a point and each marker code is the sum of the codes for the distances between the marker and

the other markers on a surgical instrument [58].

We adopted the method of finding the best-fitting distance matrix. However, the computational time complexity is reduced to $O(N^3)$ by first grouping markers that are on the same surgical instrument and then adding a convex hull constraint with clockwise order for grouped markers. With N reconstructed markers, we first find the two furthest markers from $\binom{N}{2}$ combinations of pairing distances. We can then group two sets of markers centered at the two furthest markers. Knowing the number of markers on a surgical instrument, K, the grouping step can be performed by including the closest $K-1$ markers in which their distance to the center is within the maximum marker pair distance among multiple surgical instrument configurations. Next, for every group of markers, assuming K markers in a group, the convex hull constraint can be applied to reduce number of combinations of distance matrices from $O(K!)$ to $O(K)$. In addition, by assigning a certain order, such as clockwise, the number of combinations from the convex hull constraint is further reduced by half.

6. **3D registration:** After the 3D reconstructed markers are matched to the markers defined in a surgical instrument configuration, we have the marker locations in camera space and their own model space, denoted as $\mathbf{P_C}$ and $\mathbf{P_M}$ respectively. We can apply the closed-form solution in Section 3.3.4 to compute the transformation from the camera to the instrument, $\mathbf{H_{CM}}$, which is also the pose of the instrument in the camera coordinate system.

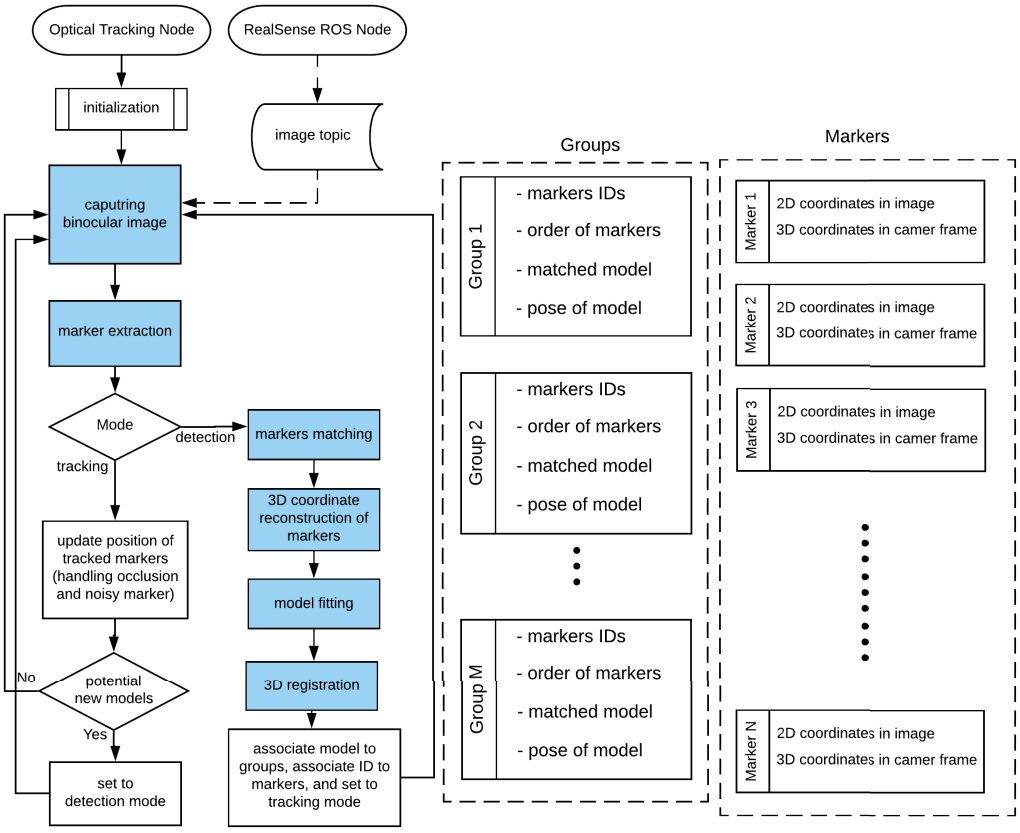

Figure 3.10: Tracking algorithm flowchart The flowchart of the tracking algorithm.

As shown in Figure 3.10, the system has a tracking mode and a detection mode. After the initial detection and recognition of surgical instrument, each group of markers would be associated with a surgical instrument configuration, and every reconstructed marker would be associated with a unique identification. This method efficiently keeps track of groups of markers. In addition, this allows us to handle noisy marker detection and occlusion as long as there are at least three markers detected for a surgical instrument.

3.3.4 Registration

To reconstruct the 3D model of the skull, CT images were obtained with voxel dimension 300 $mm \times 300\ mm \times 300\ mm$ and mesh slice thickness 0.5 mm. Through registration, we would like to calculate the transformation between the model frame **M** and the reference frame **R**, $\mathbf{H_{MR}}$ in homogeneous form, so that every coordinate system is later transformed into the reference space **R** in Section 3.3.5. The model space **M** can be derived after 3D reconstruction using CT images. The reference space **R** is defined for the reference instrument that is fixed onto the head. The 3D mesh of the head is rendered as shown in the registration GUI in Figure 3.11 (A) We chose to calculate $\mathbf{H_{MR}}$ by selecting anatomical landmarks as shown in Figure 3.11 (B) During the selection procedure, the digitizing probe was used to pick the anatomical landmarks as described in Section 3.3.3, and their locations were calculated by using the transformation from the stereo IR camera to the reference $\mathbf{H_{CR}}$ and the transformation from the stereo IR camera to the probe $\mathbf{H_{CT}}$. Landmarks selected by the digitizing probe are first represented in camera space as $\mathbf{P_C}$, which can be

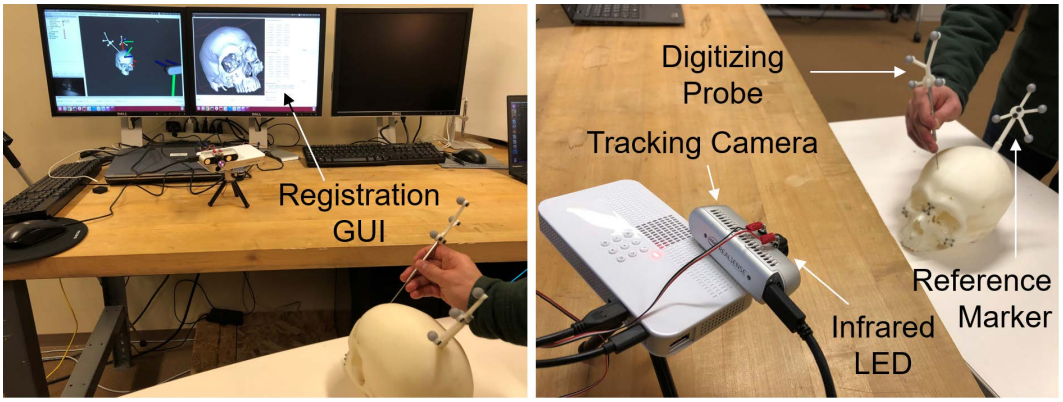

Figure 3.11: Patient-to-CT registration User used a digitizer probe to contact anatomical points to register the skull model from the patient space to CT space.

transformed into reference space with $\mathbf{P_R} = \mathbf{H_{CR}}^{-1}\mathbf{P_C}$. With the landmarks represented in reference space and model space as $\mathbf{P_R}$ and $\mathbf{P_M}$ respectively, the 3D rigid transformation between two sets of point-correspondences can be computed. The problem can be formalized as

$$\hat{H}_{MR} = \arg\min_{H_{MR}} \sum_{i=1}^{n} (P_M - H_{MR} P_R)^2$$

Several closed-form solutions exist for the expression, and we chose to implement the approach developed by [59], which is based on computing the singular-value decomposition of a derived matrix [57]. Note that the procedure inherits the error of surgical instrument tracking and user error for manual selection. Once $\hat{\mathbf{H}}_{\mathbf{MR}}$ is estimated, $\mathbf{P_M}$ can be transformed into the reference space as $\hat{\mathbf{P}}_{\mathbf{R}}$, where $\hat{\mathbf{P}}_{\mathbf{R}} = \hat{\mathbf{H}}_{\mathbf{MR}}^{-1}\mathbf{P_M}$. Finally, the registration error can be derived by calculating the average landmark pairs distance for $\mathbf{P_R}$ and $\hat{\mathbf{P}}_{\mathbf{R}}$. In one test, the registration error of the selected skull is 2.70 mm, and its visualization through projection mapping is shown in Figure 3.5.

3.3.5 Projection mapping

A virtual scene is built to precisely match the real scene. This requires the camera intrinsic parameters and the camera pose defined in the virtual scene. In projection mapping, the projector is treated as a viewing camera in the virtual scene. The camera needs to be set up by using the projector's intrinsic parameters from the calibration result in Section 3.3.2. In addition, the transformation from the 3D model of the object to the camera in the virtual scene, $\mathbf{H_{OC}}$, is identical to the transformation from the object to the projector in the real world, $\mathbf{H_{MP}}$. Since the coordinate system of virtual scene has been set to align with the coordinate system of the skull model $\mathbf{M}$, we can update $\mathbf{H_{OC}}$ from $\mathbf{H_{MP}}$ during the projection mapping process, where $\mathbf{H_{OC}} = \mathbf{H_{MP}}$. As shown in Figure 3.9, PPMD knows the transformation from the projector to theRGB camera $\mathbf{H_{PC_{rgb}}}$ from Section 3.3.2, the transformation from the RGB camera to the IR cameras $\mathbf{H_{C_{rgb}C}}$ from RealSense, the transformation from the IR cameras to the reference instrument $\mathbf{H_{CR}}$ from Section 3.3.3, and the transformation from the reference instrument to the model of skull $\mathbf{H_{RM}}$ from Section 3.3.4. Therefore, the desired transformation can be derived as

$$\mathbf{H_{MP}} = \mathbf{H_{RM}}^{-1}\mathbf{H_{CR}}^{-1}\mathbf{H_{C_{rgb}C}}^{-1}\mathbf{H_{PC_{rgb}}}^{-1}$$

Note that the computation of $\mathbf{H_{MP}}$ can be neatly and efficiently handled by the 'tf' package in ROS [4]. Finally, the image rendered from the camera view in the virtual scene is what will be projected.

In single-stage cranioplasty, the patient's head is mostly stationary during

[4]RealSense ROS TF: http://wiki.ros.org/tf

the operation. Therefore, the skull model frame **M** can be used as the global fixed frame during visualization. As the user moves the PPMD by hand, the transformations are updated in real-time with every single image frame. As stated in Sec 3.3.1, the depth camera of the RealSense D435i's frame rate runs up to 90 Hz. Therefore, the users hardly see any projection lag. Image lagging in AR/VR applications often causes the user to feel uncomfortable and dizzy, especially with HMDs. The PPMD, therefore, has the advantage of providing the user with a comfortable viewing experience. The visualization result of projection mapping for single-stage cranioplasty scenario can be found in Figure 3.3, where (A) shows an overlaying of an oversized customized cranial implant on top of the plastic skull and (B) shows a visualization of outlining the defect contour.

3.4 Experiments and Results

3.4.1 Instrument tracking

To evaluate the tracking accuracy of the surgical instruments using PPMD, we compared the tracking result by free-hand motion between PPMD and the NDI Polaris optical tracking system. Knowing the tracking accuracy of Polaris optical tracking system can achieve within 0.3mm, we used Polaris tracking result as our ground truth to estimate the tracking accuracy of PPMD. As shown in Figure 3.12, both devices are set up on tripods and placed a certain distance away from each other to ensure that the testing area is within the working range of both systems respectively and with their field of views aligned facing the testing area.

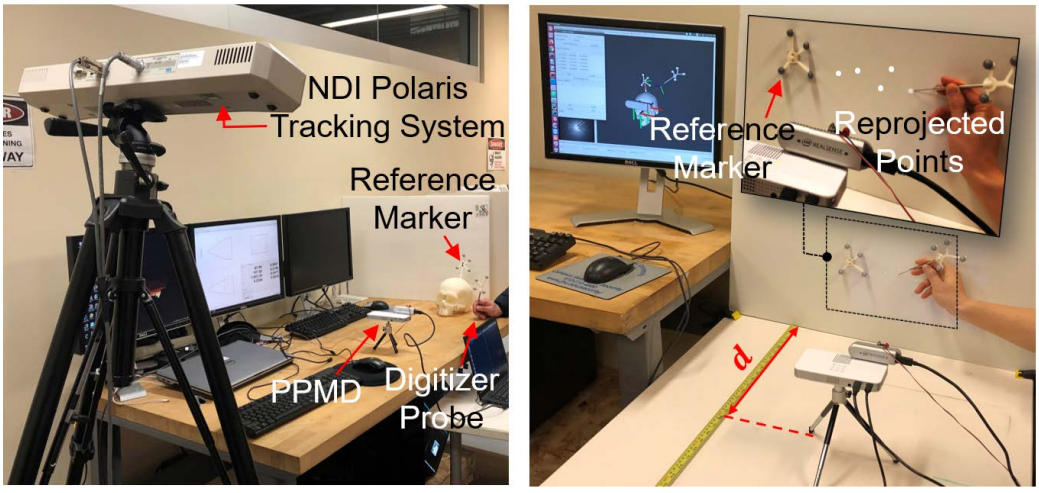

Figure 3.12: Experiment setup (a) A NDI Polaris optical tracking system is used for comparison reference. A reference marker and a digitizer probe are used to evaluate the tracking accuracy of the PPMD system. (b) Points defined on a white board are collected via the digitizer probe at the first round. The collected points are projected on the white board and collected at the second round.

We conducted 8 sets of evaluation tests by changing the distance d of the reference and probe markers to PPMD. The PPMD system was configured to collect data at a running rate of 90 Hz, whereas the NDI Polaris was at 20 Hz. The test began by first placing a board in front of both reference and probe instruments to block the view of the markers in PPMD and Polaris. When the recording started, no actual data were recorded until the board was removed. We assume both devices will start recording data simultaneously when the board is removed as the markers are made visible to the two systems. We established pose correspondences of the collected data from both systems. Figure 3.13 and Figure 3.14 show the free-hand motion of the probe with respect to the reference tracked by PPMD and the Polaris tracking system. The plotted lines represent the tracked position of the probe while the arrows

Table 3.1: Instrument tip tracking accuracy

Distance (cm)	**20**	**30**	**40**	**50**	**60**	**70**	**80**	**90**
Average translational error (mm)	0.87	0.97	1.18	1.06	1.31	1.51	2.10	3.55
Average rotational error (degs)	0.78	0.75	0.94	1.27	1.55	2.27	3.93	2.90

indicate the orientation of the probe. The accuracy is shown in Table 3.1. The average translational error $Error_{trans}$ is derived from

$$Error_{trans} = \frac{\sum_{i=1}^{N} \left\| P^i_{polaris} - P^i_{ppmd} \right\|}{N}$$

where $P^i_{polaris}$ is the position of pose i measured in Polaris, P^i_{ppmd} is the position of pose i measured in PPMD, and N is the number of correspondent poses. In our experiments, we have 120 pose pairs. The average rotational error $Error_{rot}$ is measured by

$$Error_{rot} = \frac{\sum_{i=1}^{N} \theta^i}{N}, \theta^i = \cos^{-1}\left(\frac{\left(R^i_{ppmd}\right)^{-1} R^i_{polaris} - 1}{2} \right)$$

where $R^i_{polaris}$ is the orientation of pose i measured in Polaris, R^i_{ppmd} is the orientation of pose i measured in PPMD, and N is the number of correspondent poses. Note that PPMD achieves sub-millimeter tracking accuracy within a working range of 30 cm from instruments.

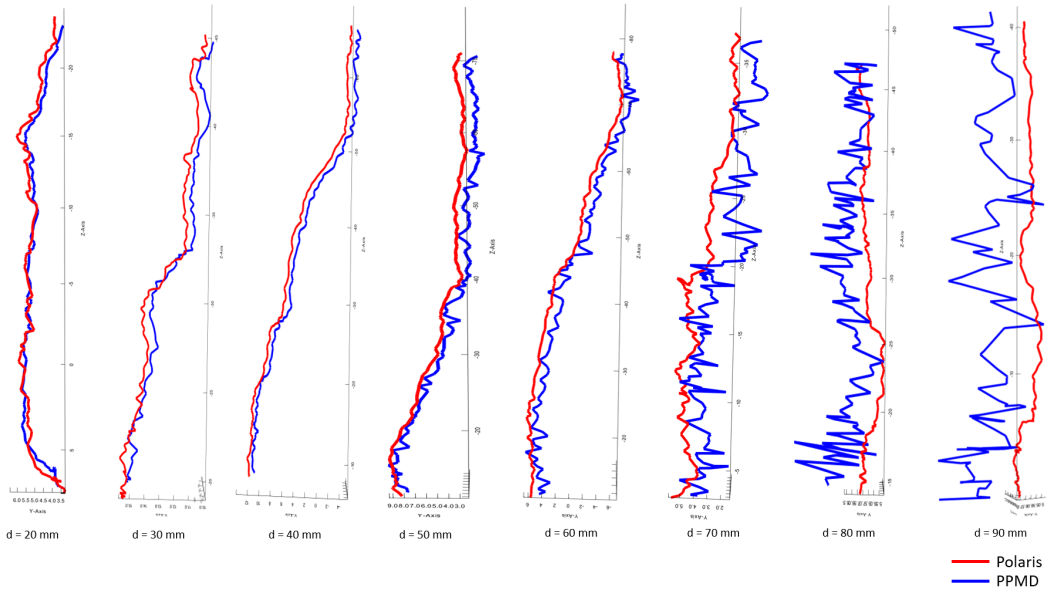

Figure 3.13: Position tracking error The positions of the digitizer probe tracked by NDI Polaris (red) and by PPMD (blue) at different distances from the PPMD's OTS camera.

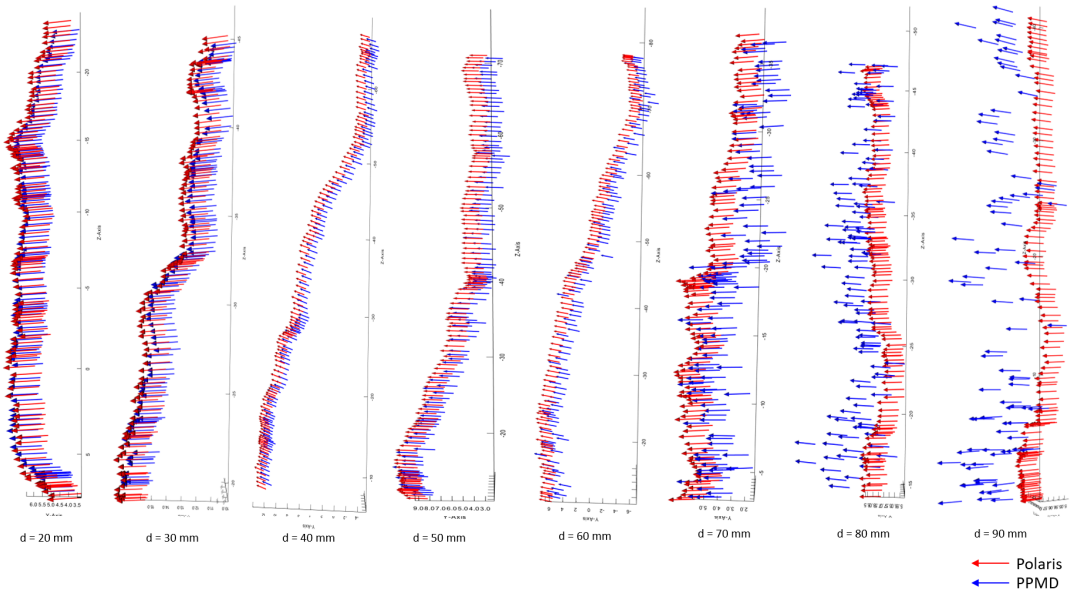

Figure 3.14: Orientation tracking error The orientations of the digitizer probe tracked by NDI Polaris (red) and by PPMD (blue) at different distances from the PPMD's OTS camera.

3.4.2 Instruments tool-tip tracking by projection mapping

A preliminary experiment was conducted to evaluate the accuracy of the projection mapping and tracking of the instruments tool-tip. As shown in Figure 3.15, with a reference instrument in camera view, in the first round, we use PPMD to record 20 random tool-tip position of the probe instrument drawing on a white board parallel to the device at a given distance. Next in the second round, those points were projected back onto the board, and then we used PPMD to recollect these points with the same probe instrument. Note that the experiment includes the error doubly propagated from optical tracking. Similar to the evaluation of tracking accuracy of the instrument's tool-tip, we performed experiments at various distances between the camera and the white board, ranging from 40 to 90 cm. Finally, the average euclidean distance between the two sets of collected points in these two rounds were calculated (Figure 3.15). Table 3.2 shows the total reprojection error measured by the difference between the instrument's tool-tip positions.

Table 3.2: Instrument tool-tip tracking error propagation

Distance (cm)	**40**	**50**	**60**	**70**	**80**	**90**
Average error (mm)	7.53	8.71	10.13	14.74	14.19	17.86

3.5 Summary and Discussion

This work utilizes projection AR to allow the surgeon to visualize the defect boundary on the oversized CCI. A real-time 3D projection system is developed

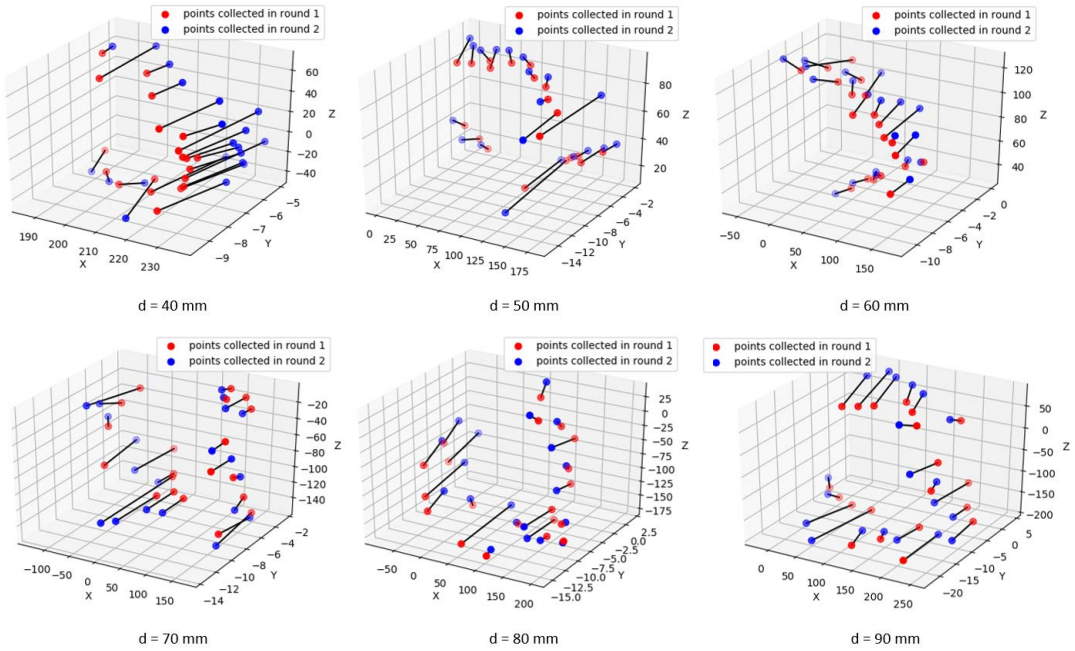

Figure 3.15: Camera-Projector reprojection error The errors between the points collected at the first round (red) and the second round (blue).

for registration, projecting CT models, prefabricated cranial implants, and acquiring defect geometries during single-stage cranioplasty. The system provides simultaneous optical tracking via a modified stereo IR camera mounted on the projector. An optical tracking algorithm is developed to track multiple surgical instruments and reference markers. The author also developed a GUI for camera-projector calibration, patient-to-CT registration, and projection mapping. The author evaluated the tracking accuracy of the proposed OTS comparing to the NDI Polaris OTS, and measured the projection mapping error. The results showed that the tracking and projection mapping accuracy are relatively small within a short range.

The developed PPMD system allows the surgeon to visualize the defect geometry directly on the CCI via projection AR. The author quantified the

tracking accuracy of its onboard OTS camera by comparing it with the commercially available OTS, and demonstrated a comparable accuracy when the system operates at a short distance. As this handheld system is designed for short-range applications, long distances can compromise its tracking accuracy. The system is also more compact compared to the commercial optical tracking system and, therefore, more cost-effective.

Moreover, this work introduces the basic techniques for the patient-to-CT registration and camera-projector calibration, which allows the system to capture and output the defect geometry. The developed system also takes advantage of utilizing registration points, either anatomical points or externally attached markers, to accomplish the registration process. Using this technique, the author integrates the registration, optical tracking, and projection mapping into one package. This innovation makes further improvements of automating the resizing process possible, as the author will further discuss in the next Chapter.

Chapter 4

A Robotic System for Implant Modification

4.1 Motivation

The previous Chapter introduced a portable projection mapping system that assists the surgeon to better visualize the defect boundary on the oversized CCI. This system utilizes an OTS camera to perform patient-to-CT registration using anatomical feature points. After registration, the surgeon acquires the defect contour by tracing the skull resection edge using a digitizing instrument. The collected defect boundary can then be projected on the oversized CCI to guide the subsequent manual resizing. Although this SAR technique provides visual guidance, it still requires manual resizing by the surgeon. Moreover, the developed OTS camera collects one data point per frame, which is error-prone and susceptible to noise. Nevertheless, such a technique enables surgeons to gauge the amount of manual resizing more precisely. This Chapter reports the investigation of automating the CCI resizing process. Furthermore, the application of the 3D scanning technique is investigated to facilitate the

intraoperative data acquisition of cranial defects.

Recent advances in 3D scanning technologies provide new venues for applications in the medical field. 3D scanning generates high-quality 3D models of real-world objects. The 3D models can be used to generate programs for robots to achieve a series of specific autonomous tasks. Different from the OTS camera, a 3D scanner can collect thousands of data points per frame without contacting the object. Therefore, using a 3D scanner can simplify and expedite the intraoperative data acquisition process, making the patient-to-CT registration faster and more accurate.

This Chapter presents a novel robotic system for generating precise CCIs for patients who undergo single-stage cranioplasty, as shown in Figure 4.1. The system relies on a handheld 3D scanner and a cutting robotic arm. 3D scanning enables fast and accurate registration. The 3D scanned defect model can then be used to generate the robot's cutting toolpath. To evaluate the resizing performance of the system, the author proposes to measure the gaps between the resized implant and the defect skull. The combination of 3D scanning and cutting robotic arm may provide stable and accurate performance compared to the conventional manual cutting approach by surgeons and the OTS approach in Chapter 3.

4.2 Contribution

The author's contributions in this Chapter include:

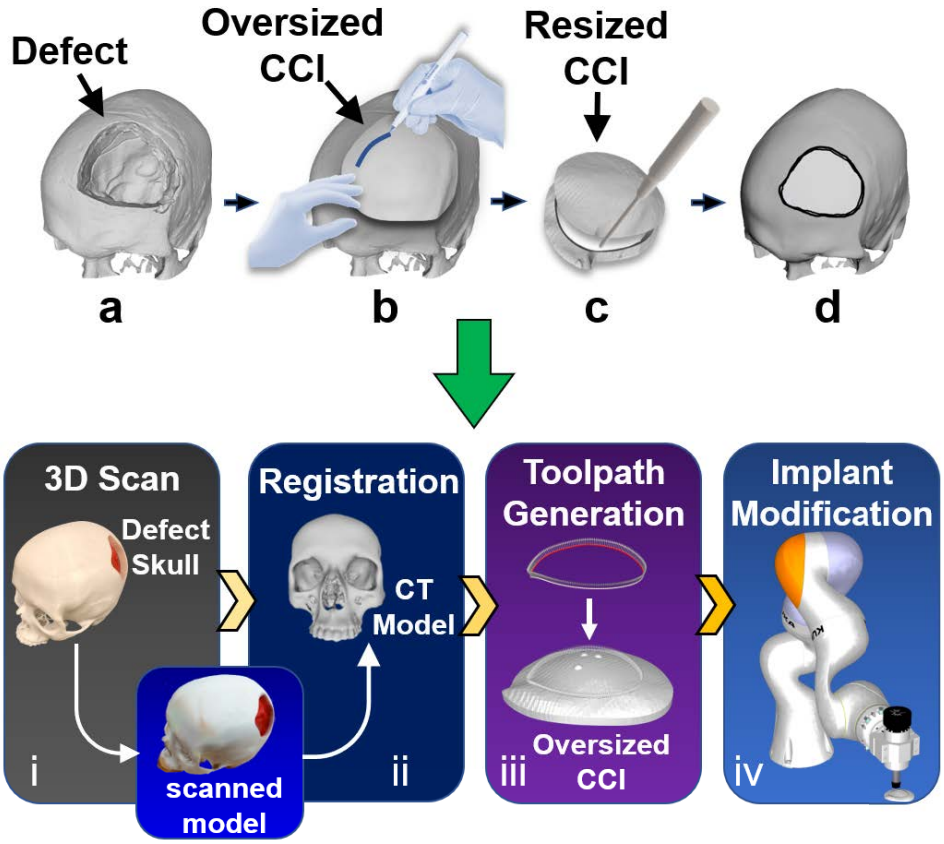

Figure 4.1: Transition from manual to automated CCI resizing Top: A clinical example of the single-stage cranioplasty with a prefabricated oversized CCI: a) the surgeon marks the defect contour on the CCI. b) the implant is manually modified by a surgical cutter. c) the resized CCI is fit to the skull defect. Bottom: The workflow of robotic single-stage cranioplasty: i) 3D scanning generates a scanned model of the defect skull. ii) the scanned model is registered to the preoperative CT model. iii) a cutting toolpath is generated. iv) a cutting robot modifies the implant.

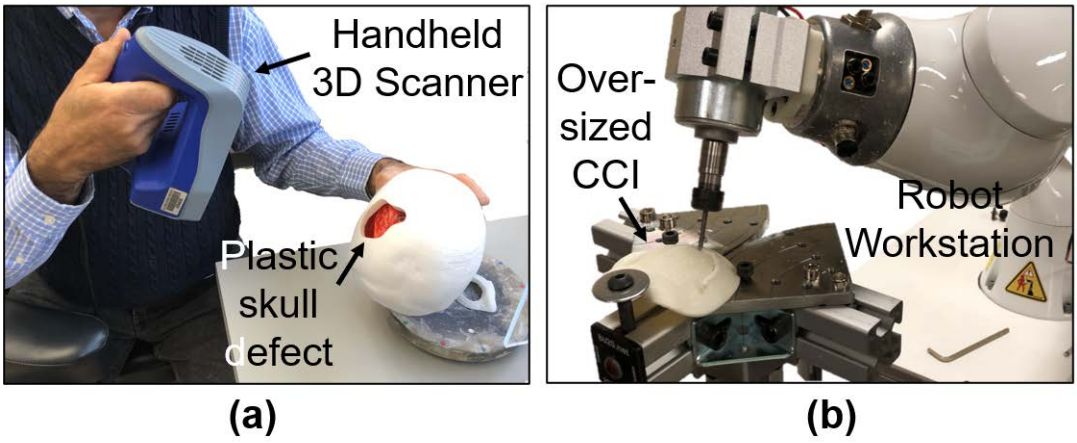

Figure 4.2: Intraoperative data acquisition via 3D scanning and robotic CCI modification Left: The plastic defect skull is scanned by a handheld 3D scanner. Right: robot resizes the oversized implant.

- Introducing a fast and non-contact approach for acquiring defect information using a handheld 3D scanner.
- Developing a toolpath algorithm for generating robot's cutting toolpath from extracting defect contours.
- Integrating a robotic system for resizing oversized CCIs.

Mr. Wei-Lun Huang helped the author in implementing a portion of the toolpath algorithm and assisted in the evaluation experiments. The work in this Chapter was published in the Proceedings of IEEE International Conference on Robotics and Automation (ICRA) 2021 [60].

4.3 Method

A robotic system is developed for resizing oversized CCIs during intraoperative operation. The system consists of a handheld Artec Space Spider 3D

scanner (up to 0.1 mm resolution) and a KUKA LBR iiwa 7 R800 robotic arm (repeatability $\pm$0.1mm). The 3D scanner is utilized to acquire 3D information of the skull defect and to export a refined mesh. (Figure 4.2 (a)) We modify the KUKA robotic arm into a cutting workstation by attaching a spindle tool to the robot's end-effector (Figure 4.2 (b)).

Our intraoperative CCI modification method includes four steps (Figure 4.1 Bottom): **1)** The information of a defected skull is collected using a 3D scanner; **2)** The scanned data is registered to the CT model space; **3)** A cutting toolpath is generated by extracting the defect contour; **4)** A cutting robot resizes the CCI according to the generated toolpath.

4.3.1 3D reconstruction of a patient's skull defect

A 3D scanning process was first utilized to acquire intraoperative patient data. During this process, the 3D scanner was held by hand at an approximate half meter away from the skull and moved slowly around it. This process could be terminated when there were sufficient 3D data as shown in the visualization software (Artec Studio). This process usually takes less than two minutes.

4.3.2 Patient-to-CT registration

The neurosurgeon plans the skull resection based on the patient's preoperative CT. The 3D-scanned defect geometry was then registered to the preoperative CT skull model. This process transformed the 3D scanned defect geometries to the CT model space, as shown in Figure 4.3. An iterative closest points (ICP) registration method [61] was applied to refine the registration. Three

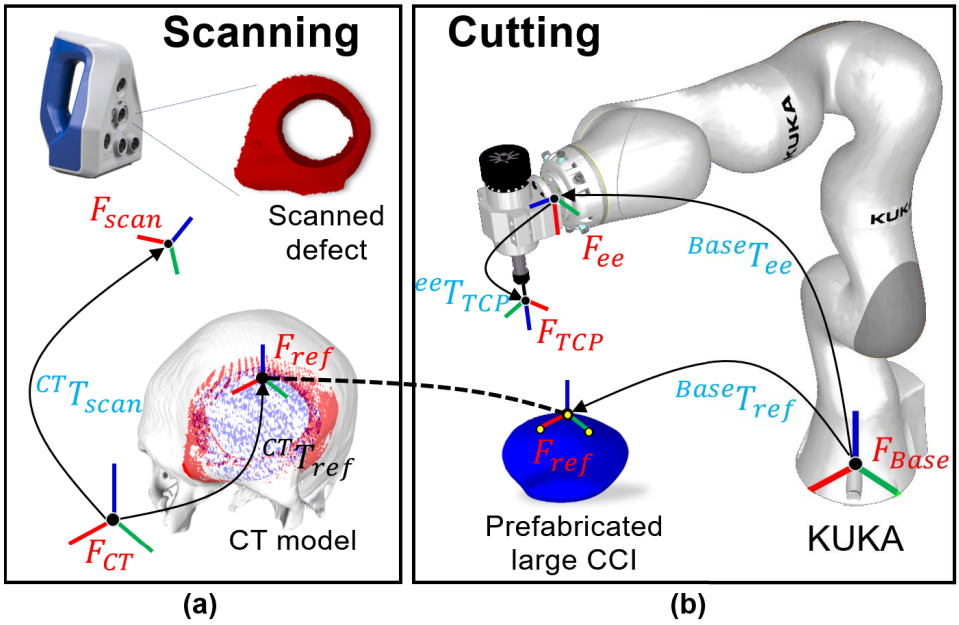

Figure 4.3: Coordinate systems transformation Left: patient-to-CT registration aligns the 3d-scanned defect mesh model (red) F_{scan} to the CT model (white) F_{CT}. Right: the robot locates a prefabricated oversized CCI (blue) by finding the reference frame F_{ref} defined by three spherical markers that originally defined in F_{CT}. F_{Base} is the robot's base frame. F_{ee} is the robot's end-effector frame. F_{TCP} is the calibrated TCP frame. The transformation between different coordinate frames are shown as T.

anatomical points were artificially designed on the defect skull and were picked from the 3d-scanned model for ICP initialization.

Since the preoperative CT model has two layers separated by the bone thickness, during the registration process, the 3d-scanned data tends to mistakenly overlap with the inner layer of the skull, because of the similar geometric feature between the inner and outer layer. To prevent this problem, we designed a preprocessing algorithm to convert the closed CT model to an open surface mesh by removing the inner layer.

In this method, we defined the 3D position of each vertex in the CT skull mesh as $\mathbf{q}_i \in \mathbb{R}^3$. The center of the mesh $\mathbf{o} \in \mathbb{R}^3$ can be approximated by: $\mathbf{o} = \frac{\sum_{i=1}^{n} \mathbf{q}_i}{n}$. Then we constructed vector $\mathbf{v}_i$, which points from the center $\mathbf{o}$ to each vertex $\mathbf{q}_i$. Since each vertex in the skull mesh is also associated with a normal vector $\mathbf{n}_i$ of its own. The vectors of the inner layer point to the hollowed space inside the skull towards the center $\mathbf{o}$, while the vectors of the outer layer point to the opposite directions. As a result, the sign of $\mathbf{q}_i \cdot \mathbf{n}_i$ determines whether this vertex is located in the inner layer or the outer layer. Vertices with negative dot products were removed to keep only the outer layer of the CT mesh model.

4.3.3 Toolpath Generation

To generate a toolpath for the subsequent resizing process, the defect contour was first extracted from the 3d-scanned mesh of the skull defect. Then, the 3d-scanned defect was registered to the preoperative CT model. Therefore, the implant was aligned to the 3d-scanned defect model in the CT coordinates. A

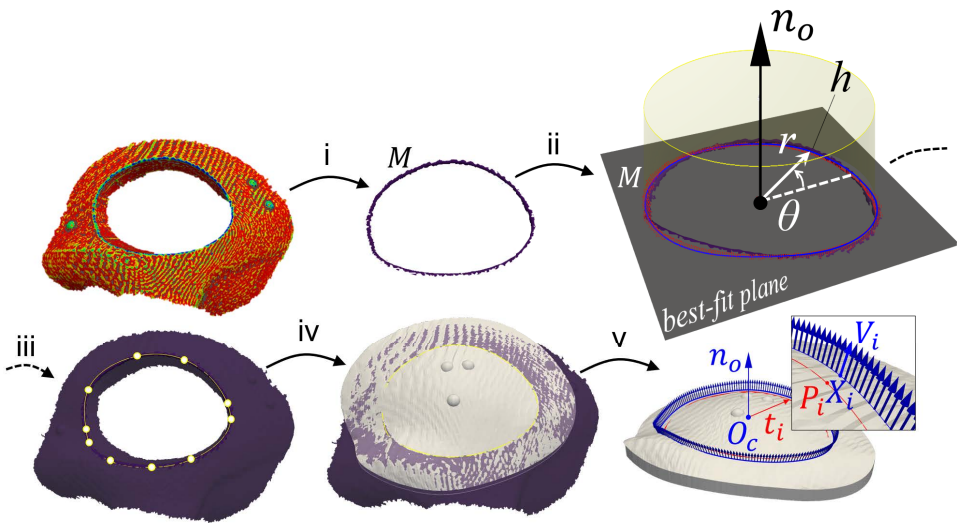

Figure 4.4: Toolpath generation (i) A curvature filter followed by manual cleaning is applied to the 3d-scanned defect data to extract the vertices of the defect contour. (ii) The remaining vertices are fitted to a plane, transformed to a local cylindrical coordinate system defined on the plane parameterized as $(\theta,\ r,\ h)$, and then fitted to a polynomial curve. (iii) The fitted curve is converted into a spline curve interpolated through control points. (iv) The control points are projected onto the registered implant's top surface. (v) A cutting toolpath is generated from the spline curve.

toolpath consisting of cutting positions and vectors along the extracted contour was generated in the implant coordinate system, as shown in Figure 4.4. We implemented the following steps to generate 3D cutting toolpath with visualization using Pyvista [62]:

4.3.3.1 Curvature Filter

To extract the contour of the defect, a curvature filter was applied to the vertices of the 3d-scanned mesh and followed by manual cleaning. We utilized a curvature filter to determine the local mean curvature along the surface of the defect and extracted the high curvature value above a designed threshold. The mean curvature H was calculated as $H = \frac{1}{2}(\kappa_1 + \kappa_2)$, where κ_1 and κ_2 are the maximum and minimum values of the principal curvature on the mesh [63]. This filter was able to identify crease changes by the curvature of the surface mesh. After curvature filtering, only the vertices near the dropping edges were kept (Figure 4.4, i). Additional manual cleaning was performed to further remove potential redundant vertices that were far off the edge.

4.3.3.2 Curve Fitting

After removing all the redundant vertices, a group of vertices around the defect edge were remained denoted as M (Figure 4.4, ii). We defined a local cylindrical coordinate system on a best-fit plane of the extracted contour parameterized as $(\theta,\ r,\ h)$. The center of the cylindrical coordinate system was obtained by the mean coordinates of the remaining vertices. A nonlinear least-squares method was then used to fit a closed polynomial curve to these vertices expressed in the cylindrical coordinates.

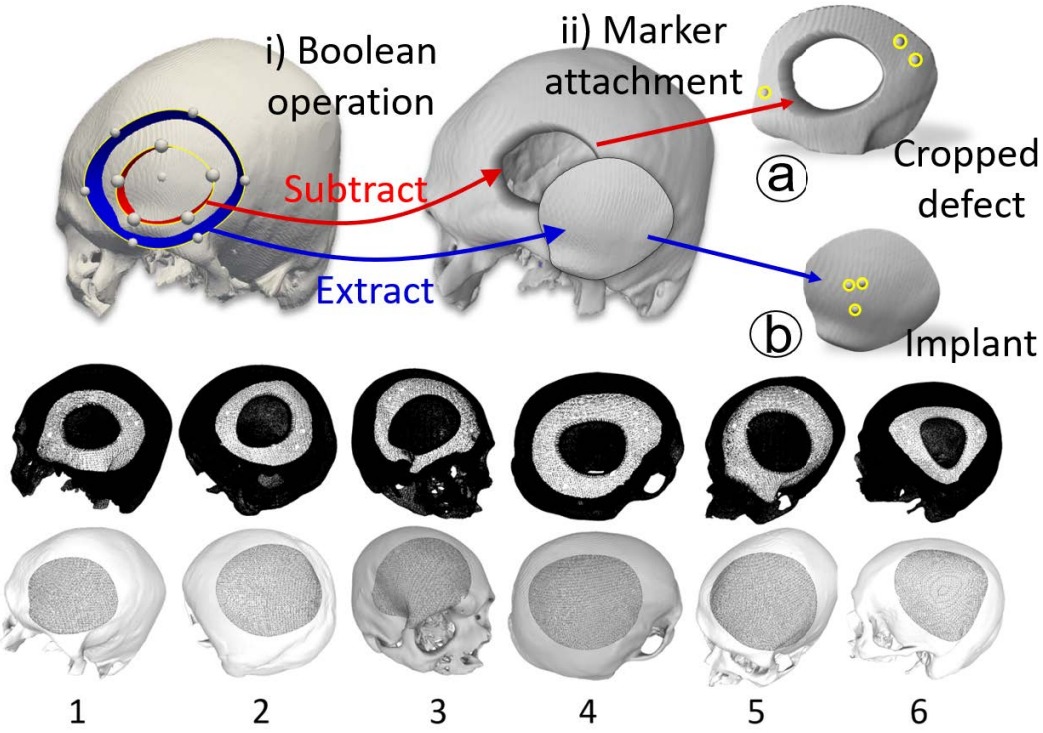

Figure 4.5: Implant and defect generation Top: the skull defect (a) and the implant (b) are generated by (1) a boolean operation between the skull and two customized contours (red contour: skull defect, blue contour: implant) and (2) attaching spherical markers to their surfaces. The skull defect is cropped to a 3-D printable size. Bottom: the skull defects (top) and implants (bottom) for six different specimens are generated.

4.3.3.3 Spline Projection

The fitted curve was then converted into a spline curve, which consists of several control points along the curve. Although the 3d-scanned defect was registered to the CT model after patient-to-CT registration, the extracted defect contour may not perfectly align to the implant's top surface due to the registration error. To eliminate the error, the control points were projected onto the top surface of the implant mesh so that the spline curve would adjust its shape to match the curvature of the implant's top surface (Figure 4.4, iv).

4.3.3.4 Toolpath Generation

For each discretized point $\mathbf{P_i}$ of the spline curve, a unit 3D vector $\mathbf{V_i}$ was added to define the tool center point (TCP)'s axis orientation. Each $\mathbf{V_i}$ was computed by tilting a constant angle from $\mathbf{n_o}$, the normal vector of the best-fit plane, toward $\mathbf{t_i}$, a vector defined from the center point O_c to each curve point $\mathbf{P_i}$. A cutting toolpath was then obtained by combining each curve point $\mathbf{P_i}$ with its associated cutting vector $\mathbf{V_i}$. To compensate the tool radius, the curve points $\sum \mathbf{P_i}$ were expanded to $\sum \mathbf{X_i}$ by an offset equal to the radius of the cutting bit (Figure 4.4, v).

4.4 Experimental Setup

To evaluate the implant-resizing accuracy of our integrated system, we compared our method with the surgeon's manual-resizing method and an existing optical tracking method. We conducted six experiments with independently generated skull defects with different sizes and shapes. The defect specimens were generated using boolean operations. As shown in Figure 4.5, we first subtracted the mesh inside the red contour from a complete skull to create a defect on the skull. On the same complete skull, the implant mesh inside the blue region was extracted to create its corresponding oversized implant. The defected skull was further cropped by a plane to a 3D printable size and was fabricated using a 3D printer (Stratasys F370, ABS material). Finally, we created three spherical markers on the top surface of each cropped defect and its corresponding implant for Patient-CT registration and implant localization.

4.4.1 Method Comparison

We compared the implants generated by our method with the manual resizing method, as well as the optical tracking method used by Murphy et al. [42]. For robotic cutting, the cut depth was set to 3 mm, which is the thickness of the 3d-printed implants. The cut angle was set to 20 degrees for all the generated cutting toolpaths to generate beveled boundaries.

4.4.1.1 Manual resizing method

We provided an expert neuroplastic surgeon six partial skulls with defects and their corresponding oversized implants. The surgeon first outlined the defect contour of each specimen manually on the implant based on his visual judgment. He then resized the implant with a hand-held cutting tool following the outline.

4.4.1.2 Optical tracking method

The optical tracking method used a digitizing instrument and an optical tracking system to trace the defect contour (Figure 4.6, a). Instead of manual resizing, the oversized implants were then resized by the same cutting robot and with the same cutting parameters described above.

4.4.2 Tool Center Point (TCP) Calibration

The transformation between the tip of the spindle tool and the robot arm's end-effector was calibrated using a pivot calibration [64]. In this method, we hand-guided the robotic arm to different poses, such that the TCP always

touches the tip of a fixed pin. The accuracy of the TCP calibration, measured by the TCP error, is shown in Figure 4.7, and the relative pose from F_{base} to F_{TCP}:

$$^{Base}T_{TCP} = {}^{Base}T_{ee} \cdot {}^{ee}T_{TCP}$$

4.4.3 Implant Localization

The oversized CCI was secured on the robot's working platform with bolts during the resizing process (Figure 4.2 (b)). In order to obtain the relative position and orientation of the oversized CCI in the robot space (Figure 4.3 (b)), we hand-guided the robot's spindle TCP to touch the tip of each spherical marker separately so that the locations of the reference markers defined in F_{ref} could be transformed to robot's frame F_{Base}. The registration between the robot space and CT space was then achieved based on the known locations of the markers, described in the F_{Base} and in the F_{CT} respectively.

4.4.4 Hardware Details

The integrated system was set up on a computer running Intel Core i7-6820HQ @ 2.7GHz CPU. The 3D scanner (Artec Spider) collects data at 15 HZ. The KUKKA robot is operated using online mode via RoboDK [1]. The registration between the 3D-scanned model and the CT model was implemented in Meshlab [65], open-source software for mesh processing. The NDI Polaris optical tracking system operates at 10 Hz (± 0.3 mm tracking accuracy) was used in the comparison experiment.

[1]RoboDK is an offline programming and simulation software for industrial robots. https://robodk.com/

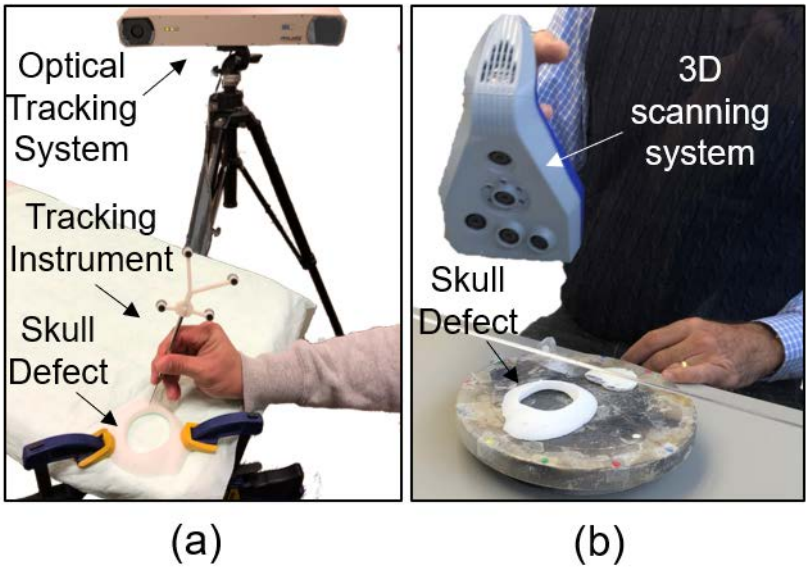

Figure 4.6: Experiment setup a) collecting the defect contour by optical tracking system. b) scanning the defect contour with a handheld 3D scanner.

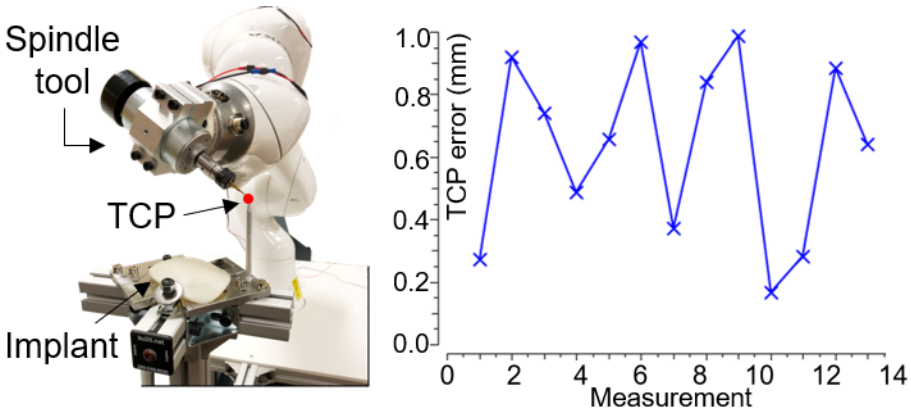

Figure 4.7: Pivot calibration robot TCP calibration errors.

4.5 Result

4.5.1 Registration

4.5.1.1 Optical Tracking Method

Three anatomical markers were artificially added to the original CT models and were 3D printed with the defect specimens. The anatomical points on the printed specimens were localized in the optical tracking system with a tracking instrument (Figure 4.6 (a)). Each defect specimen was registered back to the CT coordinate system using point set registration based on singular value decomposition [59]. The registration error was given by the mean Cartesian distance between the registered anatomical points and the original anatomical points defined in the CT space (Table 4.1).

4.5.1.2 3D Scanning Method

After 3D scanning the defect specimen, we first manually aligned the three anatomical points on the defect with the original anatomical points defined in the CT model as an initialization. Then ICP was used to fine-tune the registration of the scanned specimen to the original CT model. The error was evaluated by calculating the mean distance between all of the valid vertices and their closest vertices in the original CT model (Table 4.1).

4.5.2 Resizing Accuracy

The post-completed implants were physically fitted to the defect specimens. First, we scanned the implants sitting on their respective defects with a 3D

Table 4.1: Registration Errors of Two Methods

Specimen	1	2	3	4	5	6
Optical Tracking Point Set Registration (mm)	0.39	0.38	0.32	0.32	0.30	0.34
3D Scanning ICP (mm)	0.04	0.02	0.04	0.04	0.05	0.03

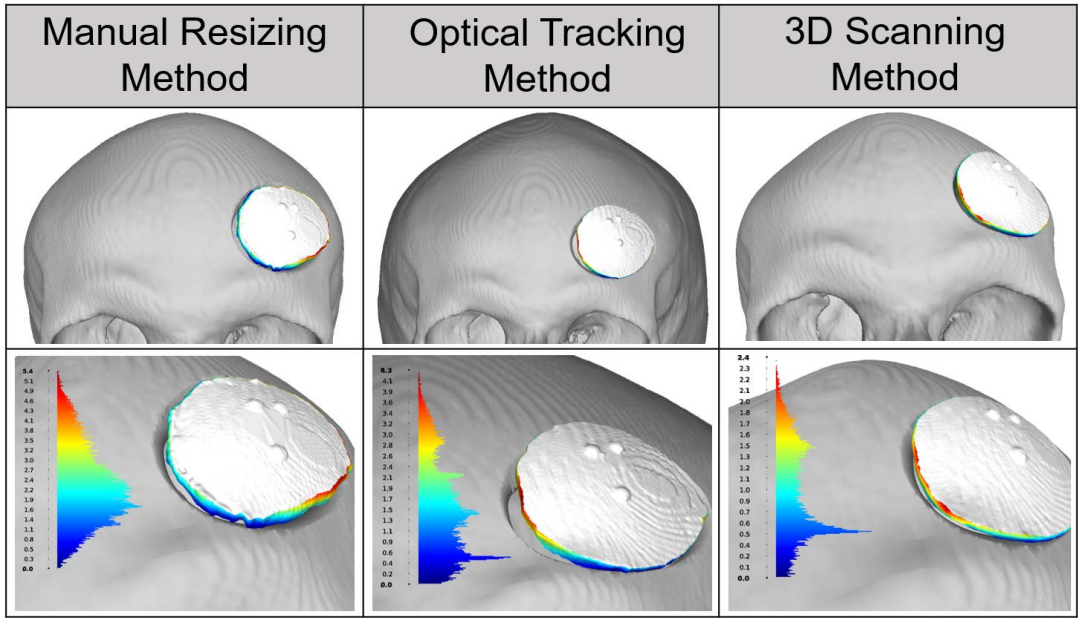

Figure 4.8: An example of gap distance analysis (specimen 1) Left, middle, right show the results of the conventional manual modification, the existing optical tracking method, and our proposed 3D scanning method, respectively. Top and bottom show their overviews and zoomed views. The color bars in the bottom plots show the gap distance between the implant's boundary and the defect edge.

scanner and registered to their original CT models using the artificial anatomical points on the defect specimens. We then 3d-scanned the post-completed implants individually and registered to the previous 3D scans using the three artificial fiducial points created on each implant so that each post-completed implant 3D model would be positioned realistically relative to the generated defect in the CT coordinate system.

We evaluated the gap distances between the boundaries of the post-completed implants and their corresponding defect edges. The gap distances were visualized in Meshlab [65] (Figure 4.8). We used the gap distance distribution (maximum, mean, and standard deviation) to quantify the error for each method for the 6 specimens. Figure 4.9 shows the analysis of the max gap distance. For the manual resizing method, all the resized implants were smaller than the defect edges since the surgeon would repeatedly trim the implant until it fits into the defect. Yet, for optical tracking and 3D scanning methods, the post-completed implant could be slightly larger than the defect boundaries, which would not completely fit into the defect.

Among the six defect specimens, the third specimen was considered the most difficult case due to the complex shape above the eye orbit. Although the gap analysis for our proposed approach showed the fourth and the sixth specimens had larger maximum bone gaps than the third specimen, this corresponds to the fact that the resized implant for this two cases did not completely fit into the defect as the post-completed implant's boundary may slightly overshoot the defect's edge. Among the mentioned three methods, Figure 4.10 shows that our proposed 3D scanning method with robotic integration was

the only one with the mean gap distance below 1.5 mm.

4.5.3 Time

Table 4.2: Time spent in each step (minutes)

	Optical Tracking	3D Scanning	Manual
Data Acquisition & Registration	3 - 6	4 - 8	-
Toolpath Generation	-	2 - 3	-
Implant Localization	4 - 8		-
CCI Resizing	3 - 5		10 - 80

4.6 Summary and Discussion

A novel method of intraoperatively resizing oversized CCIs is presented for single-stage cranioplasty. In this proposed method, first, the defect is scanned to create a mesh model. The mesh model is then registered to the reconstructed 3D model from the preoperative CT to define the defect's contour in the CT space. Next, a cutting toolpath is generated using a discrete spline curve to represent the defect contour. After localizing the oversized CCI with respect to the robot's base frame, the cutting robot automatically resizes the implant to generate the final shape to fit the defect.

The proposed method improves the accuracy of the cut by 56% compared to the surgeon's cut and 42% compared to the optical tracking method. Moreover, the implant cut boundaries created by the robot were considerably

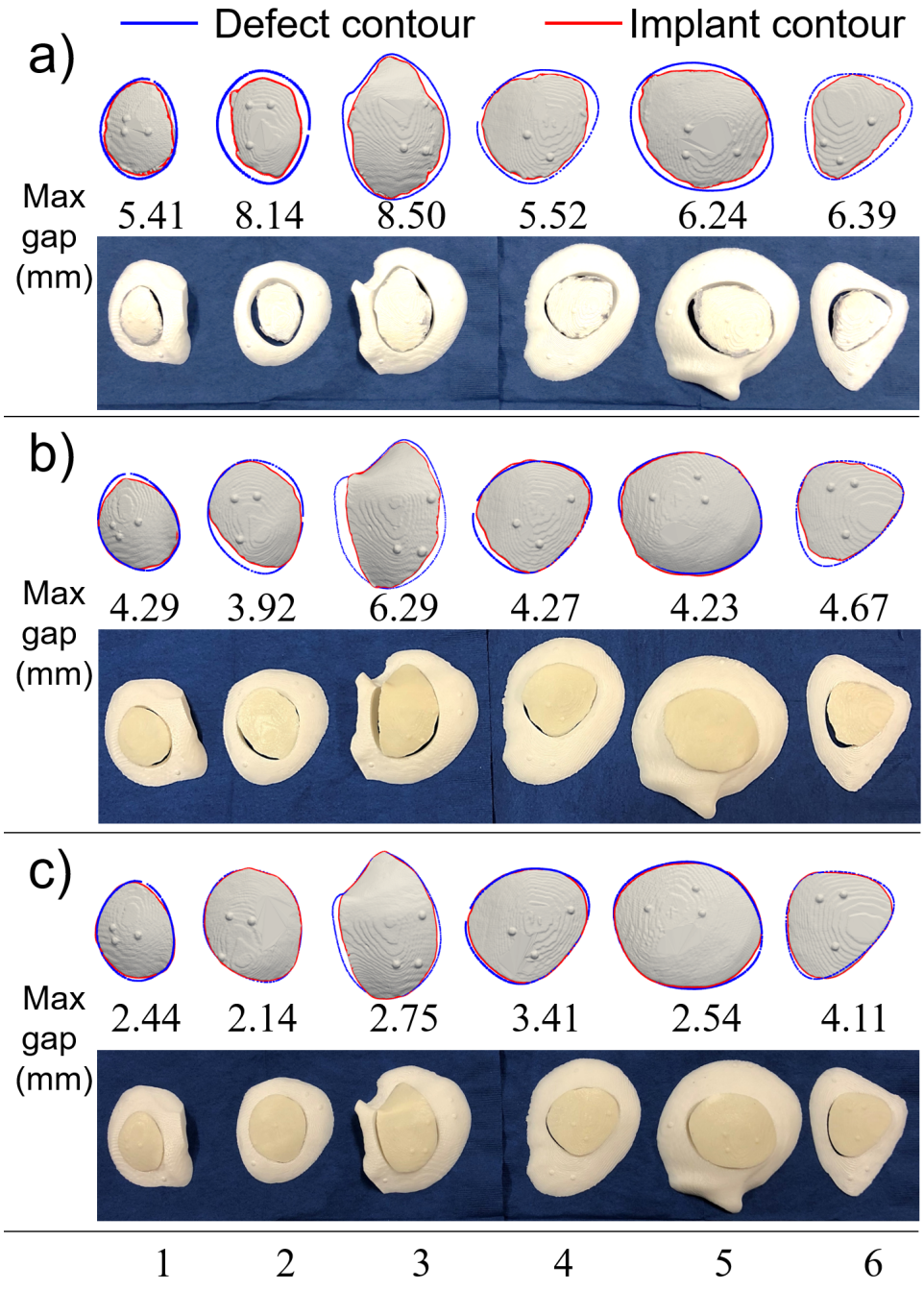

Figure 4.9: Maximum gap distance Visualization of the defect contour (blue curve) and implant contour (red curve) for a) conventional manual modification, b) optical tracking method, and c) 3D scanning method. The numbers in the middle of each plot show the maximum gap distance.

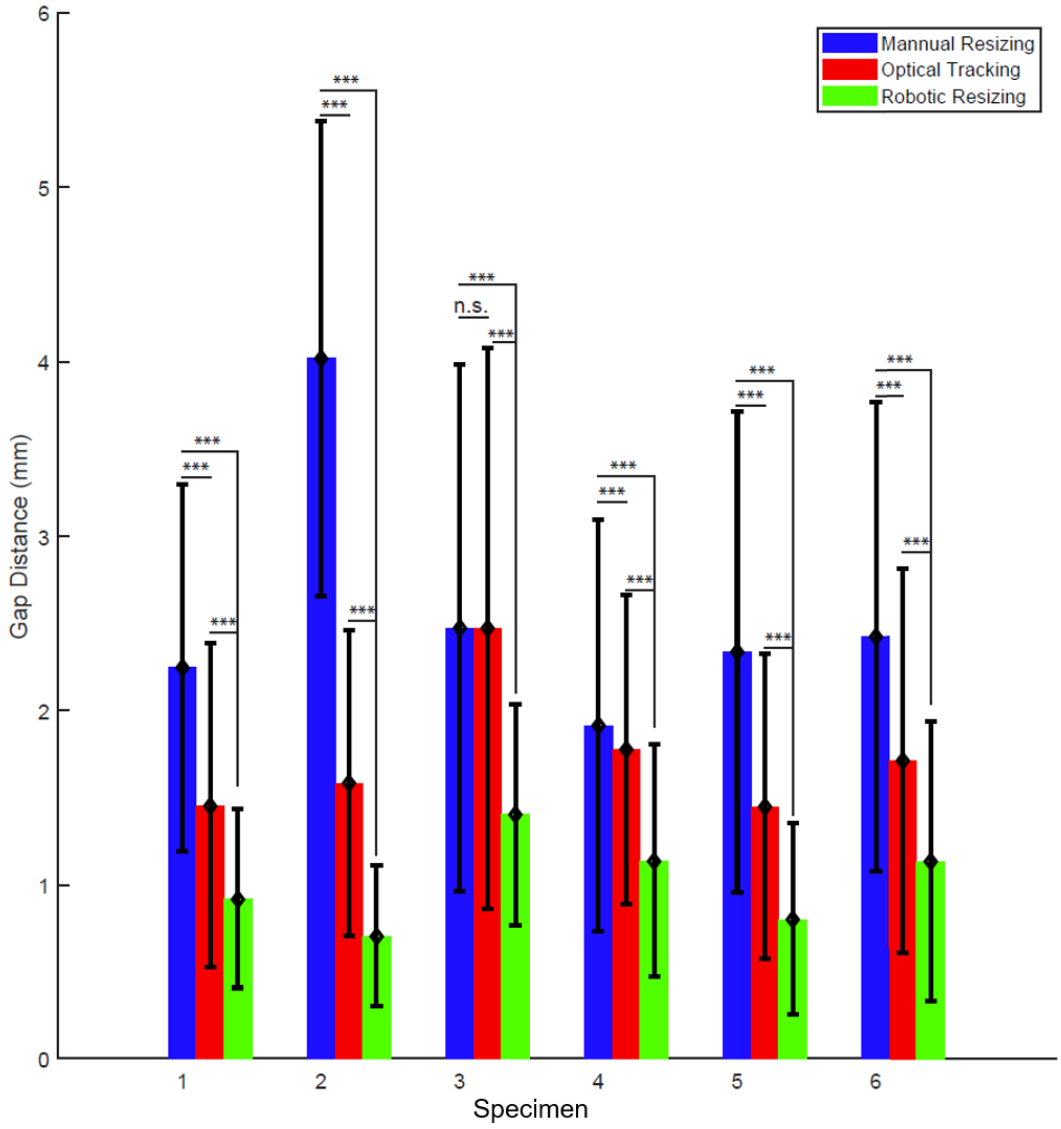

Figure 4.10: Mean gap distance The bar plot shows the mean gap distance between the skull and the resized implant by conventional manual resizing (blue), optical tracking method (red), and robotic resizing (green) for six specimens. The error bars show their standard deviations. p-value is calculated based on two-sample student's t-test: n.s. $p>0.05$; *** $p<0.001$

smoother than those created by the expert surgeon. The smooth boundary may contribute to the better continuity between the skull and the implant. Additionally, our proposed method also maintains the operation time within 10 - 23 minutes whereas manual modification takes up to 80 minutes as mentioned in Chapter 2 [12]. In this study, the robotic modification of oversized CCIs is shown to be more consistent and precise compared to the expert surgeon's performance.

The registration method described in this Chapter makes it possible to automate the CCI resizing process during the single-stage cranioplasty. However, the preliminary tests were done on partial plastic skulls, and the CCIs require predefined markers. This limits the practical usage of this system. Patient's skull has more complicated geometries compared to the 3D printed partial skulls. Moreover, the underlying anatomical points for registration become unattainable due to the presence of soft tissues. Additionally, the draping requirement during the surgery makes the patient-to-CT registration almost impossible. In addition, the cutting toolpath generation, although providing an accurate fit for the 3D-printed partial skull defect, has a major limitation because of the user-input constant cutting angle. This angle does not accommodate the defect wall geometry on a real skull. This may cause the resized implant to protrude above the patient's skull. Therefore, further improvement of this robotic system is made, as described in the next Chapter.

Chapter 5

Automated Implant Resizing: Phantom and Cadaver Study

5.1 Motivation

Chapter 4 detailed the development of a robotic system for intraoperative CCI modification. The system simplifies the patient-to-CT registration via a handheld 3D scanner and automated the CCI resizing process using a cutting robot. Through the preliminary tests on 3D-printed partial plastic skulls, the robotic system demonstrated higher resizing accuracy compared to the conventional manual approach and the OTS approach. However, its clinical value was not yet fully demonstrated.

A real human skull bone has more complicated geometries than partial 3D-printed skulls. It is also nearly impossible to locate the exact anatomical features on a real patient since the skull is hidden beneath the soft tissues. Furthermore, in clinical settings, surgical draping is required to cover the patient's skull except for the surgical site, making the patient-to-CT registration even more difficult. Also, the previous toolpath algorithm required user

inputs to generate cutting vectors defined by the given tilting angle instead of conforming to the defect's beveled edge. This may result in CCI protrusion above the defect. In addition, the robot required a user's operation during CCI localization by passively hand-guiding the robot to contact at least three fiducial points defined on the CCI. However, implant manufacturers usually do not provide CCIs with predefined fiducials. Therefore, further development and more study are necessary to validate the system's feasibility toward clinical use.

This Chapter presents remedies to the emerged challenges and proposes an automated workflow for single-stage cranioplasty toward more precise and clinically feasible CCI modification.

First, to address the challenge posed by the draping requirement, a 2-scan registration method is proposed to register the 3D scanned defect model from the patient space to the CT space by using our in-house customized reattachable fiducial markers. To address the challenge posed by the soft tissues, a modified ICP was implemented to achieve patient-to-CT registration.

Second, to resolve the limitation of toolpath generation in the previous study, the toolpath generation algorithm is modified. The improved algorithm automatically aligns the cutting vectors, i.e., the robot's TCP orientations, to the defect's beveled edge. The more accurate cutoff edges minimizes the possibility of protrusion as the resized CCI attains a better fit.

Third, to eliminate the user's involvement and the additional requirement of adding predefined fiducials on the CCI, I automated the implant localization process by adding an RGB-D camera to the robot. The robot then performs

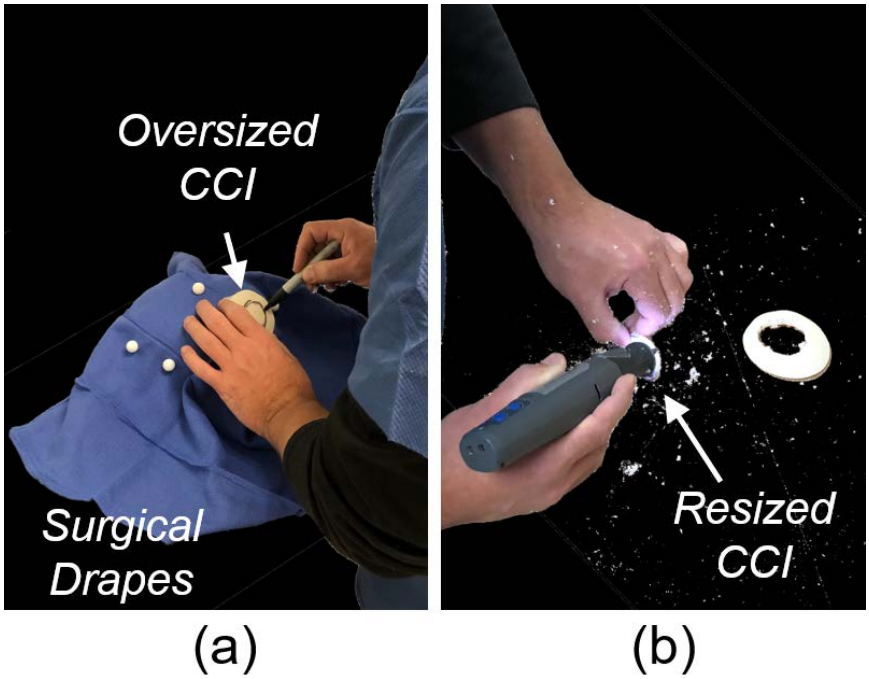

Figure 5.1: Intraoperative CCI modification by manual approach a) The surgeon marks the defect contour on the oversized CCI. b) The surgeon manually trims the oversized CCI to fit the defect.

3D scanning based on Truncated Signed Distance Function (TSDF) fusion to generate a 3D mesh of the physical implant in the robot space. This 3D implant model in the robot space can be registered to the CT space where the cutting toolpath is defined. Thus, the robot performs automatic cutting of the oversized CCI based on the given toolpath.

5.2 Contribution

The author's contributions in this chapter include:

- Introducing an automated intraoperative CCI modification workflow.

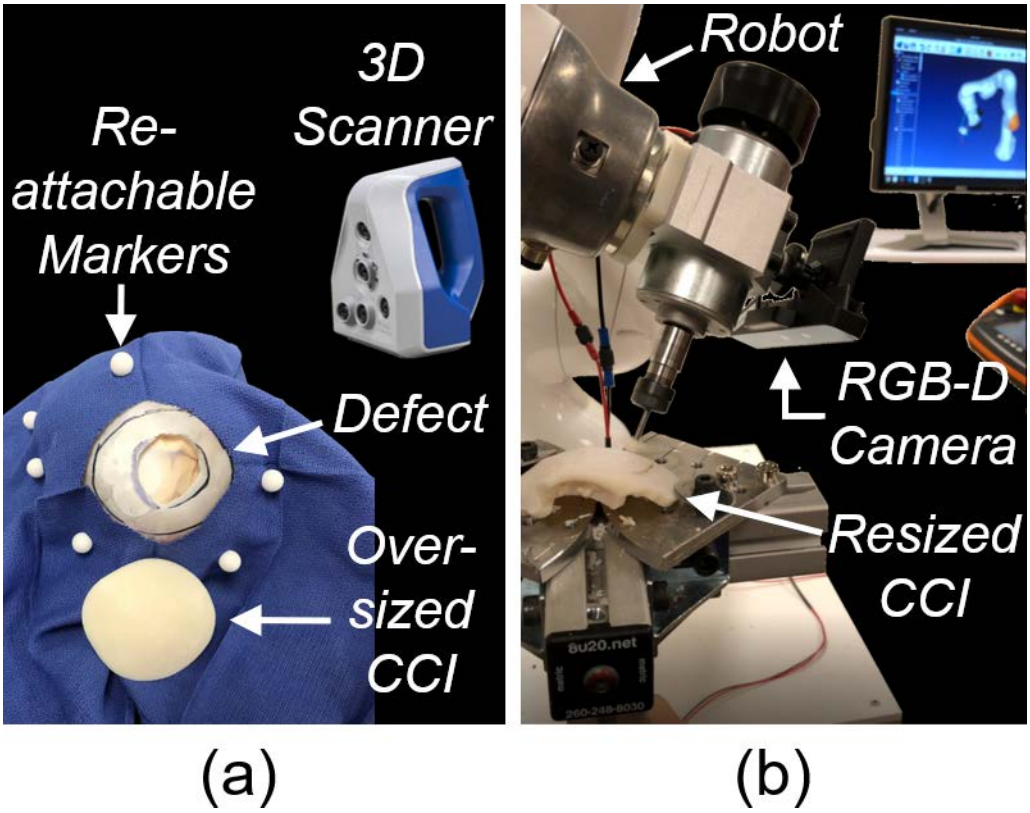

Figure 5.2: Intraoperative CCI modification by proposed automated approach a) A handheld 3D scanner scans the cranial defect with reattachable fiducial markers above the surgical drapes. b) A robot mounted with an RGB-D camera automatically localizes and resizes the oversized CCI to fit the defect.

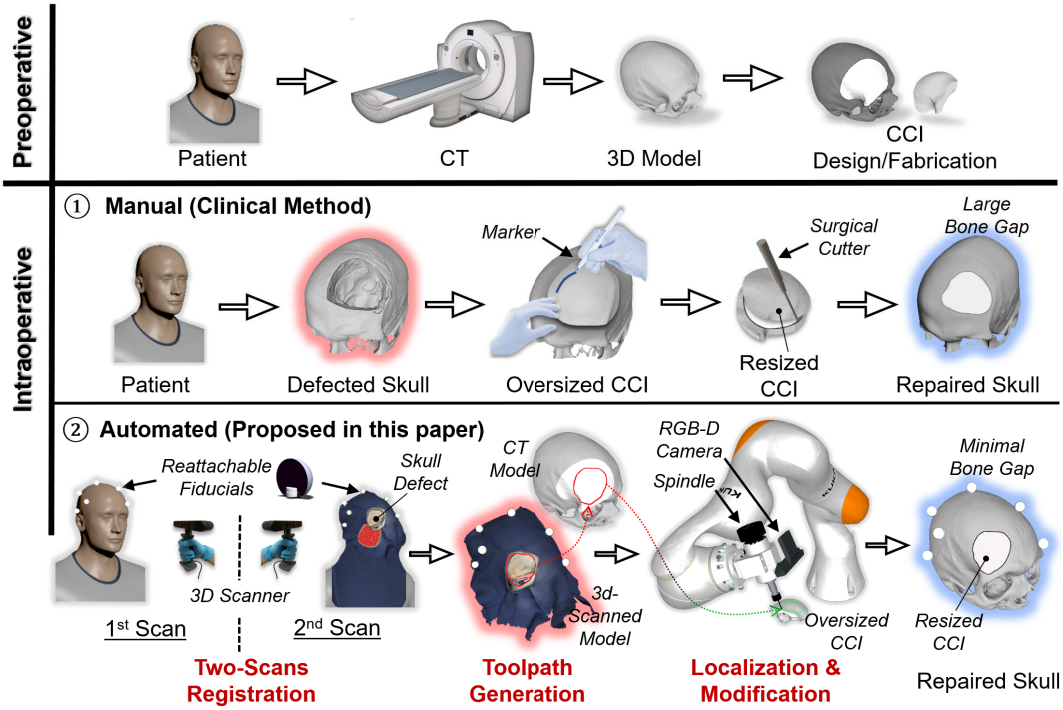

Figure 5.3: Two workflows of single-stage cranioplasty Top: A patient-specific oversized CCI is designed based on the preoperative CT. Bottom: intraoperative CCI modification by ① **Manual** vs. ② **Automated** approach.

- Proposing a 2-scan method for patient-to-CT registration addressing the challenge posed by the clinical draping requirement using reattachable fiducial markers.
- Proposing a modified ICP for patient-to-CT registration addressing the challenges of the soft tissues.
- Futher improving the toolpath generation algorithm proposed in Chapter 4 to consider the defect's beveled edge to attain closer fit.
- Further automating the robotic system developed in Chapter 4 to localize CCI via robotic 3D scanning using an RGB-D camera in a faster and more reliable fashion.
- Evaluating the resizing accuracy of the system on two full plastic skulls and two cadavers, in comparison to the partial plastic skulls used in Chapter 4, to show more convincing results of the proposed system's clinical feasibility.

Mr. Wei-Lun Huang helped the author in improving the toolpath algorithm and assisted in cadaver experiments. The work reported in this chapter was published in the IEEE Robotics and Automation Letters (RA-L), vol. 6, no. 4, 2021 [66].

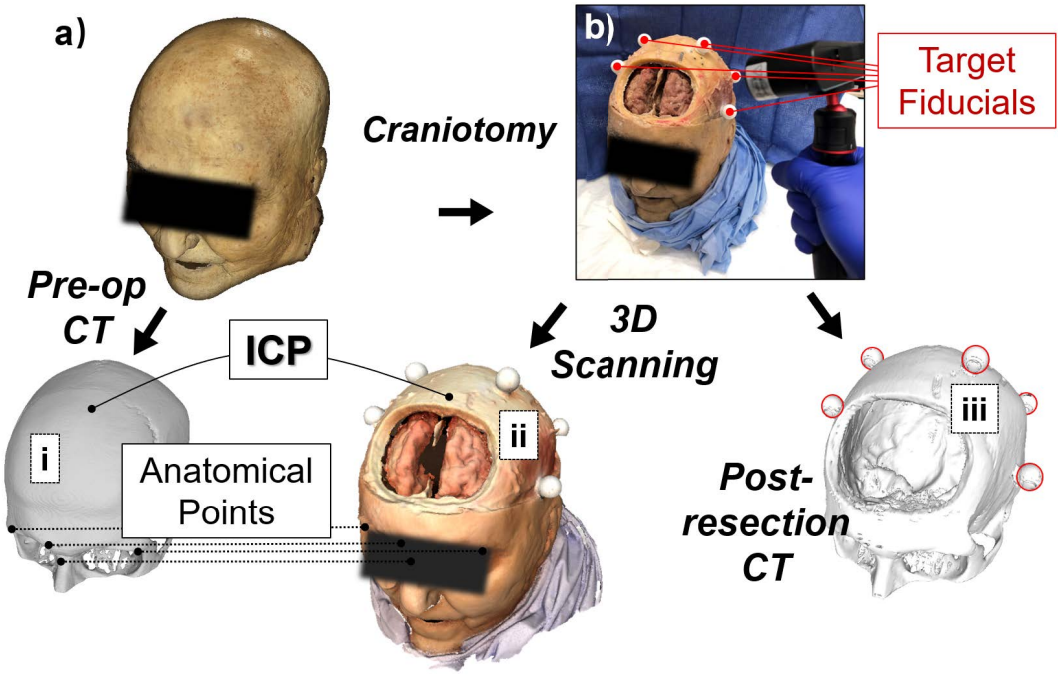

Figure 5.4: Patient-to-CT registration without draping a) Cadaver. b) Performing 3D scanning generated a 3D head/defect model (ii). Five spherical fiducials were attached for evaluating TRE. The preoperative skull model (i) and the post-resection skull model (iii) were obtained via CT scan. ICP was utilized to register the head/defect model (ii) to the skull model (i).

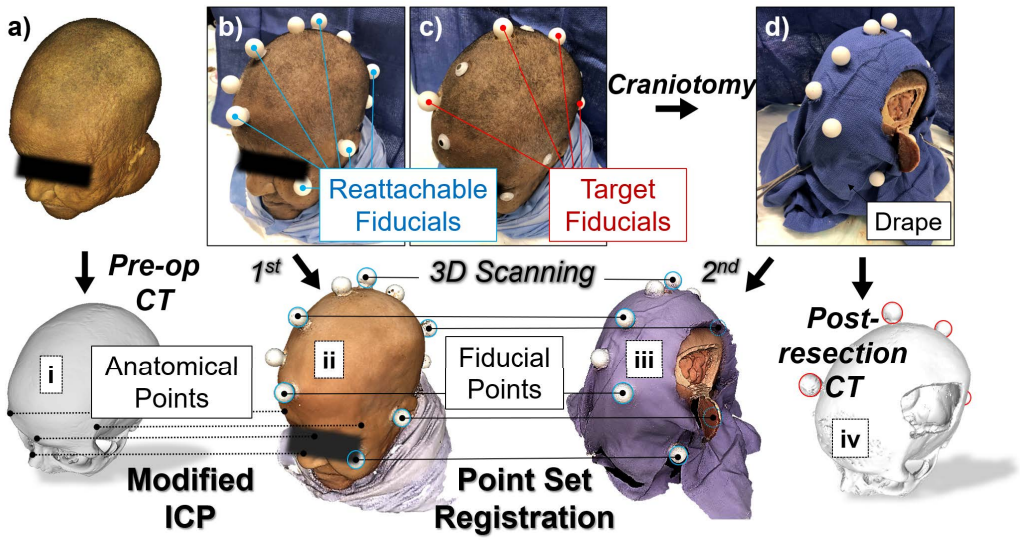

Figure 5.5: Patient-to-CT registration by 2-scan method with draping a) Cadaver. b) Performing 1^{st} 3D scanning generated a 3D head model (ii). Six reattachable fiducials were adhered to the skin for point set registration. c) Five rigid fiducials were attached for evaluating TRE. d) Performing 2^{nd} 3D scanning after draping and craniotomy generated a 3D defect model. The preoperative skull model (i) and the post-resection skull model (iv) were obtained via CT scan. Modified ICP and point set registration were utilized to register the defect model (iii) to the skull model (i).

5.3 Method

5.3.1 Patient-to-CT Registration

The patient-to-CT registration transforms the cranial defect information from the patient space to the preoperative CT space. To acquire cranial defect data, a handheld 3D scanner was used to scan the skull defects. To evaluate the registration accuracy, post-resection CT skull models were obtained with target fiducials attached.

5.3.1.1 Draping Requirement

Not Required:

When surgical draping is not required, one single 3D scan is sufficient to attain patient-to-CT registration (Figure 5.4). We first utilized anatomical points to roughly align the patient's head model (ii) to the CT model (i). Afterwards, iterative closest point (ICP) [61] was applied to refine the alignment.

Required:

In most clinical cases, aseptic draping is required to cover the patient's entire head except the surgical site because of the sterilization protocol. However, the drape would block the anatomical points and prevent registration. Hence, we propose a 2-scan method to bridge the gap using our customized reattachable fiducial markers (Figure 5.5). Each marker consists of a skin-adhesive bottom plate, which remains underneath the drape throughout the procedure, and a detachable top sphere that can be reattached above the drape via two tiny embedded magnets (Figure 5.6). First, prior to draping, the patients were

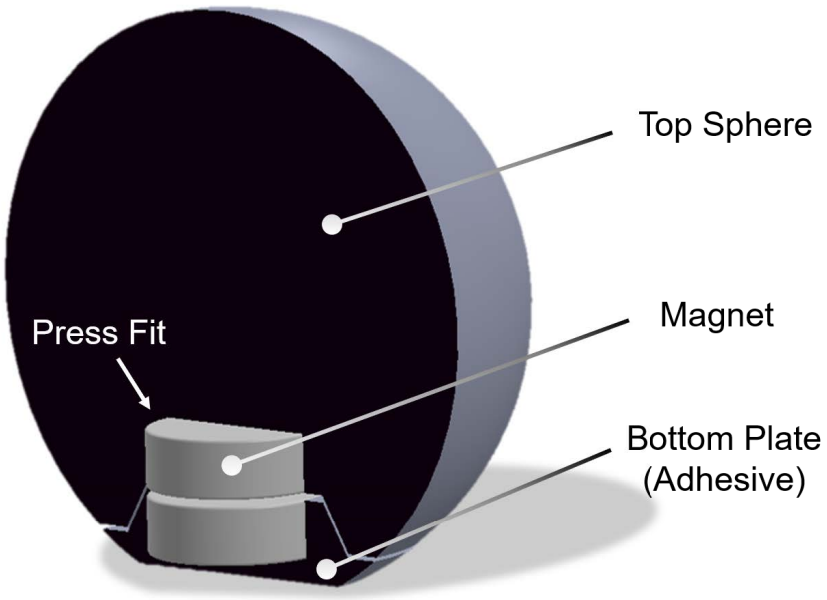

Figure 5.6: Reattachable fiducial markers The reattachable fiducial markers consists of a top sphere, a bottom plate, and two magnets. The bottom plate can be adhered to patient's skin.

3D scanned with the fiducials attached, and the 3D scanned head model (ii) was registered to the CT space (i). After draping and craniotomy, We then utilized the fiducial markers to create correspondence between the second 3D scanned defect model (iii) and the previously scanned head model (ii).

5.3.1.2 3D Scanning Procedure

Performing 3D scanning with a handheld 3D scanner is a simple process. Yet, it is important to keep the scanner at a proper distance from the scanned object according to the scanner's specifications. The user should move the scanner around the scanned object in a smooth motion while keeping the object in the center of the field of view. For optimal scanning results, the scanner should be perpendicular to any scanned surface. We used Artec Spider (a white

structured light) 3D scanner to scan plastic skulls and Revopoint POP (an infrared structured light) 3D scanner to scan cadaver heads. Upon completion, the scanner generates a 3D mesh model of the scanned object.

5.3.1.3 Modified ICP

ICP could be directly applied on plastic skulls for patient-to-CT registration since the 3D scanned skull model is identical to the CT model. For cadaver head, however, due to the scalp and soft tissues, normal ICP will not work. We propose a modified ICP for patient-to-CT registration (Figure 5.5): 1) The 3D scanned head model (ii) was scaled down with respect to its geometric center to cancel the thickness of the scalp and mimic the shape of the skull. 2) The down-scaled head model (ii) was then registered to the skull model (i) via ICP. 3) The head model (ii) was scaled back to its original size with respect to its center.

5.3.1.4 Point Set Registration

Reattachable fiducial markers were adhered to the patient's skin when surgical drape is required. A minimum of three fiducials are required for point set registration. We attached six reattachable fiducials to the cadaver's skin surrounding the resection area (Figure 5.5 b). The point set registration yields a rigid transformation T that maps the defect model (iii) to the CT space via the intermediate 3D scanned head model (ii) based on least-square fitting [59].

5.3.1.5 Registration Evaluation

Each fiducial marker's center was located by fitting a sphere of the given marker size. The fiducial localization error (FLE) mainly depends on the 3D scanner's resolution. The fiducial registration error (FRE) is given as the RMS over all the fiducial points used for the point set registration:

$$FRE = \sqrt{\frac{\sum_{i=1}^{n}(T \cdot \mathbf{a_i} - \mathbf{b_i})^2}{n}}$$

where T is the rigid transformation that minimizes the FRE, $\{\mathbf{a_i}, \mathbf{b_i}\}$ are the fiducial point pairs in the patient space and the CT space respectively. The most significant value for evaluating registration accuracy is the target registration error (TRE) [67]:

$$TRE = \|T \cdot \mathbf{p_a} - \mathbf{p_b}\|$$

where $\mathbf{p_a}$ is the target point in the patient space and $\mathbf{p_b}$ is its corresponding target point in the CT space.

5.3.2 Toolpath Generation

The oversized CCIs were generated from patients' preoperative CT (Figure 5.3 Top). After patient-to-CT registration, the 3D scanned defect model was registered to CCI in the CT space. Therefore, we could use the 3D scanned defect model to generate a cutting toolpath for resizing the oversized CCI. The cutting toolpath defined the TCP positions and orientations. To attain closer fit, we have improved the algorithm to consider the defect beveled edge by the following steps:

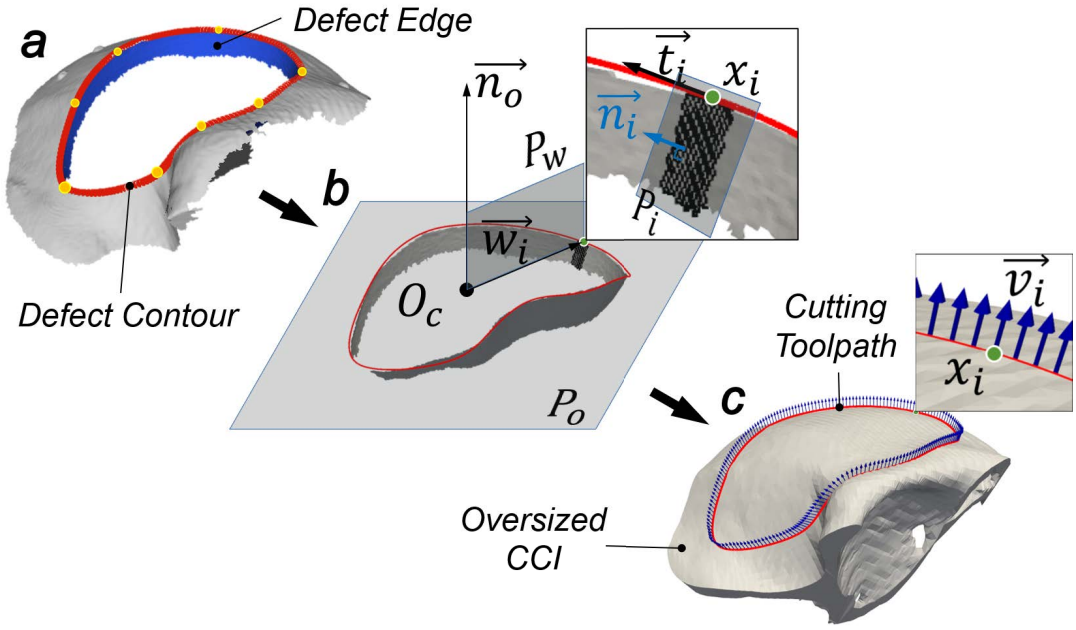

Figure 5.7: Toolpath generation algorithm a) The defect contour is represented by a spline curve (red) interpolating the control points (yellow). b) (P_o, normal $\vec{n_o}$) is the best-fit plane to the curve; Plane P_w rotates about $\vec{n_o}$ intersecting the curve at x_i; (P_i, normal $\vec{n_i}$) is the best-fit plane to the neighboring edge vertices at x_i; $\vec{t_i}$ is the tangent vector along the curve at x_i. c) $\vec{v_i} = \vec{t_i} \times \vec{n_i}$ represents the cutting vector generated at x_i.

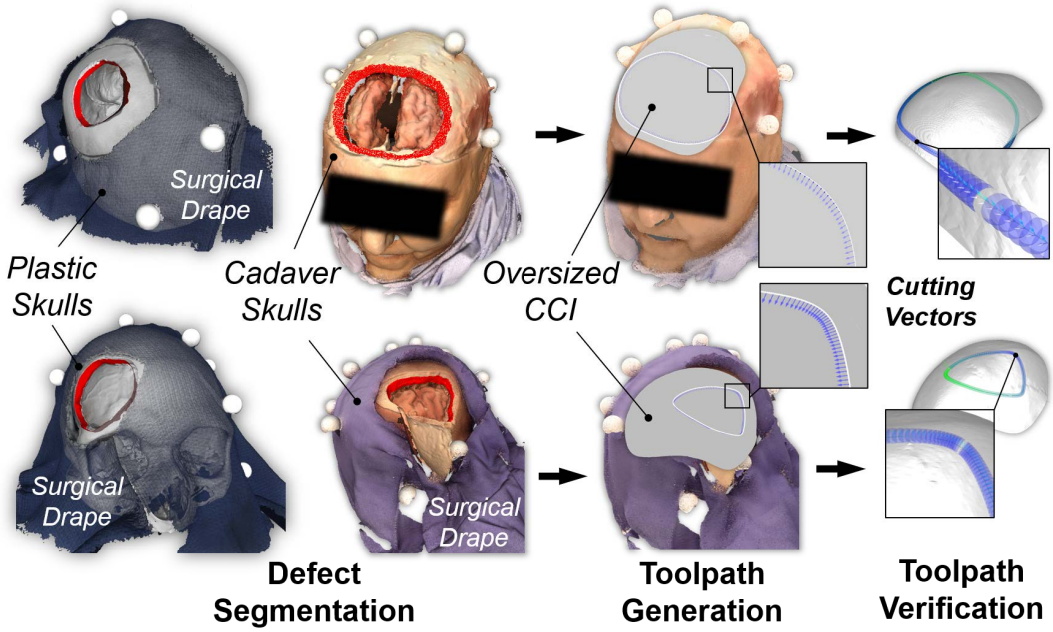

Figure 5.8: Toolpath workflow Left to right: Defect edges were segmented (plastic skulls and cadavers); Cutting toolpath was generated; After implant localization, the generated toolpath was verified with the robot kinematics in simulation before execution on the robot.

5.3.2.1 Defect Segmentation

The first step is to segment the defect contour and the defect edge from the defect model (Figure 5.7 (a)). To segment the defect contour, we followed the same procedure in [60]: a curvature filter was first applied to extract vertices with higher curvatures such as vertices close to the top edge of the defect. A spline curve was then fitted to the remaining vertices, and its shape could be further adjusted by manipulating its control points to approximate the shape of the defect contour. To segment the defect edge, we utilized the generating face group function in Meshmixer [1].

5.3.2.2 Cutting Vector Generation

The second step is to generate a cutting toolpath based on the segmented defect contour and edge. The curve points are assigned as the TCP positions. To generate TCP cutting vectors, the ideal cutting direction should be along the local tangential direction of the defect edge (Figure 5.7 (b)):

1) A plane P_o is fitted to the curve points $\sum_1^N x_i \in \mathbb{R}^3$, which gives us a normal vector $\mathbf{n_0}$. 2) At each local contour point x_i, a plane, P_w is formed by $\mathbf{n_0}$ and $\mathbf{w_i} = x_i - O_c$, in which O_c is the geometric center of the contour. The neighboring vertices associated with x_i on the defect edge are selected by dilating the intersection between P_w and contour edge with a small width. 3) A plane P_i of its normal vector $\mathbf{n_i}$ is fitted to these neighboring vertices. The TCP cutting vector is then defined as:

$$\mathbf{v_i} = \mathbf{t_i} \times \mathbf{n_i} \quad \mathbf{v_i} \in \mathbb{R}^3,\ 1 \leqslant i \leqslant N$$

[1] Autodesk Meshmixer: https://www.meshmixer.com

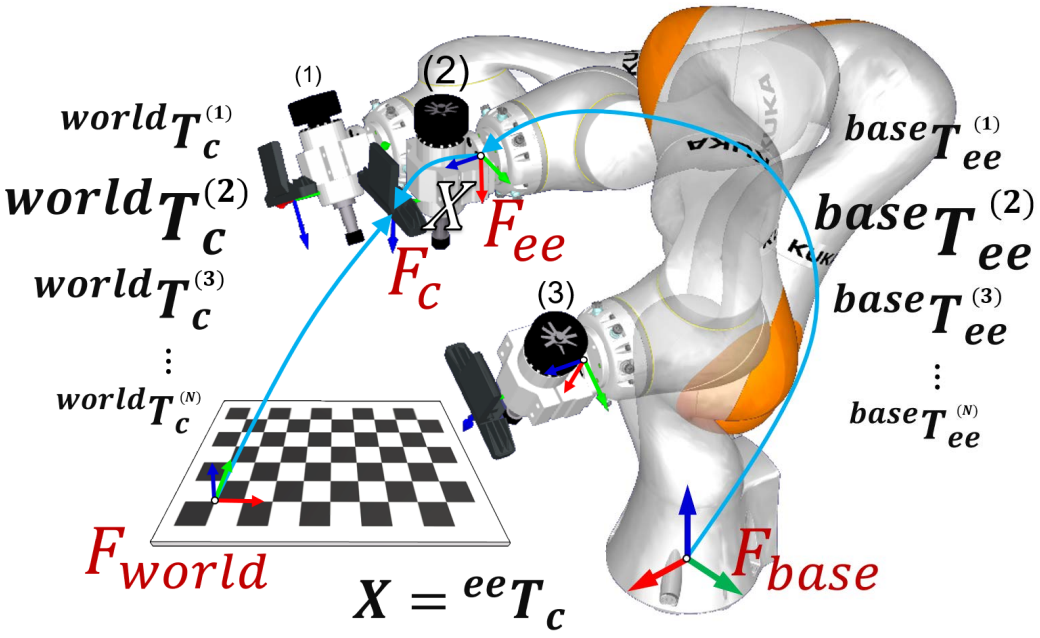

Figure 5.9: Hand-Eye calibration The robot moves to different poses ${}^{base}T_{ee}^{(1\cdots N)}$ while the camera captures images. For each image, the checkerboard's pose ${}^{world}T_c^{(1\cdots N)}$ is estimated. F_{ee} | the robot's end-effector frame; F_c | the camera frame; X | the unknown transformation to be solved.

where $\mathbf{t_i}$ is the tangent vector along the curve at point x_i.

5.3.2.3 Toolpath Projection

The third step is to project the generated toolpath onto the implant's top surface (Figure 5.7 (c)). This step could eliminate any misalignment due to registration error between the 3D scanned defect model and the implant model, and would make the generated spline curve conform to the curvature of the implant's top surface. Hence, the generated toolpath for resizing the CCI is well defined in the CT space.

5.3.2.4 Toolpath Verification

The final step is to verify the generated cutting toolpath with the robot's kinematics in simulation that all the TCPs are reachable and that no singularity occurs. In RoboDK[2], the user can verify the toolpath and adjust unreachable TCP cutting vectors when it is necessary (Figure 5.8).

5.3.3 Automatic Implant Localization

After the implant was attached on the robot's platform, the robot performed robotic 3D scanning to localize the implant. The previous method in [60] required a user to hand-guide the robot to contact at least three predefined points on the CCI. In this work, we have automated this process.

5.3.3.1 Hand-eye Calibration

An RGB-D camera (Intel RealSense SR300) was attached to the KUKA LBR iiwa 7 R800 robot (positioning accuracy: $\pm 0.1mm$ [ISO 9283]). We performed the hand-eye calibration [68] for an eye-in-hand configuration with the camera operating at 30 FPS, 1920×1080 color mode. The hand-eye calibration computes the transformation from the robot's end-effector frame to the camera frame so that the depth measurement from the camera space can be transformed to the robot space. During this process, the robot moves to 15 - 20 distinct poses to capture images of a calibration board. We used a 7×6 of square size 30 mm chessboard. With the estimated camera poses and the robot poses, the unknown transformation X can be solved by an equation of the

[2]RoboDK is an offline programming and simulation software for industrial robots

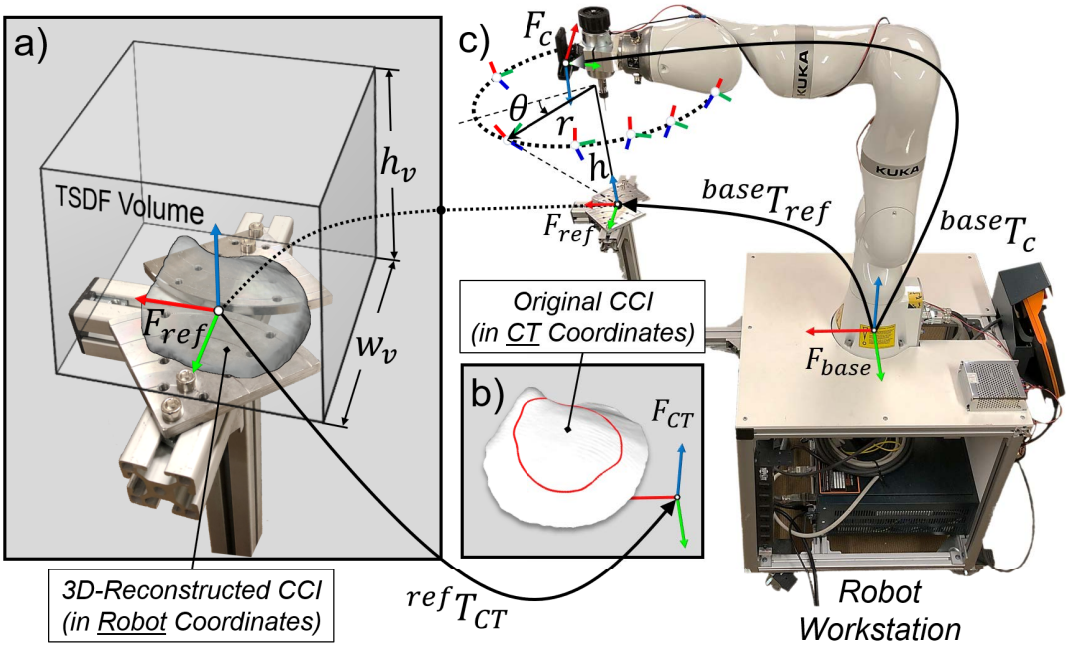

Figure 5.10: Automatic implant localization a) A 3D model of the implant is reconstructed in the robot space via TSDF fusion. b) The implant from the CT space is registered to the robot space. c) A circular path of radius r and height h above the implant is planned to perform robotic 3D scanning.

form $AX = XB$ [69] (Figure 5.9).

5.3.3.2 TSDF Fusion

The truncated signed distance function (TSDF) is a voxel-based representation of 3D space. We utilized TSDF fusion to perform 3D reconstruction of the implant by dense mapping of the acquired depth images from the RGB-D camera [70]. The camera was configured at 30 FPS, 640×480 color and depth mode, and the depth images were aligned to the color images using the Intel RealSense SDK. By fusing the images according to the camera poses calculated from the robot's kinematics, a 3D mesh model of the implant was reconstructed in the robot space.

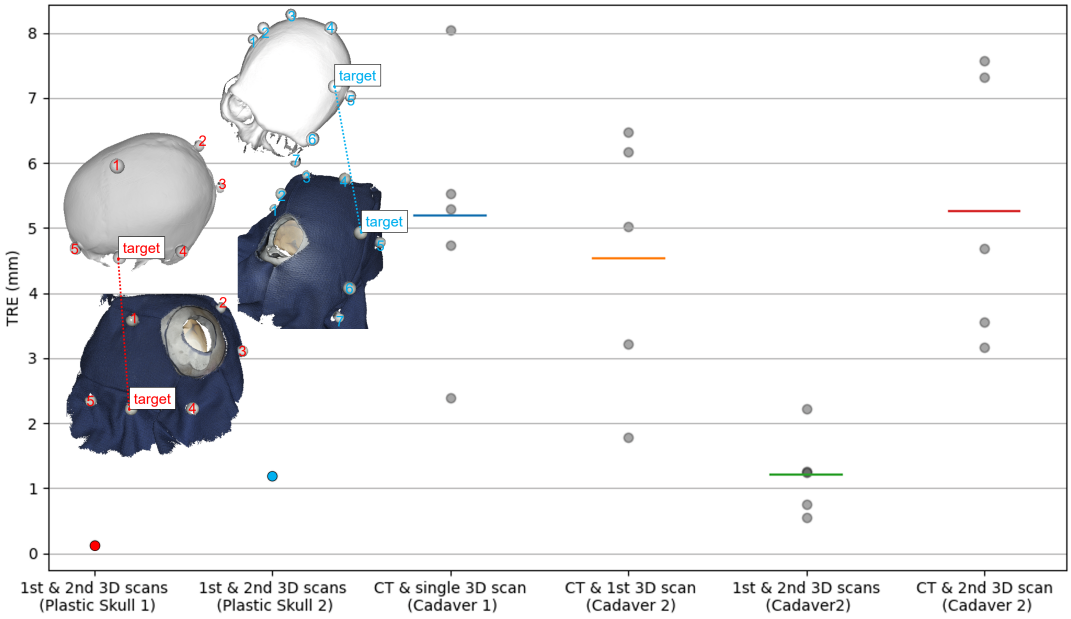

Figure 5.11: Target registration errors The dot represents the TRE of a single target; line represents the mean TRE. For each plastic skull test, the TRE was evaluated by a single target. For each cadaver test, the TRE was evaluated by five target fiducials.

5.3.3.3 CT-to-robot Registration

Once the 3D implant model in the robot space was generated, we applied the same method from the patient-to-CT registration to register the CT space to the robot space. Therefore, the generated cutting toolpath defined in the CT space could be transformed to the robot space and be executed by the robot to resize the oversized CCI.

5.4 Results and Discussion

5.4.1 Patient-to-CT Registration

In our experiments, two cadavers and two plastic skulls were tested: one cadaver was tested for the case of draping not required; the other cadaver and

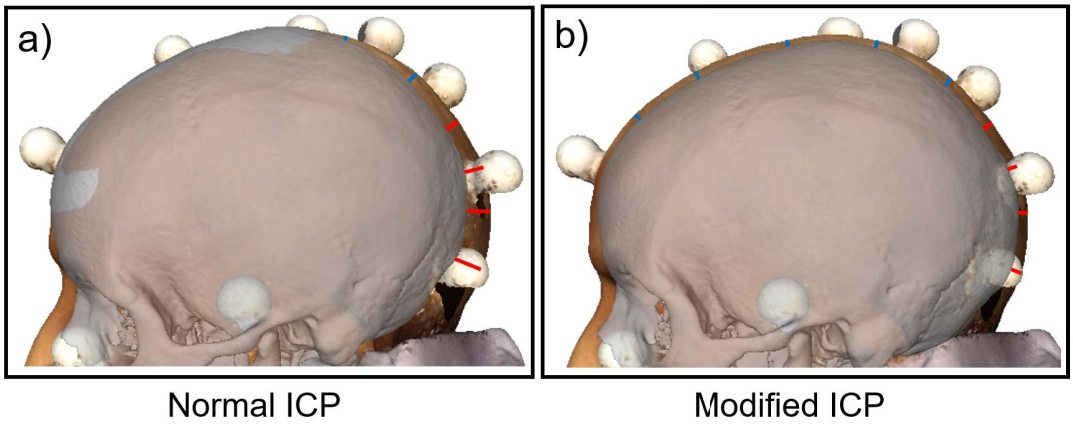

Figure 5.12: ICP vs. Modified ICP a) No gap at the frontal area; huge gap at the parietal area. b) More realistic gap at both frontal and parietal area.

the plastic skulls were tested for the case of draping required, and reattachable fiducial markers were utilized for point set registration. The FRE of the two plastic skulls were 1.004 mm and 1.149 mm respectively. The FRE of the second cadaver was 1.061 mm.

TRE was used to evaluate the patient-to-CT registration, as described in Section 5.3.1.5. Five target fiducials were rigidly attached to each cadaver head for computing TRE. The "actual" center of each target fiducial was measured from the post-resection CT. The same target points were also measured from the registered 3D scanned models.

For plastic skull tests, the TRE between the CT model and the 1st 3D scanned model were negligible because the plastic "head" model had no soft tissue and was identical to its CT model. The TRE between the 1st and 2nd 3D scanned models of the two plastic skulls were 0.136 mm and 1.196 mm respectively with one target point, and, of the second cadaver, it averaged 1.204 mm (Figure 5.11).

For cadaver head tests, the modified ICP was applied for registration, as described in Section 5.3.1.3. After the initial alignment by using the anatomical points, the normal ICP would only align the frontal area, leaving a huge gap at the parietal area. We computed the TRE by normal ICP that was 15.571 mm, whereas by modified ICP it was 4.534 mm. Therefore, the registration error was considerably reduced by our modified ICP (Figure 5.12).

In the case of no draping required, the normal ICP could be applied when a large portion of the skull were exposed. The TRE between the CT model and the 3D scanned head model of the first cadaver was 5.199 mm.

5.4.2 Implant Localization

A circular path ($r = 100mm$, $h = 300mm$) above the robot's implant platform was planned to perform robotic 3D scanning (Figure 5.10 (c)). To evaluate the localization accuracy, we designed a testing device that consisted of three ball sockets (Figure 5.13 (a)). The inserting ball of the device could also be used as a ball probe. The socket ball centers were measured from the 3D reconstructed TSDF model and from the robot's kinematics by hand-guiding the ball probe to contact each socket. Since the two measured locations ideally should be the same, the TSDF fusion error was quantified by the average points difference, which was 2.130 mm. This error may vary depending on the camera calibration, the hand-eye calibration, the depth camera accuracy and the robot's TCP pivot calibration. To minimize this error, a rigid transformation T

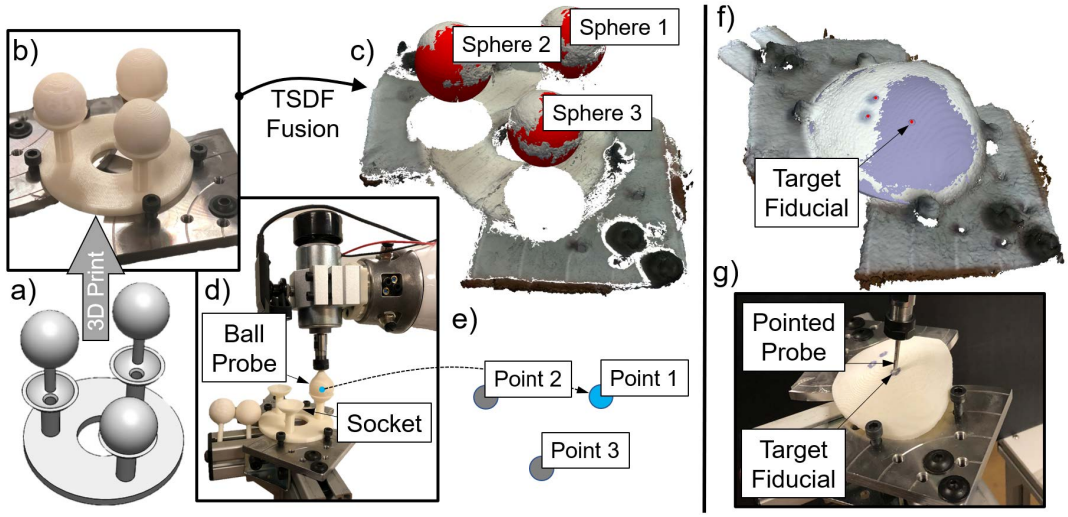

Figure 5.13: TSDF fusion accuracy evaluation Left: a) A testing device consists of three semispherical sockets and insertion balls for evaluating TSDF fusion. b) The 3D printed device was installed on the robot's platform. c) The spheres' centers were estimated from the 3D reconstructed model. d) The insertion ball was attached to the robot as a probe and its center was estimated via pivot calibration. e) The sockets' centers were located by robot contacting with the ball probe. Right: f) An implant with three target fiducials was reconstructed in the robot space. g) Each target fiducial was located by robot contacting with the pointed probe.

was applied based on least-squares using SVD [59]:

$$\arg\min_{T} \sqrt{\sum_{i=1}^{n} \frac{(T \cdot a_i - b_i)^2}{n}}$$

where $\{a_i, b_i\}$ are the measured locations by TSDF and hand-guiding respectively. After applying this transformation, the TSDF fusion error was reduced to 0.345 mm.

To verify the implant localization accuracy, we placed an implant with three known fiducials on the robot's platform. A 3D mesh model of the implant was generated in the robot's space via robotic 3D scanning. The three fiducials on the implant were also located by hand-guiding the robot using a pointed probe. The implant localization error based on this three points was 0.395 mm (Figure 5.13 (f, g)).

5.4.3 Overall Time

We compared the amount of time spent by our approach to the manual approach. Berli et al. reported the manual modification took a range of time between ten and eighty minutes in seven surgeries [12]. In our experiments, the expert surgeon spent about ten to thirty minutes, which conformed to the lower range of that time span. However, many unforeseeable factors could affect the manual approach's time such as the surgeon's skill, defect location, implant size and its shape complexity etc. Yet, our proposed approach consistently took about ten to fifteen minutes regardless of the complexity of the shape. All the calibrations could be performed prior to the surgery, and the automatic implant localization is significantly faster and more repeatable

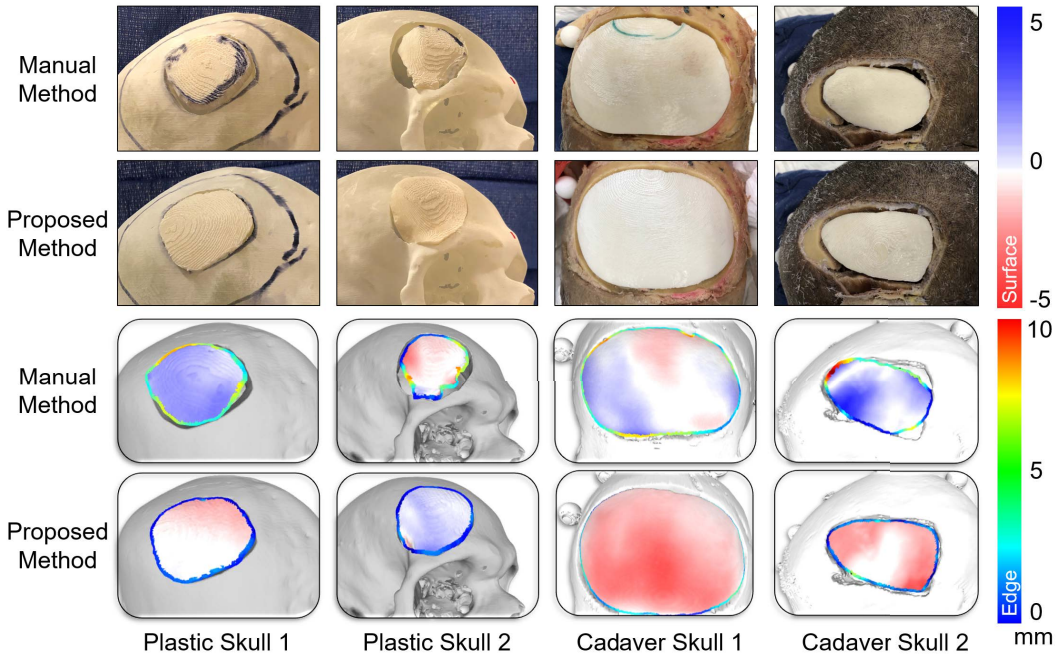

Figure 5.14: Resizing accuracy evaluation Oversized CCIs were resized by manual and by our proposed method to fit four cranial defects created on two plastic skulls and two cadaver heads. Top color bar represents the signed difference between the resized implant's top surface and its perfect skull. Bottom color bar represents the gap distance from the resized implant's edge to the defect skull.

compared to the previous hand-guiding approach. The time distribution in each step of our approach is listed in TABLE 5.1

Table 5.1: Time Distribution

Procedure	Minutes
3D Scanning	3-5
Patient-to-CT Registration	1-2
Toolpath Generation	2-3
Implant Localization	1-2
Resizing Implant	3-4

5.4.4 Resizing Accuracy

Oversized CCIs (6 *mm* in thickness) were 3D printed and resized by manual and by our automated approach to fit four cranial defects created on two plastic skulls and two cadaver heads. We evaluated the resizing accuracy by measuring the gap distance between the resized implant's edge and the skull defect's edge. The gap distance is defined by the per vertex euclidean distance in the "Distance from Reference Mesh" method in MeshLab[65]. In addition, the signed distance was computed for each resized implant by comparing its top surface to the 'perfect' skull. All the data were acquired by 3D scanning the physical resized implants fitted to their corresponding defects (Figure 5.14).

The mean gap distance and maximum gap distance were also evaluated, as shown in Figure 5.15, which showed that our proposed approach has improved the resizing accuracy by 60% on plastic skulls and by 30% on

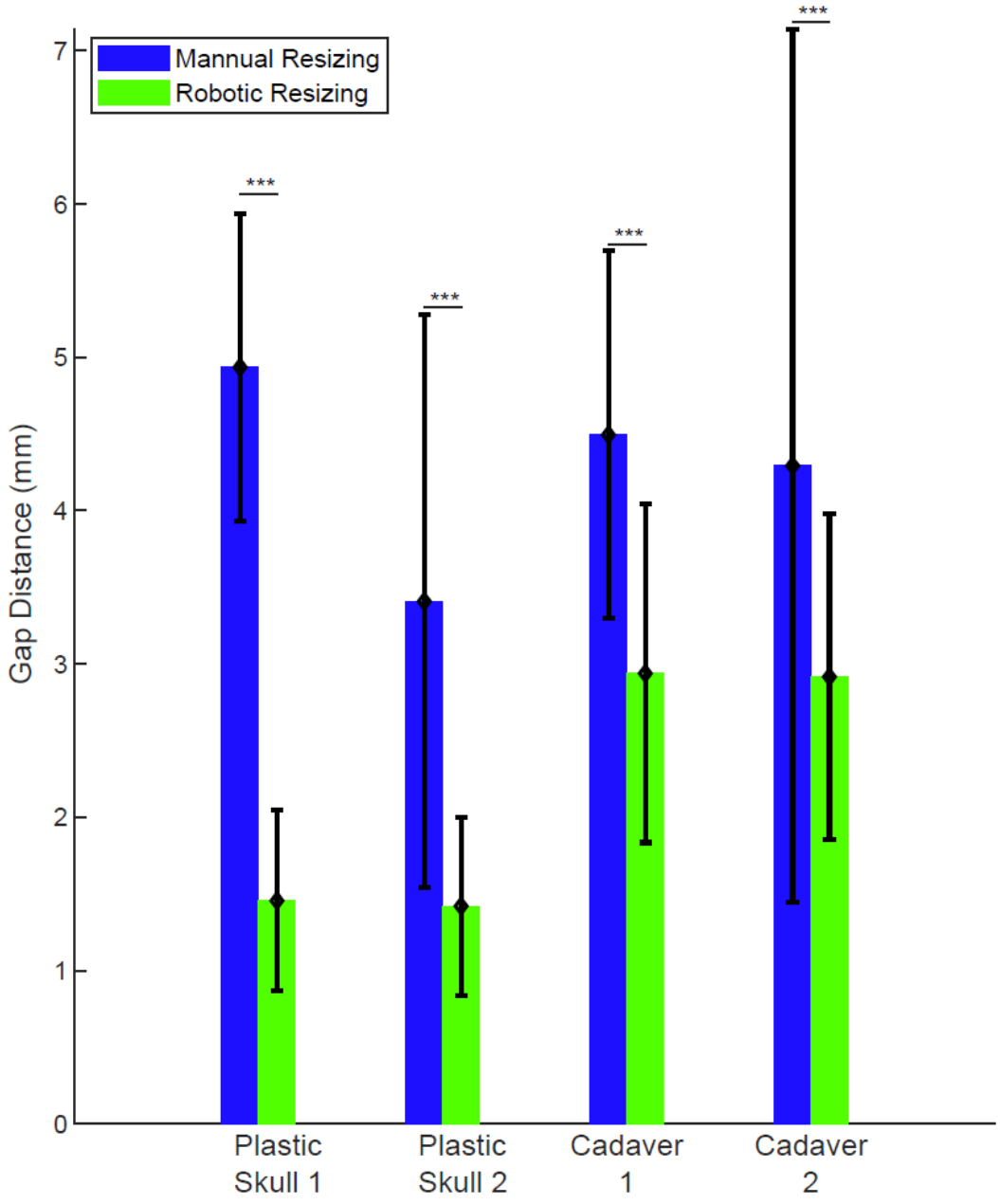

Figure 5.15: Mean gap distance Comparison of the resizing accuracy by manual and robotic method in terms of bone gap distance. The gap distance is calculated at each vertex. The graph shows mean value and $\pm$ std. p-value is calculated based on two-sample student's t-test: *** p<0.001

cadavers compared to the manual approach. Furthermore, this improved accuracy is consistent for two different defect locations, which represent distinct complexity of local craniomaxillofacial geometry. This demonstrates that our robotic cutting system can improve the resizing accuracy over the manual method on even a more complicated craniomaxillofacial geometry.

5.5 Summary

The robotic system developed in Chapter 4 provides an efficient CCI modification for single-stage cranioplasty. This Chapter further develops the system toward clinical applications.

Because of the draping requirement, the anatomical features are covered and can no longer provide correspondence for the patient-to-CT registration. To solve this issue, the author developed reattachable fiducial markers to provide additional registration points to accomplish this process.

Because of the complex skull geometry, an inappropriate cutting angle may result in the implant protruding above the patient's skull, which causes additional clinical complications. The complicated geometry of the skull must be accommodated by automatically adjusting the cutting angles so that the robot can always cut along the defect's wall. Therefore, the improved toolpath generation algorithm takes into account the defect's edge geometry, which allows the robot to resize CCIs closer to the 3D defect's shape. This improvement minimizes the possibility of implant protrusion.

The surgical workflow is further automated by automating the implant localization process. This improves the localization accuracy and saves time

compared to the passive hand-guiding method used in Chapter 4.

The proposed approach is compared to the conventional manual method for resizing accuracy using plastic skulls and cadavers. The results demonstrate that the proposed robotic system reduces the procedure time and minimizes the bone gaps between the resized implant and the skull defect.

In this work, however, the manually-tuned, experimentally-determined cutting speed and spinning rate of the tool were not optimized. Additional experiments are needed to evaluate the optimal cutting parameters for smooth cutting of the implant.

Chapter 6

A 5-Axis Laser Cutting System for Implant Modification

6.1 Motivation

The previous Chapter demonstrated an automated workflow for intraoperative CCI modification using a robotic system. The system utilizes the advanced 3D scanning technique as well as reattachable fiducial markers to accomplish the patient-to-CT registration. The robot localization of the implant is achieved automatically, which eventually allows the robot to resize the CCI using a mechanical cutter. The phantom and cadaver tests showed the proposed system's higher resizing accuracy compared to the conventional manual approach. This demonstrated the feasibility of the system toward clinical applications.

However, utilizing a mechanical cutter is limited by the robot's workspace, for the generated cutting locations and orientations may not be reachable by the robot. Therefore, the generated toolpath may need further adjustment, which, in turn, may reduce accuracy. In addition, mechanical cutting also

generates dust and rough edges, which may not be ideal in a sterile clinical environment.

In recent times, laser has been widely used in industries for cutting materials like steel, aluminum, wood, and various types of plastics [71–73]. Laser transmits highly-concentrated energy onto a small area of the workpiece material to melt and vaporize the focused region. This technique results in a much cleaner and streamlined cut compared to mechanical cutting. Laser cutting is frequently used for cutting acrylic sheets which are made of PMMA. A majority of commercial cranial implants are also made of PMMA. Therefore, this Chapter introduces the application of laser cutting for resizing CCIs.

This Chapter presents a five-axis laser cutting system for fast and precise CCI modification. The laser system consists of a three-axis linear stage, directing the laser beam, and a two-axis rotary table, mounting the implant. This compact design eliminates the workspace limitation that existed in the robotic cutting system and provides a cleaner, more accurate, and faster resizing.

6.2 Contribution

The author's contributions in this Chapter include:

- Developing a five-axis laser cutting system for intraoperative CCI modification.
- Calibrating the control system parameters, and derived the kinematics of the five-axis motion system.

- Testing the system on a phantom defect skull, and compared the results to the manual approach and the projector approach.

Mr. Jerry Fang helped the author in assembling the hardware. The work reported in this Chapter was published in the Proceedings of ASME International Design Engineering Technical Conferences and Computers and Information in Engineering Conference (2017) [74]. The author has filed a US patent for the system titled *"Cutting machine for resizing raw implants during surgery"*

6.3 Method

6.3.1 Design of Laser Cutting Machine

6.3.1.1 Design Considerations

A laser-based cutting system is considered superior than other methods (e.g. contact, stress, or pressure), since the entire surgical procedure is to be performed under a sterile environment. The system is designed to be compact so that the machine can be easily transported from one operating room to another. The size of the workspace for creating CCI profiles is greater than that of an average human skull. The laser power requirements for cutting through CCIs varies depending on the CCI thickness and material composition.

6.3.1.2 System Overview

The dimension of the laser cutting system is 1155 mm x 670 mm x 980 mm (length x width x height) as shown in Fig. 6.1. The system has the capability

of shaping the CCIs with five degrees of freedom. This allows the system to continuously trim the edges of the CCI with the desired angle at any location along the path. The machine comprises five units as shown in Fig. 6.2. Clockwise from the top, these units are: interface devices, accessories, mechanical hardware, electronic components, and laser components. Interface devices include PC, monitor, emergency stop button, and switches. Accessories include ventilation fans and water pump to cool the system, and an air pump to assist the laser in cutting CCIs. Mechanical hardware includes a Cartesian linear stage (LSR-KIT3020XY; LightObject, USA), customized rotary table, and aluminum steel machine frame (40-4040 LITE; 80/20 Inc. USA). Electronic components include NEMA series stepper motors (xy-axis: NEMA 17, z-axis: NEMA 34, rotary joints: NEMA 23; LightObject, USA), 5-axis breakout board, and motor driver boards. The laser components include a laser tube (SPT 35W CO2 Sealed; LightObject, USA), laser power supply (20W-45W PWM (AC 110V); LightObject, USA) and three reflecting mirrors (40W CO2 Laser Mirror/Lens; LightObject, USA).

6.3.1.3 Machine Configuration

The Cartesian linear stage provides 3 degrees-of-freedom (DOF) linear motion and the gimbal rotary table provides 2 DOF rotary motion. This 5 DOF system enables the laser to cut at a wider range of orientations and positions. Each motor is driven by a driver board, which in turn is controlled by a 5-axis breakout board. The placement of mirrors as shown in Fig. 6.3 allows the laser beam to be projected onto the rotary table.

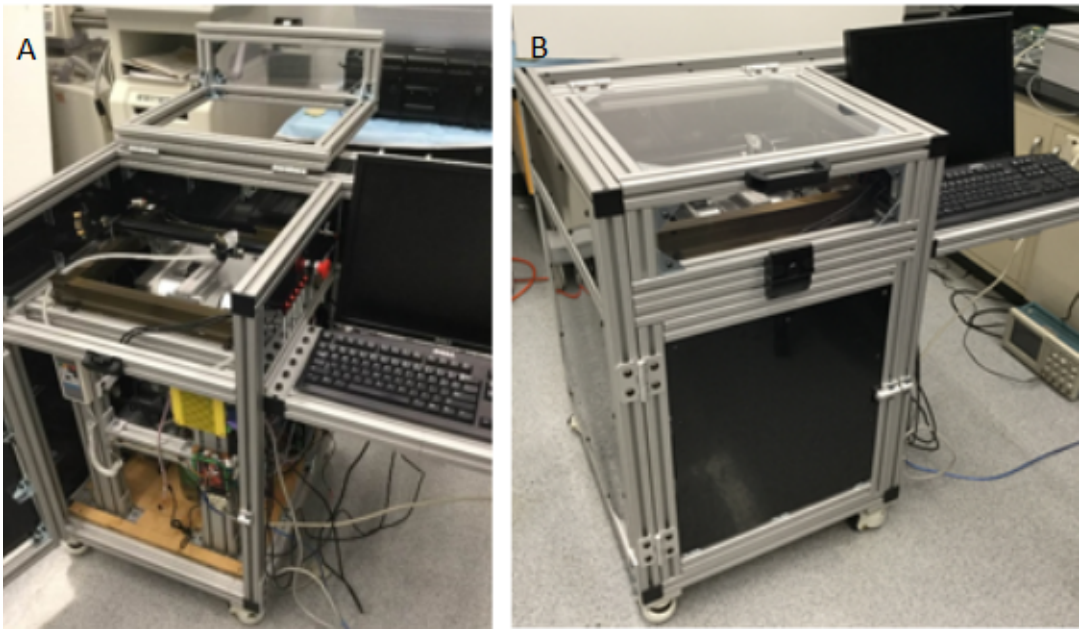

Figure 6.1: 5-axis laser cutting system A: inner view. B: outer view.

6.3.1.4 Laser Power

The 35W CO2 laser tube is powered by an AC 110V laser power supply. The output power can be controlled by either a TTL (20 kHz – 50 kHz, 5V PWM) or a 0–5V DC analog input. A water cooling system is built in to cool the laser tube. An air pump is installed for assisting the cutting process.

6.3.1.5 Cutter Location and Orientation

For this system, the cutter and its tip correspond to the laser beam and its focal point, respectively. Cutter location (CL) data extracted from 3D CAD models are used to generate a cutting path. CL data comprises two vectors: cutter tip position (Q) and cutter tip orientation (K). Both vectors are represented in

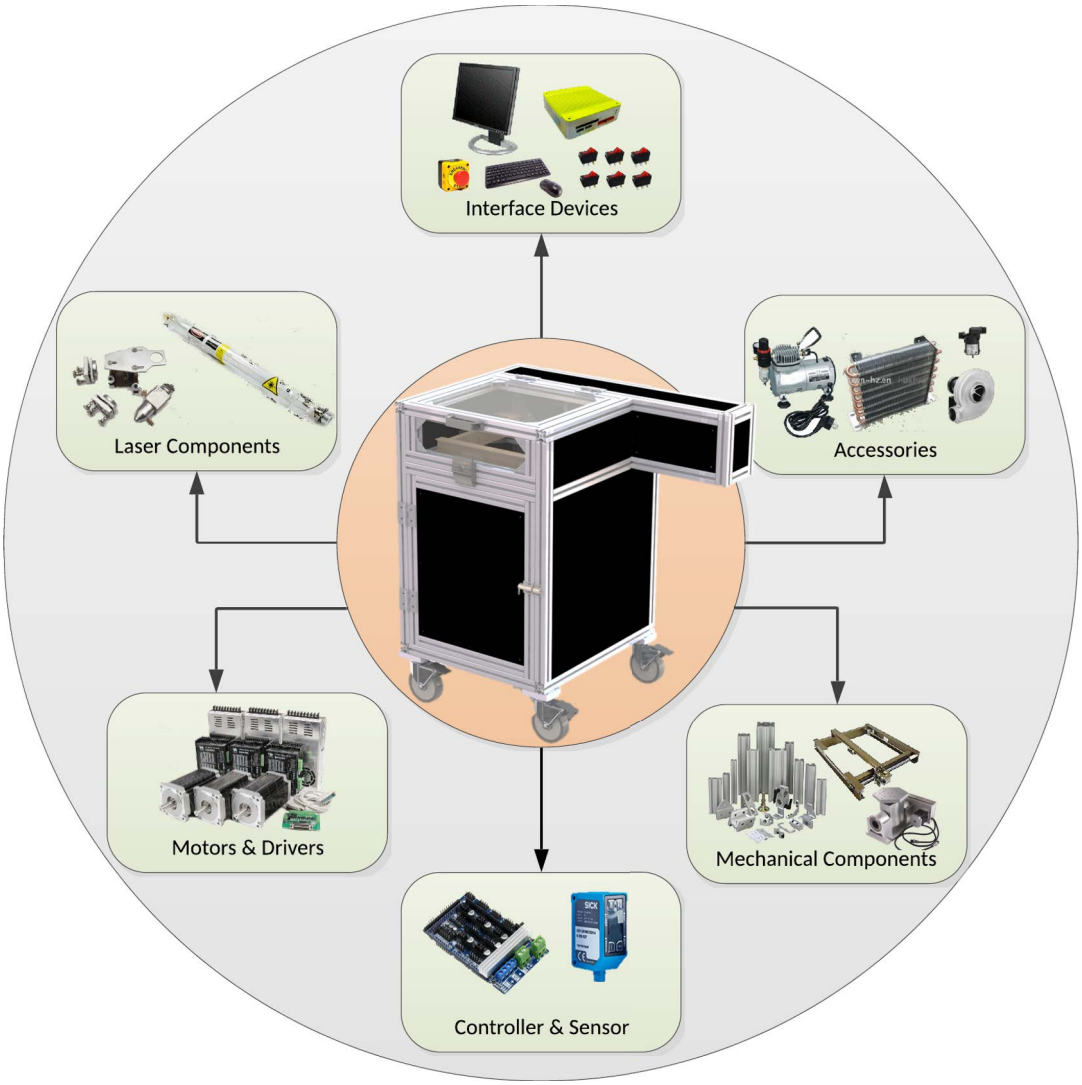

Figure 6.2: System components Laser system components/units.

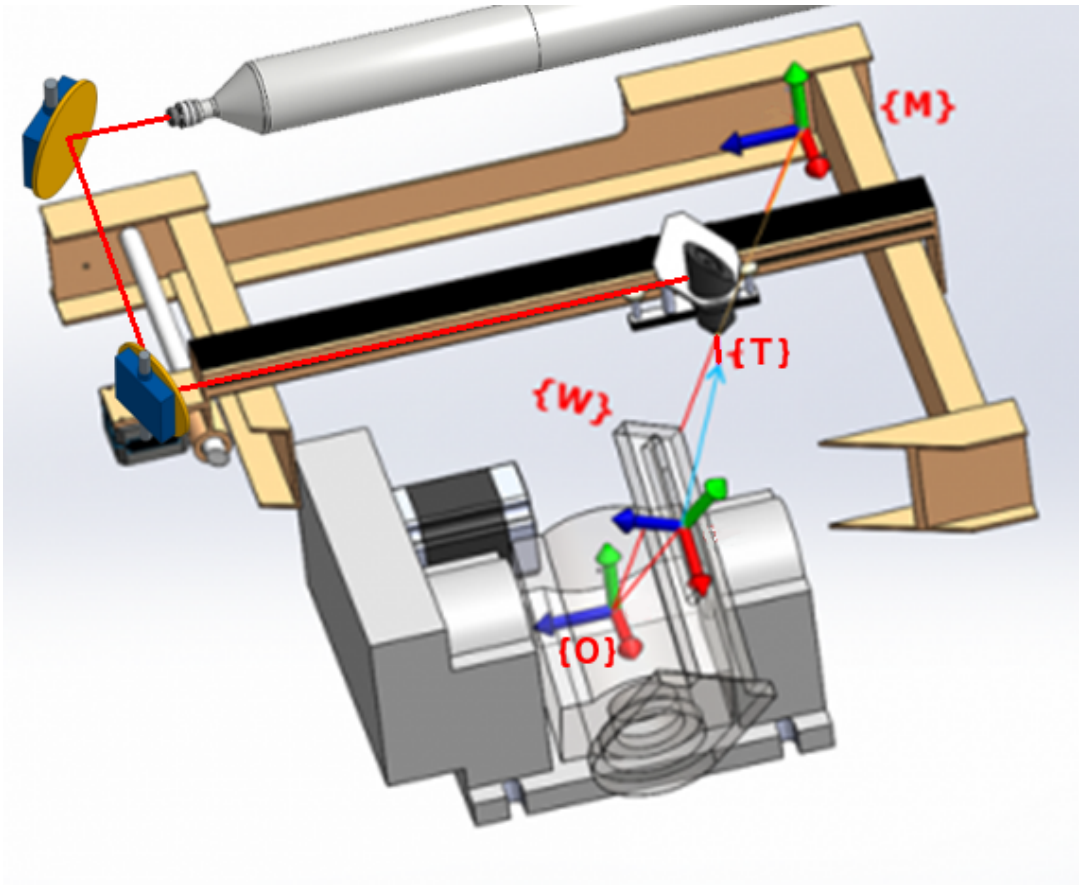

Figure 6.3: Coordinate systems The definition of coordinate systems. Laser projection onto rotary table using three mirrors. The coordinates frames are machine M, rotary table O, workpiece W, and laser head T.

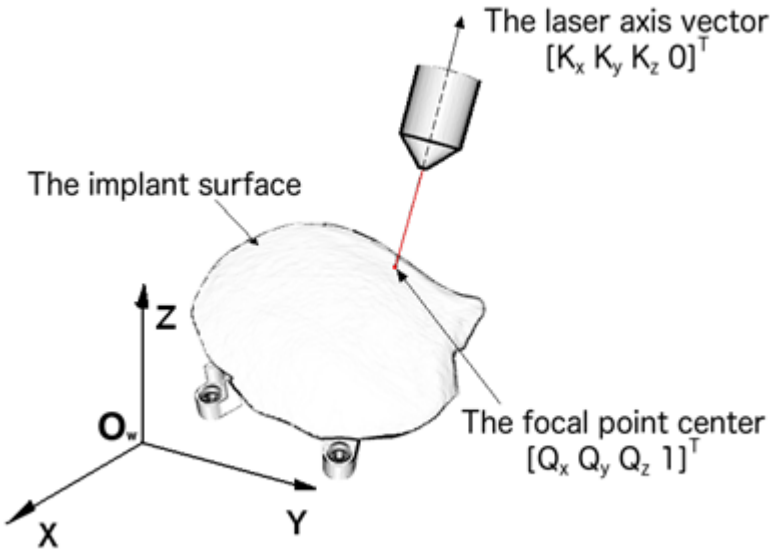

Figure 6.4: Cutter location and orientation in workpiece frame Vector Q describes the cutter tip position and vector K describes the cutter tip orientation.

the workpiece coordinate system as shown in Fig. 6.4. The generation of the cutting path is currently under development and will be addressed in detail in the future work.

6.3.1.6 Software Overview

LinuxCNC, open source software, controls the CNC laser cutting operation. The software reads the G-code and instructs the machine to move accordingly by sending control signals from a computer to the controller board in order to drive the motors. The kinematics model is also implemented in the LinuxCNC environment, and the calibrated parameters of the laser system are shown in Table 6.1.

Table 6.1: Calibrated parameters of the 5-axis motion system

Steps/Rev: number of stepper-motor-steps required to achieve one motor revolution.
Motor teeth & leadscrew teeth: reduction between motor and leadscrew.
Leadscrew pitch: amount of movement generated in one leadscrew turn.
Travel range: range of reachable space.

Parameter	D_1	D_2	D_3	θ_1	θ_2
Steps/Rev	200	200	200	200	200
Motor Teeth	1	1	1	1	1
Leadscrew Teeth	1	1	1	8	50.9
Leadscrew Pitch	20 mm	14.5 mm	5 mm	360 deg/rev	360 deg/rev
Current	2 A	2 A	3.5 A	2.8 A	2.8 A
Holding Torque	0.57 N·m	0.57 N·m	11.2 N·m	1.9 N·m	1.9 N·m
Travel Range	0 - 295 mm	0 - 255 mm	0 - 70 mm	-26 - 26 deg	-19 - 32 deg

6.3.2 Kinematics Analysis

There are four frames to consider: the machine frame {M}, rotary table frame {O}, the workpiece frame {W}, and the laser head frame {T} (Fig. 6.3). The origin of {O} is defined to be the point at which two rotary axes coincide, and the origin of {W} is at the surface of the implant mounting plate through which one of the rotary axes passes. The origin of {M} is at the home configuration of the system. The kinematics model in Fig. 6.5 illustrates the forward kinematics transformation from {W} to the laser focal point.

6.3.2.1 Forward Kinematics

Parameters for the variables that appear in this section are shown in Table 6.2 and are illustrated in Fig. 6.6. L_x, L_y, and L_z are the dimensions for the home offset of {M} with respect to {O}, D_1, D_2, and D_3 are the relative distances of the laser head (cutter) with respect to the home configuration of the system. L_f is the focal length of the laser head, and l is the length of the link from {W}

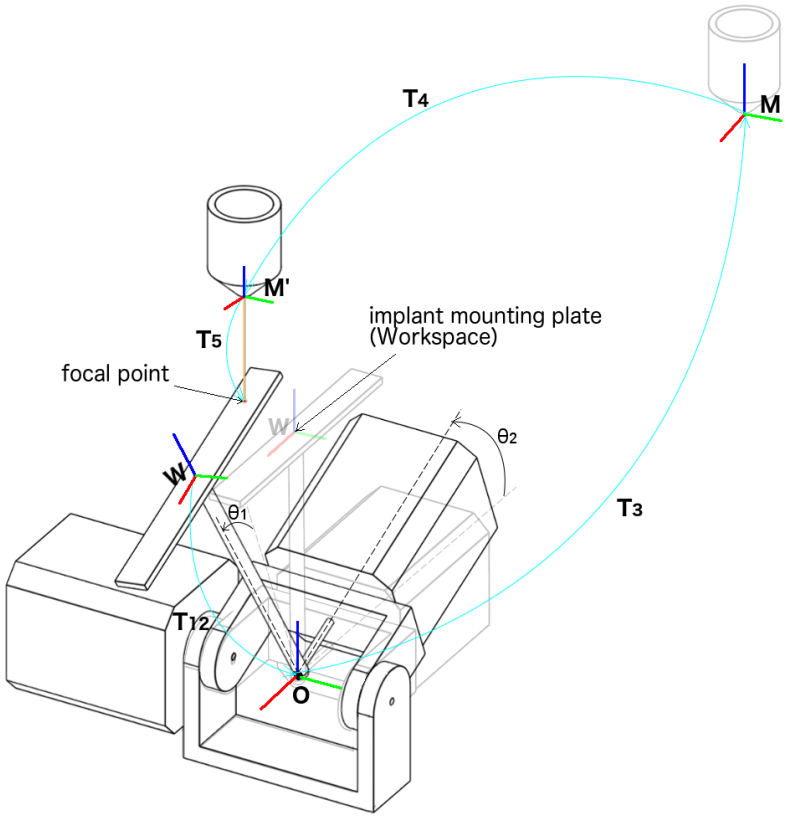

Figure 6.5: Kinematics model The diagram shows the system aligns the laser beam and its focal point to a given cutter location by moving the rotary table and the linear stage.

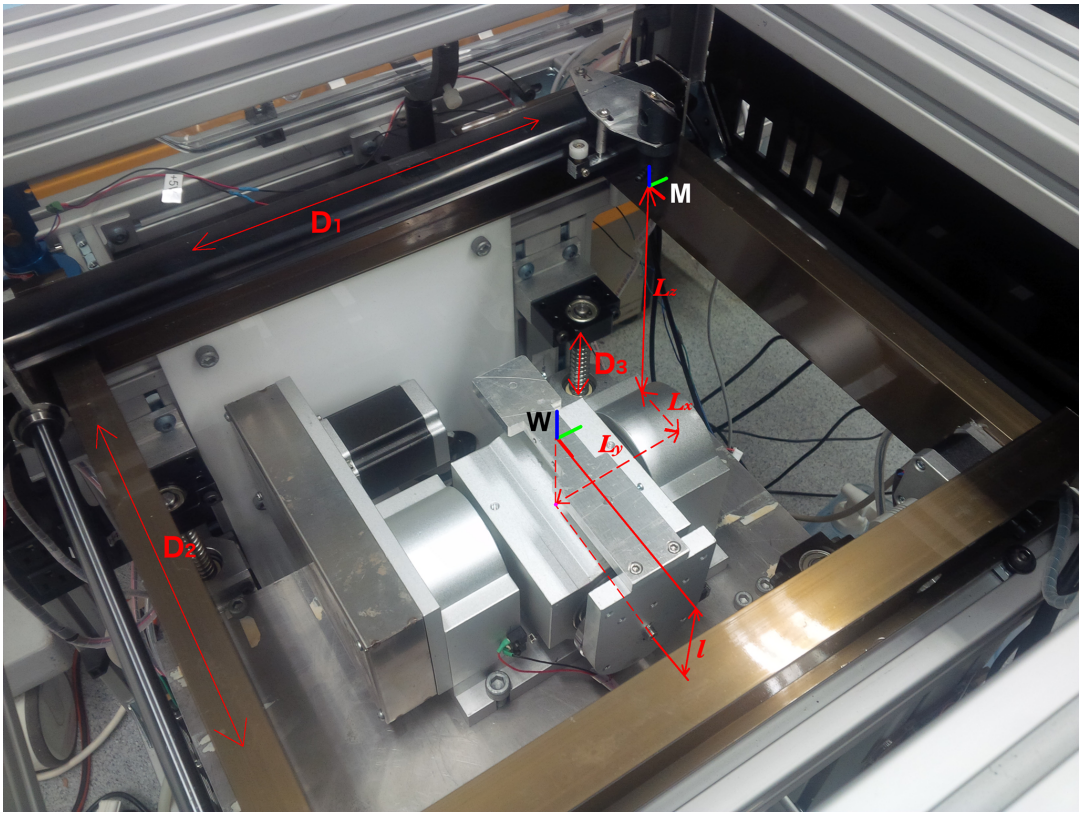

Figure 6.6: Robot links and joints Variable definitions to accompany Table 6.2

to {O}.

The transformation from {W} to {O} comprises two transformations (Eqn. 6.1 and 6.2) due to the two rotating axes intersecting at a pivot point. This point has an intermediate frame {O'} that is coincident with {O}. Note that θ_1 and θ_2 correspond to each of the two angles on the rotary table, and c and s denote *cos* and *sin*, respectively. The rotational components in Eqn. 6.1 and 6.2 differ from those of conventional rotation matrices because the rotary table moves

Table 6.2: Physical parameters of the system.

Variable	Value	Variable	Value
L_x	136.6 mm	L_f	34 mm
L_y	88.7 mm	l	77.8 mm
L_z	155 mm	-	-

in an opposite direction, and therefore negative angles, relative to {W}.

$$ {}^{W}A_{O'} = \begin{bmatrix} 1 & 0 & 0 & 0 \\ 0 & c\theta_1 & s\theta_1 & 0 \\ 0 & -s\theta_1 & c\theta_1 & -l \\ 0 & 0 & 0 & 1 \end{bmatrix} \tag{6.1} $$

$$ {}^{O'}A_{O} = \begin{bmatrix} c\theta_2 & 0 & -s\theta_2 & 0 \\ 0 & 1 & 0 & 0 \\ s\theta_2 & 0 & c\theta_2 & 0 \\ 0 & 0 & 0 & 1 \end{bmatrix} \tag{6.2} $$

Equations 6.3 describe the transformation from {O} to {M}, {M} to {T}, and {T} to the implant surface, respectively. All three transformations involve only the translational component, as the orientation of the axis remains the same. ${}^{T}A_{f}$ describes the offset of the cutter tip that is equal to the focal length of the

laser beam, L_f.

$$
{}^{O}A_f = {}^{O}A_M * {}^{M}A_T * {}^{T}A_f = \begin{bmatrix} 1 & 0 & 0 & D_2 - L_x \\ 0 & 1 & 0 & -D_1 + L_y \\ 0 & 0 & 1 & D_3 + L_z - L_f \\ 0 & 0 & 0 & 1 \end{bmatrix} \tag{6.3}
$$

The product of all the transformations (${}^{W}A_{O'} * {}^{O'}A_O * {}^{O}A_f$) results in the complete forward kinematics of the system, ${}^{W}A_t$, as shown in Eqn. 6.4.

$$
{}^{W}A_f = \begin{bmatrix} c\theta_2 & 0 & -s\theta_2 & P_x \\ s\theta_1 s\theta 2 & c\theta_1 & s\theta_1 c\theta_2 & P_y \\ c\theta_1 s\theta_2 & -s\theta_1 & c\theta_1 c\theta_2 & P_z \\ 0 & 0 & 0 & 1 \end{bmatrix} \tag{6.4}
$$

The forward transformation of the kinematics can be written as followed.

$$
\begin{aligned}
Q &= \begin{bmatrix} P_x & P_y & P_z & 1 \end{bmatrix}^T \\
&= \begin{bmatrix} (D_2 - L_x)c\theta_2 - (D_3 + L_z - L_f)s\theta_2 \\ -(D_1 - L_y)c\theta_1 + (D_2 - L_x)s\theta_1 s\theta_2 + (D_3 + L_z - L_f)s\theta_1 c\theta_2 \\ (D_1 - L_y)s\theta_1 + (D_2 - L_x)c\theta_1 s\theta_2 + (D_3 + L_z - L_f)c\theta_1 c\theta_2 - l \\ 1 \end{bmatrix}
\end{aligned} \tag{6.5}
$$

6.3.2.2 Inverse Kinematics

The solution set $[\theta_1, \theta_2, D_1, D_2, D_3]$, represented in {M}, can be computed at a position along the implant contour. These solution sets would inputted into LinuxCNC to command the system in shaping CCI profiles.

The laser beam is always along the z-axis. The third column of Eqn. 6.4, therefore, computes the cutter orientation vector, K, which is used to compute

the Euler angles for the rotary table.

$$K = \begin{bmatrix} K_x \\ K_y \\ K_z \\ 0 \end{bmatrix} = \begin{bmatrix} -s\theta_2 \\ s\theta_1 c\theta_2 \\ c\theta_1 c\theta_2 \\ 0 \end{bmatrix} \tag{6.6}$$

θ_1 and θ_2 can be calculated from Eqn. 6.6 as follows.

$$\begin{cases} \theta_1 = \tan^{-1}(\dfrac{K_y}{K_z}) & (6.7) \\ \theta_2 = \sin^{-1}(-K_x) & (6.8) \end{cases}$$

Equation 6.5 can be rewritten as:

$$Q = \underbrace{\begin{bmatrix} 0 & c\theta_2 & -s\theta_2 & 0 \\ -c\theta_1 & s\theta_1 s\theta_2 & s\theta_1 c\theta_2 & 0 \\ s\theta_1 & c\theta_1 s\theta_2 & c\theta_1 c\theta_2 & -l \\ 0 & 0 & 0 & 1 \end{bmatrix}}_{H} \underbrace{\begin{bmatrix} D_1 - L_y \\ D_2 - L_x \\ D_3 + L_z - L_f \\ 1 \end{bmatrix}}_{X} \tag{6.9}$$

The solutions for D_1, D_2, and D_3 are computed by solving for X in Eqn. 6.9 with $X = H^{-1}Q$, where H is a homogeneous transformation. D_1, D_2, and D_3 can also be derived analytically:

$$\begin{bmatrix} D_1 \\ D_2 \\ D_3 \\ 1 \end{bmatrix} = \begin{bmatrix} 0 & -c\theta_1 & s\theta_1 & ls\theta_1 \\ c\theta_2 & s\theta_1 s\theta_2 & c\theta_1 s\theta_2 & lc\theta_1 s\theta_2 \\ -s\theta_2 & s\theta_1 c\theta_2 & c\theta_1 c\theta_2 & lc\theta_1 c\theta_2 \\ 0 & 0 & 0 & 1 \end{bmatrix} \begin{bmatrix} Q_x \\ Q_y \\ Q_z \\ 1 \end{bmatrix} + \begin{bmatrix} L_y \\ L_x \\ L_f - L_z \\ 0 \end{bmatrix} \tag{6.10}$$

Equations 6.7, 6.8, and 6.10 can be used to find the inverse solution

$[\theta_1, \theta_2, D_1, D_2, D_3]^{\mathrm{T}}$. If the joint limits are not violated, the machine drives the laser head to a given desired cutting location provided by the CL data.

6.4 Results

The contour path of the oversized implant is shown in Fig. 6.7. We used this contour path as baseline control. This implant model and the corresponding defect were designed in SolidWorks. We converted the implant contour point coordinates to G code. The oversized implant profile was created with a 3D printer. Three methods for reshaping implants were compared: 1) the application of laser cutting system; 2) manual reshaping using computer-assisted projection [43] (Fig. 6.7 b); and 3) manual reshaping without the computer-assisted projection. Both types of manual involve tracing the contour onto 3D printed implants and cutting along the path with a Dremel drill. Figure 6.8 illustrates the comparison between modified implant profiles and the control profile. The image overlay and distance measurement were performed using Gimp. The results, which were approximated distance values measured in the images, are shown in Table 6.3. In summary, the implant modified by the laser system has a relatively smaller bone gap of 0 $\sim$ 0.6 mm. Although there is 0 $\sim$ 1.2 mm collision overshoot, it can be manually eliminated using a Dremel drill.

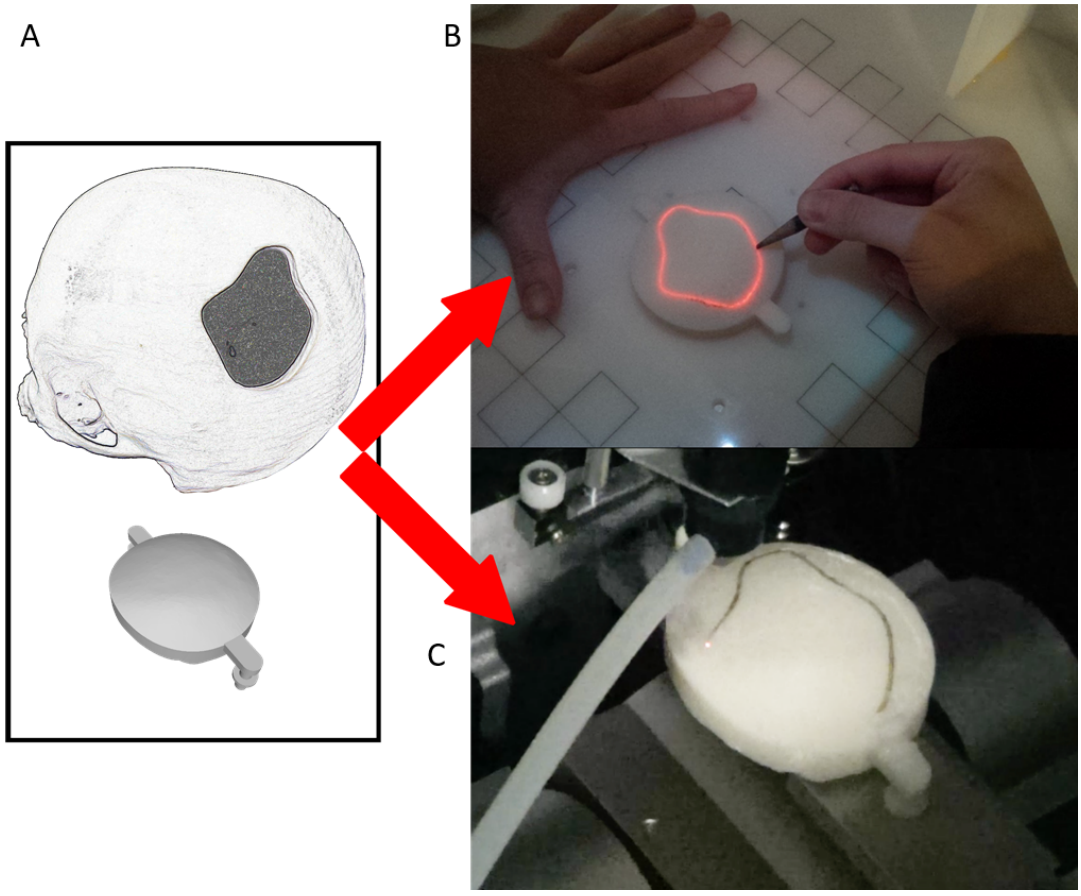

Figure 6.7: Experiment setup A: Experimental cranial defect model and its oversized implant profile. B: modification by the projection method. C: modification by the laser system.

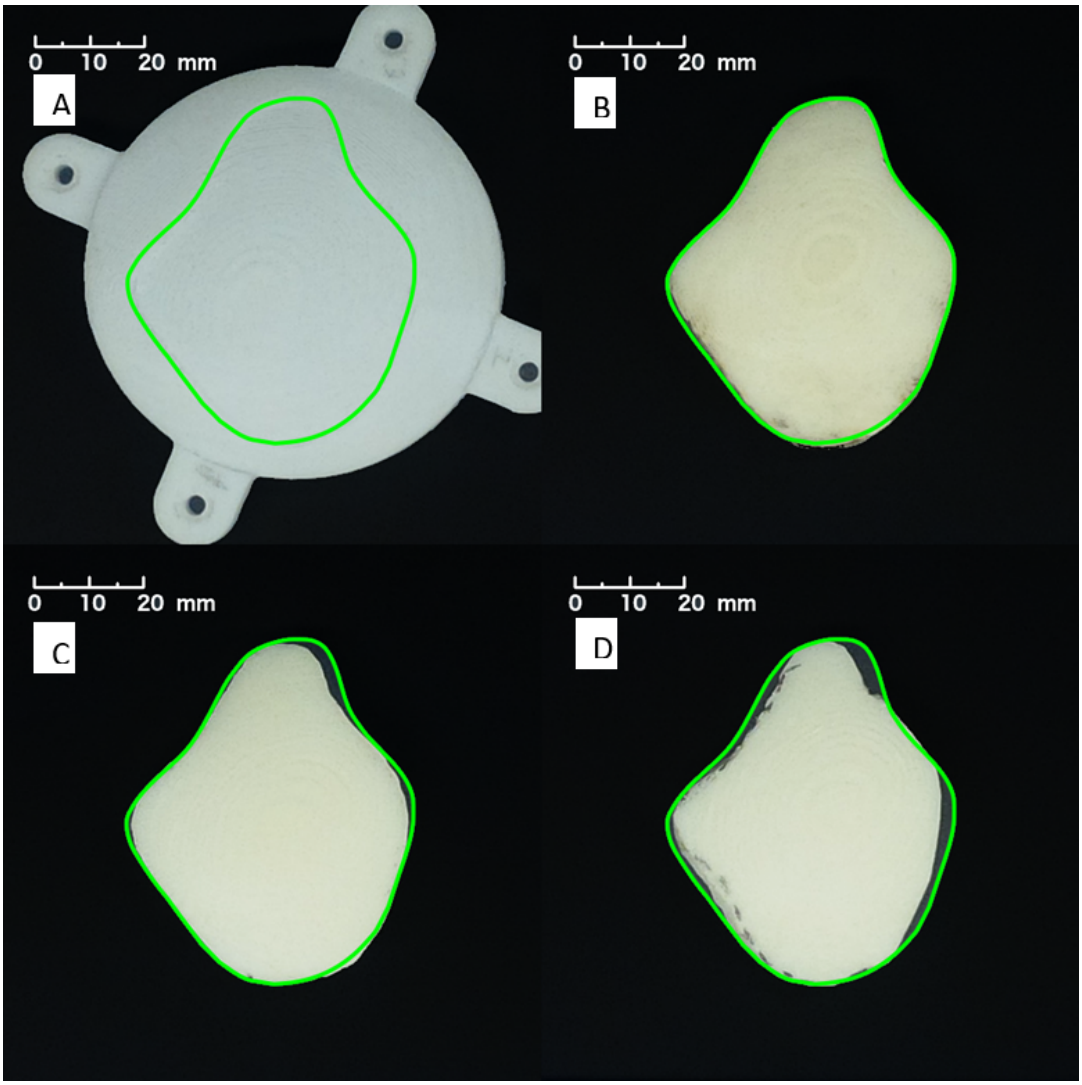

Figure 6.8: Evaluation of the cutoff implants A: printed oversized implant profile with defect contour. B: implant modified by the laser system. C: implant modified manually with computer-assisted projection. D: implant modified manually by visual judgement.

Table 6.3: Distance measurements of different cutting methods

Method	Max Collision Overshoot	Max Gap Distance
Laser System	1.2 mm	0.6 mm
Manual (visual)	-	3.0 mm
Manual (projection)	-	2.5 mm

6.5 Summary and Discussion

Mechanical cutting usually generates a large amount of dust, which is not ideal in the sterile surgical environment. Moreover, an implant resized from the mechanical cutting usually has rough edges, which compromises its fitting accuracy. Even though the robotic cutting system mentioned in the previous two Chapters improve the resizing accuracy over the manual approaches, the confined workspace restricts the robot from reaching certain tool orientations.

This Chapter introduces a cranial implant laser cutting system for single-stage cranioplasty. The system features automatic, five-axis laser cutting capability enabling three-dimensional cutting, which is essential in achieving smoother cutting edges when repairing complex cranial deformities.

The preliminary study on a simple defect geometry presented in this Chapter shows a higher implant resizing accuracy compared to the parallel manual modification approach. Because of the geometric simplicity of the skull defect, only 3-axis kinematics was applied in this study. For more complex defect geometry, the full 5-axis kinematics, which considers the defects' wall angle, should be utilized as discussed in the next Chapter. In addition, thicker implant might need higher laser power to achieve one-time

cut.

The proposed five-axis laser cutting system can potentially change the paradigm for performing cranioplasty procedures. The technology can help surgeons achieve optimal implant modification and, subsequently, improved surgical outcomes.

Chapter 7

Applications and Improvements of the 5-Axis Laser

7.1 Motivation

The previous Chapter introduced a 5-axis laser cutting system for CCIs resizing and described the basics for the 5-axis kinematics. Testing on a simple skull defect, which only involves 3-axis cutting, demonstrated its higher resizing accuracy than the manual approach.

In this Chapter, the author addresses some major improvements over the latest laser cutting system. First, the author implements the control of the 2-axis rotary table described in the previous Chapter, which allows a more accurate cutting angle. Second, the existing implant fixture platform, mounted on the rotary table, requires customized tabs, which usually do not come with the commercially purchased CCIs. This Chapter presents a universal implant fixture platform by using a clamp. The system also includes a foldable marker ring around the implant fixture platform as a correspondence to transform the cutting toolpath from CT space to the laser space. A hand-held

3D laser scanner matches the implant from the laser space to the CT space via correspondence from the marker ring. This allows the generated cutting toolpath to be transformed to the laser space. Third, the system uses a 100 W laser as opposed to the 35 W laser used in Chapter 6, which grantees a one-time cut.

Because of the high resizing accuracy, the titanium plates or strips, commonly used for cranial implant fixation [75, 76], are not necessary for the laser-resized CCI. Therefore, one of the important applications of the laser system in the neuroplastic field is non-screw fixation. In addition, taking advantage of the more accurate, cleaner, and faster cutting by the laser, several other neuroplastic applications are made possible. Specifically, this Chapter introduces laser milling, which can be used to fabricate instrumented implants for targeted drug delivery, deep-brain stimulation, and shunt placement.

7.2 Contribution

The author's contributions in this Chapter include:

- Further developing the five-axis laser cutting system for intraoperative CCI modification.
- Upgrading several major components of the system, and improved the five-axis toolpath algorithm.
- Proposing an implant localization method using an RGB camera or a 3D scanner with a foldable marker ring.

- Testing the system's five-axis cutting performance on a phantom defect skull, and compared the results to the manual approach.
- Presenting the non-screw fixation, and the potential of laser milling in fabricating instrumented implants.

Mr. Wei-Lun Huang helped the author in improving the five-axis toolpath generation algorithm. The work reported in this Chapter has not yet been published.

7.3 Method

7.3.1 Surgical Workflow

The overall workflow for CCIs resizing using the laser system, as shown in Figure 7.1, is generally the same as the workflow proposed in Chapter 5 using the robotic system. They shared the same process of patient-to-CT registration as described in Chapter 5: the 2-scan method using a hand-held 3D scanner prior to draping and reattachable fiducial markers for registration when draping is applied. However, since the laser only has 5-Degree of Freedom (DoF) compared to KUKA robot's 7-DoF, the toolpath generation algorithm needs to be modified. To facilitate the registration between the CT, where the toolpath is generated, and the laser space, where the physical implant is placed, a foldable marker ring is utilized. The marker ring provides correspondences for CT-to-laser registration while the handheld 3D scanner captures the implant geometry.

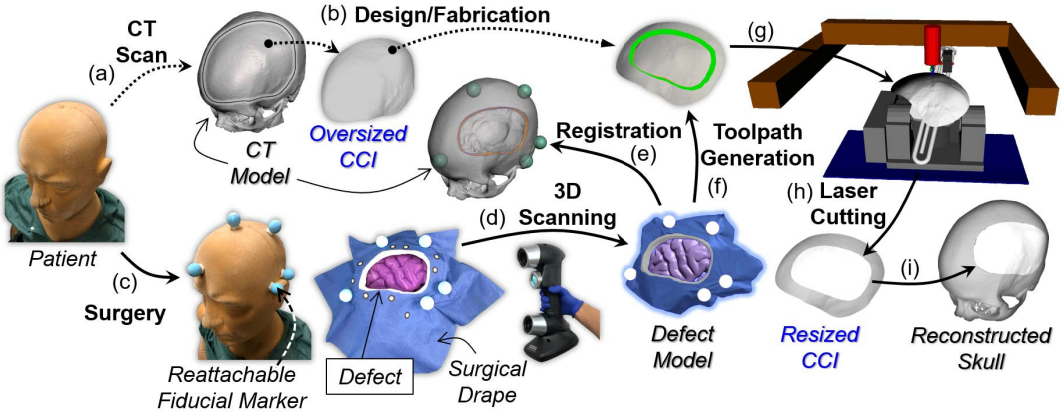

Figure 7.1: The CCI resizing workflow using 5-axis laser system (a) The patient takes a preoperative CT scan. (b) A patient-specific oversized CCI is designed and fabricated based on the CT model. (c) The patient undergoes neuroplastic surgery. (d) The cranial defect geometry is captured using a handheld 3D scanner. (e) The patient-to-CT registration is accomplished via reattachable fiducial markers. (f) A 5-axis toolpath algorithm generates the cutting toolpath. (g) The laser system localizes the implant. (h) The laser system cuts the implant. (i) The resized implant is attached to the skull.

7.3.2 System Overview

The previous Chapter uses a 35 W laser and only implements 3-axis control for cutting. In this Chapter, the author implements all 5-axis kinematics to the system, and upgrades to a 100 W CO_2 laser. To eliminate the customization of adding tabs to the implant, a new implant fixture clamp is installed on the rotary table. For the laser system to localize the implant, two approaches are utilized. The first approach uses an RGB camera to locate the implant by detecting the markers on the implant, which requires additional customization from the implant manufacturer. The second approach relies on a foldable marker ring to provide corresponding registration points for CT-to-laser registration. A handheld 3D laser scanner was used to acquire the implant and

marker ring information for the registration. The marker ring is attached to a 1/4 inch camera mount on the laser system and is unfolded during the registration process through the 3D laser scanner. It will then be folded during the cutting. The XY coordinates of the registration points in the laser space is recorded by the linear stage. A SICK distance sensor (Od1-B035) is attached next to the laser nuzzle to measure the registration points' Z coordinates (Figure 7.2).

7.3.3 Controller Structure

We upgraded to a 5-Axis GRBL controller for the five closed-loop stepper motors and a 100 W laser simultaneously. The author developed a Rviz GUI to communicate with the controller. For implant registration using an RGB camera, the interface simply controls the GRBL controller for laser cutting. For implant registration using the foldable marker ring, a LabJack U3 data acquisition device is added for coordinate recording. Before cutting, the user jogs the distance sensor, through the GRBL controller, to each registration point to record their coordinates in the laser space via LabJack U3. After all registration points' coordinates are recorded, the distance sensor is detached. The interfaces then utilizes GRBL controller to cut the implant based on the generated toolpath (Figure 7.3).

7.3.4 Implant Localization and Registration

Two methods of implant localization are utilized in this Chapter. The first approach uses an RGB camera to detect predefined markers on an implant.

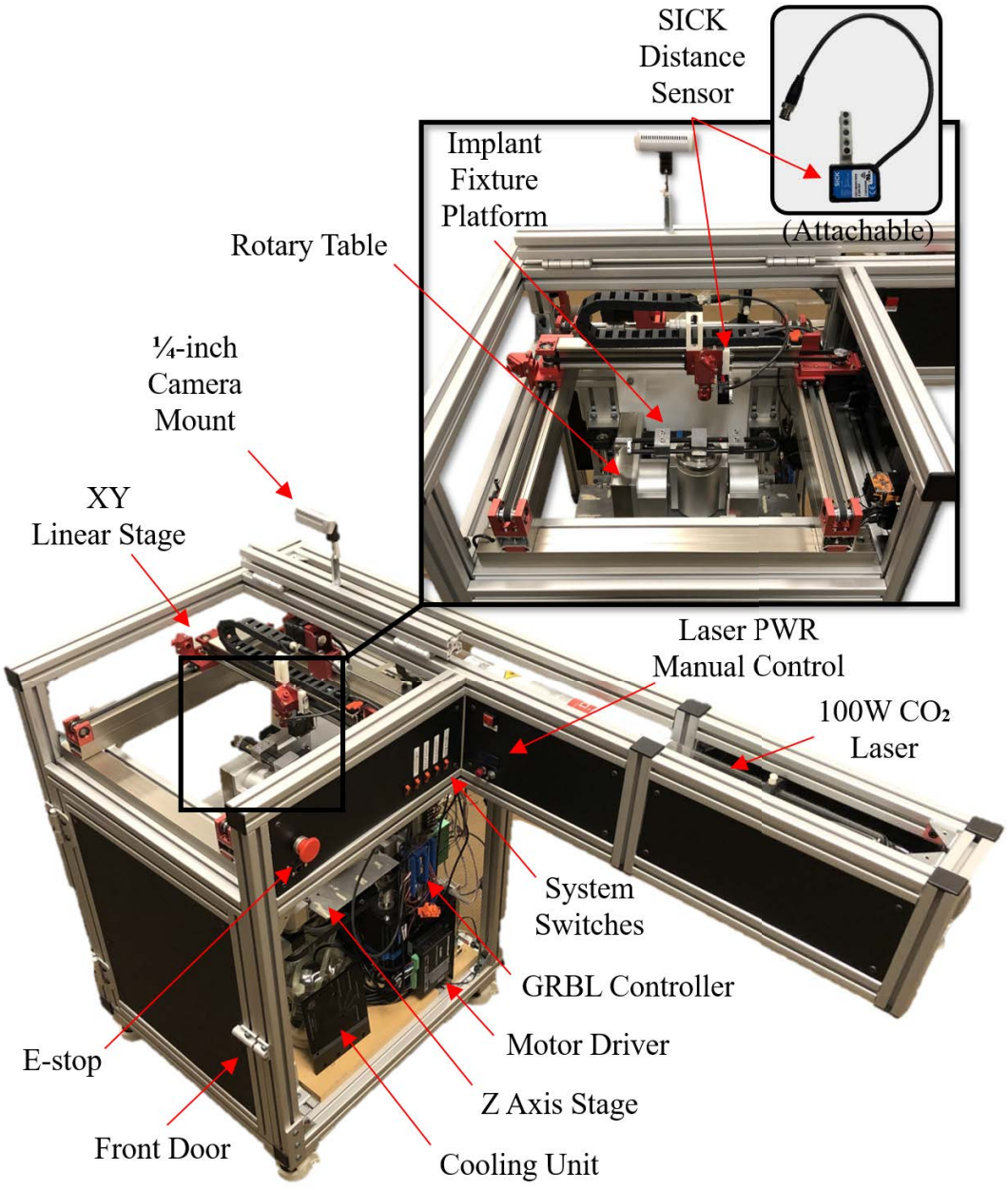

Figure 7.2: System overview The upgraded 5-axis laser system with a universal implant fixture platform, a 100W CO_2 laser, a GRBL controller, and a SICK distance sensor.

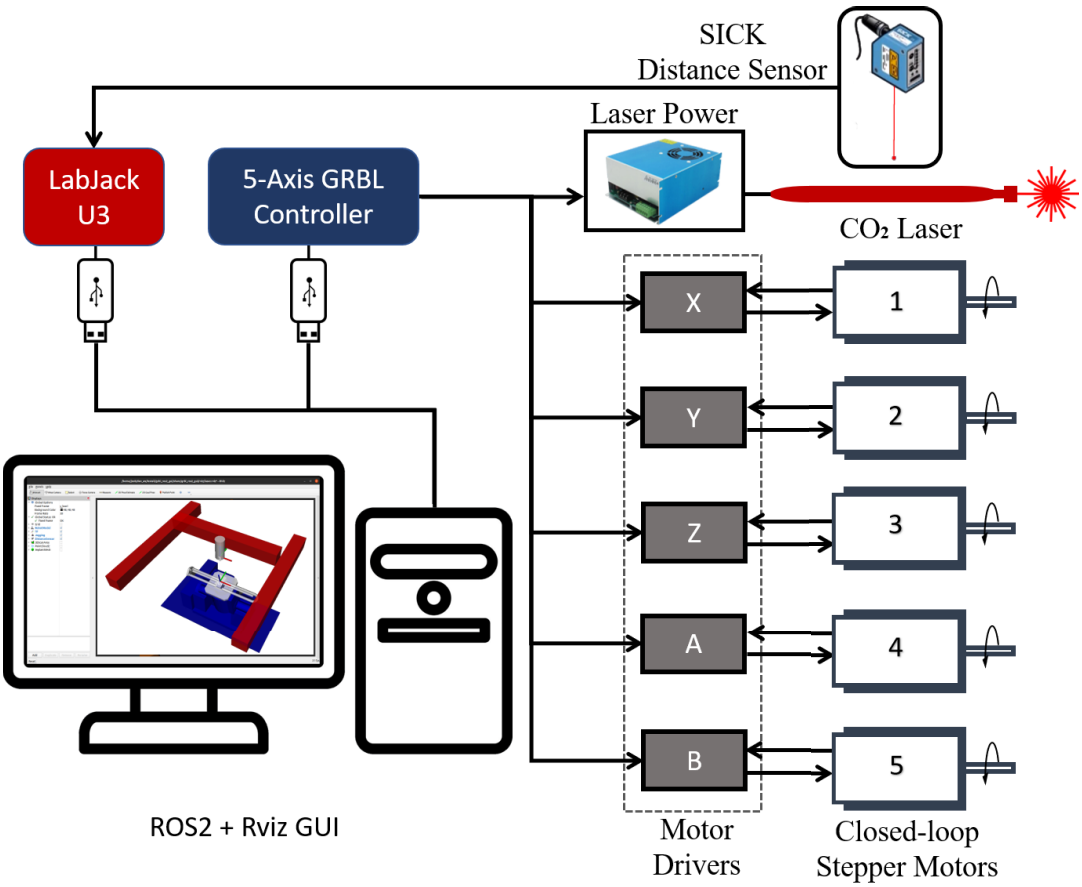

Figure 7.3: System controller diagram A ROS2/Rviz2 GUI communicates with the 5-axis motion system and the laser via a GRBL controller, and with the SICK distance sensor via a LabJack U3.

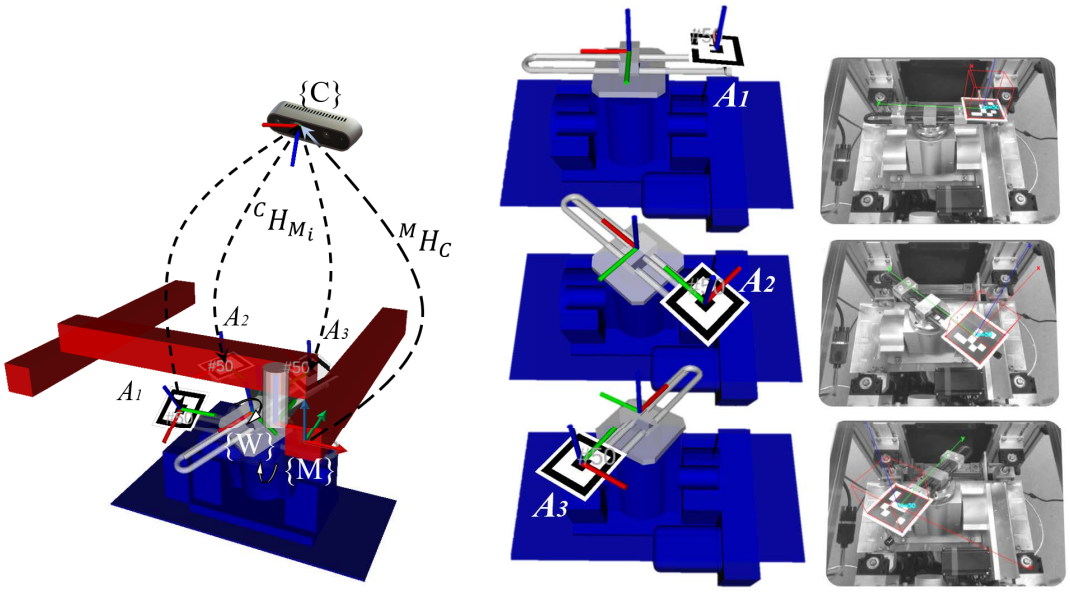

Figure 7.4: Hand-eye calibration The hand-eye calibration finds the transformation of the camera frame {**C**} from the machine frame {**M**}, $^{M}H_{C}$. During this process, the system commands the rotary table to move to different poses while the RGB camera captures and estimates the pose of the ArUco marker attached on the rotary platform.

The second approach utilizes a 3D handheld laser scanner to detect markers on a foldable marker ring around the implant.

7.3.4.1 Using an RGB Camera

The first step is to perform a one-time hand-eye calibration, using an aruco marker. The aruco marker is attached to the rotary table, and is moved to a number of different poses. The camera captures the aruco marker at each pose for calculating $^{M}H_{C}$, the relative pose of the camera {**C**}, to the machine frame {**M**} (Figure 7.4). The calculation is similar to that from Chapter 5.

Once the hand-eye calibration is completed, the RGB camera is ready for localizing implants with predefined marker points. The camera captures the implant at two different angles by rotating the rotary table. The difference

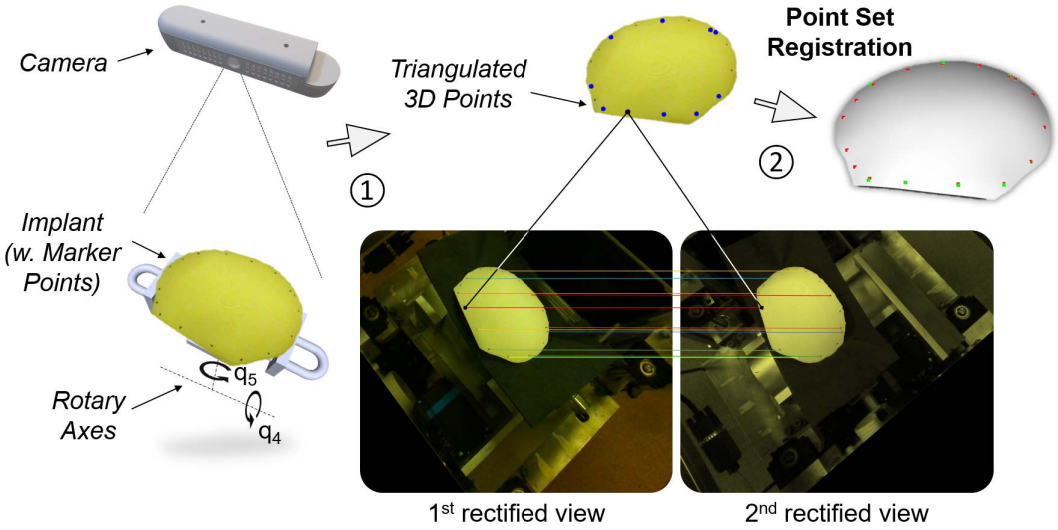

Figure 7.5: Implant registration using a RGB camera Marker points on the implant are detected and triangulated to find its 3D coordinates in the camera space. Afterwards, the implant is registered to the machine via point set registration.

between the two camera poses can be retrieved from the robot's kinematics. The two images are then rectified. The detected marker points can be triangulated to find their 3D coordinates in the camera space. Applying point set registration on the detected marker points finds the location of the implant in the machine space based on ${}^{M}H_{C}$ (Figure 7.5).

7.3.4.2 Using a 3D Scanner

Another approach for registering the implant to the laser system is to use foldable marker ring and a high-resolution 3D laser scanner (Figure 7.6). The marker ring has four registration points and several markers. First, the coordinates for each registration point is measured and recorded, as mentioned in Section 7.3.3. Registration begins with capturing the geometries of the implant and the marker ring using a handheld 3D laser scanner. The 3D scanned

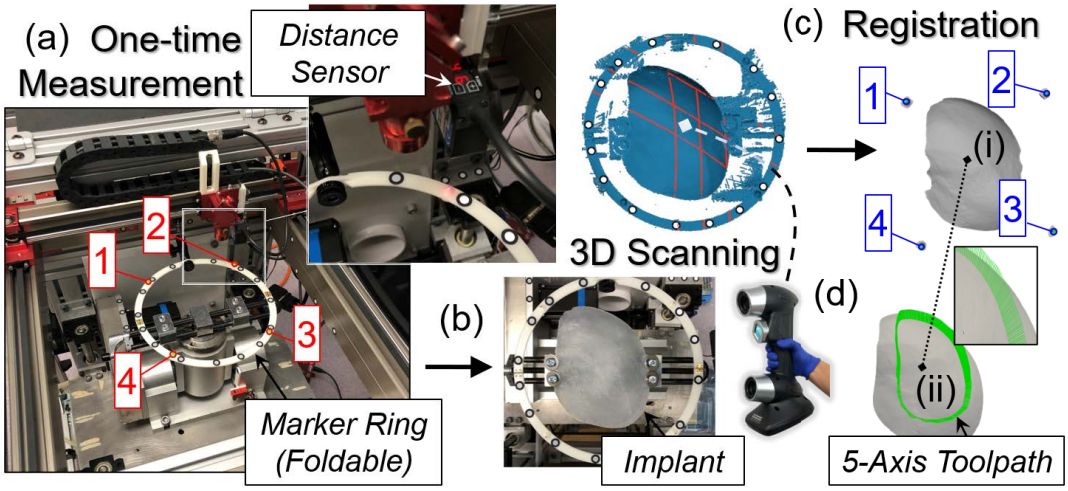

Figure 7.6: Implant registration using a 3D scanner (a) Performing an one-time measurement using the distance sensor to record the coordinates of the four registration points on the marker ring. (b) After mounting the implant on the rotary's fixture platform, a handheld 3D scanner is used to generate a 3D mesh of the implant including the surrounding marker ring. (c) The 3D scanned mesh can be registered to the machine coordinates system using the four correspondent registration points. (d) The generated 5-axis toolpath can be transformed to the laser space after registering the CT implant model to the 3D scanned implant model via ICP.

implant model and the four registration points are then segmented. Using point set registration by these four correspondence points, the laser system localizes the 3D scanned implant. The registration to the 3D scanned model is completed by running ICP.

7.3.5 Toolpath Generation

The laser system includes four coordinate frames, as shown in Figure 7.7. The frames are defined as: 1) the global coordinate system defined in machine space, or, machine frame {**M**}; 2) the coordinate system defined at laser nuzzle, or, tool frame, {**T**}; 3) coordinate system defined at the implant mounting platform, or, workpiece frame, {**W**}; 4) coordinate system defined at the coincident

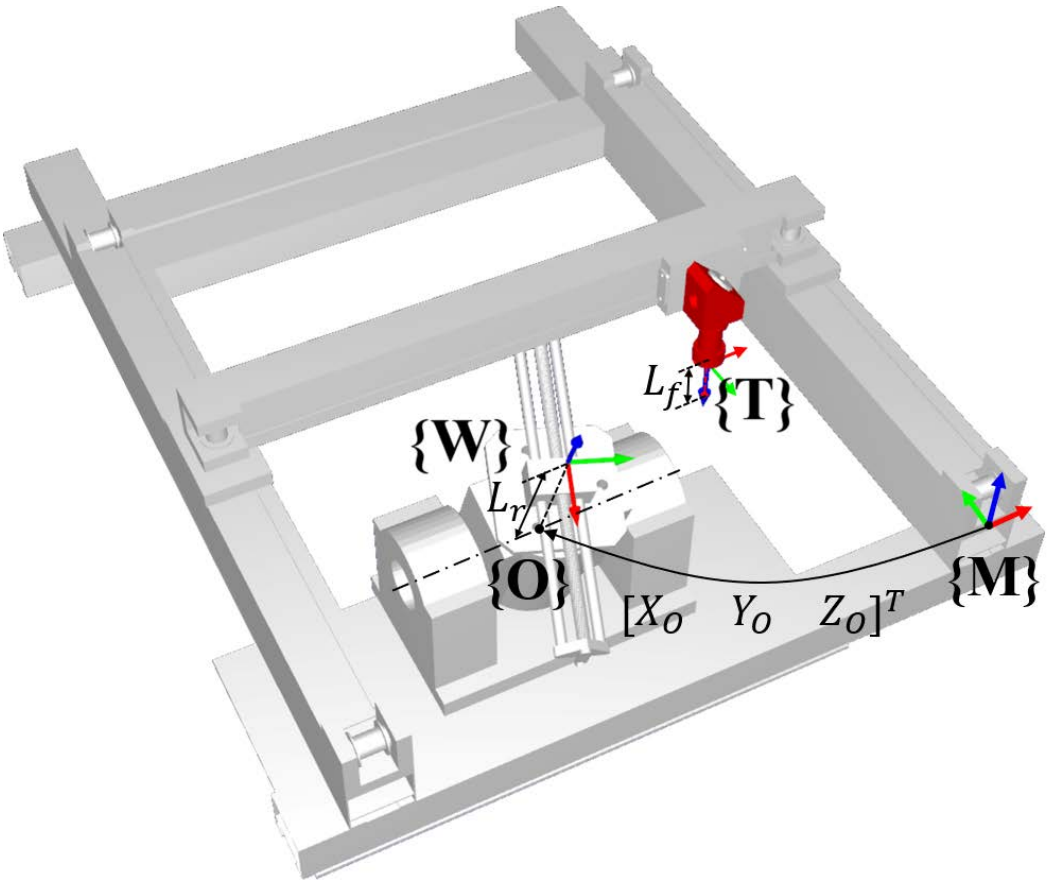

Figure 7.7: Coordinate systems definitions Four coordinates frames are defined on the system: {**M**}, {**T**}, {**W**}, {**O**}. L_f is the focal length of the laser nuzzle. L_r is the length of the rotary platform's tilting link. X_O, Y_O, Z_O are the distance between {**M**} and {**O**} along each axis.

point between the two rotary axes, or, rotary center frame {**O**}. {**O**} is vertically aligned with {**W**}, and remains stationary relative to {**M**}.

The toolpath generation is modified from the 7-DoF robotic toolpath algorithm. Similar to the toolpath generation described in Chapter 5, 3D model of the implant and the segmented defect edge wall from the 3D scanned defect model are still used for generating the cutting locations and vectors (same as the TCP in Chapter 5). Because of the 5-DoF, the cutting vectors must be

in the rotating plane along the Z axis of {**W**}. By inputting the registration information between the 3D scanned model and the implant in the laser space, the system can compute the best-fit cutting vector for each cutting location along the defect wall while satisfying this constraint (Figure 7.8).

7.3.6 Kinematics

The generated cutter locations and angles are defined in {**W**} frame. Here, the author demonstrates the basic algorithm to convert them into machine's joint values useful for generating G-code (for GRBL controller to read).

The n^{th} discretized cutter location point, $\mathbf{p_n}$, and its corresponding unit cutting vector, $\mathbf{v_n}$, are defined in {**W**}. It is then transformed to {**M**} via coordinate frame {**O**}. To align the laser beam to the cutting vector $\mathbf{v_n}$, the rotary table rotates the implant fixture platform, since the laser beam always points straight down. Therefore, the ${}^{O}H_{W}$ is defined by the rotation angles $\{\theta_4,\ \theta_5\}$ (Figure 7.9):

$$\theta_4 = \mathbf{v_n} \cdot \mathbf{z_0}$$

in which $\mathbf{z_0} = [0, 0, 1]$. and $\theta_5 = n \cdot \frac{2\pi}{N}$, in which N is the total number of input cutter locations. Therefore:

$${}^{O}H_{W} = \begin{bmatrix} cos(\theta_5) & -sin(\theta_5) & 0 & 0 \\ cos(\theta_4) \cdot sin(\theta_5) & cos(\theta_4) \cdot cos(\theta_5) & -sin(\theta_4) & -sin(\theta_4) \cdot L_r \\ sin(\theta_4) \cdot sin(\theta_5) & sin(\theta_4) \cdot cos(\theta_5) & cos(\theta_4) & cos(\theta_4) \cdot L_r \\ 0 & 0 & 0 & 1 \end{bmatrix}$$

where L_r is the length of the tilting link measured from the rotary center to the top of the workpiece platform.

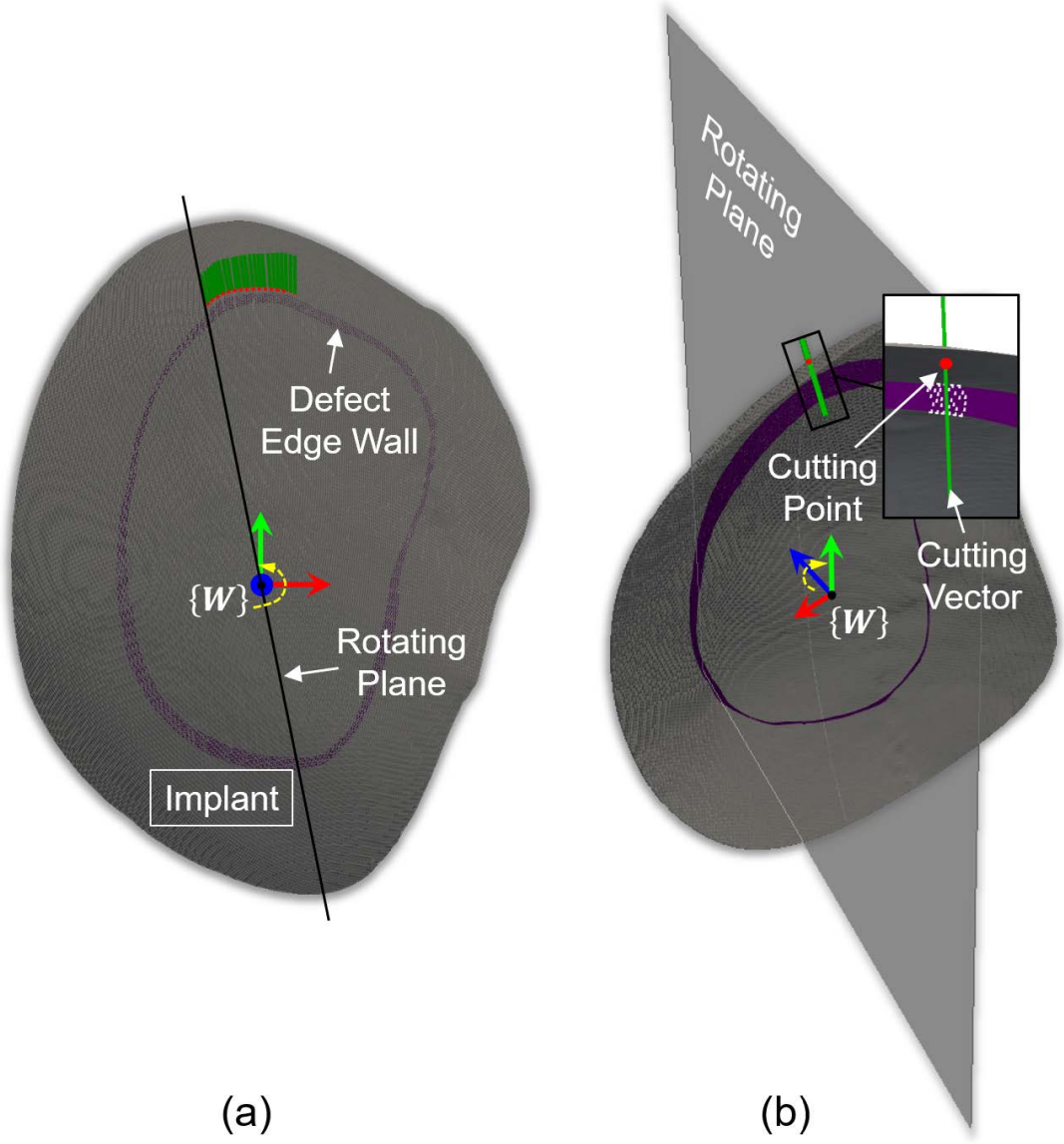

Figure 7.8: 5-Axis toolpath generation Given implant and defect edge in {**W**}, a rotating plane spins around it Z-axis up to a full circle. A best-fit vector (green) within the plane to the defect wall is generated. The vector intersects with the implant (red) is the cutter location. (a) Top view. (b) Bottom isometric view.

The transformation from {**T**} to {**O**} is then:

$$ {}^{T}H_{O} = \begin{bmatrix} 1 & 0 & 0 & -X_O \\ 0 & -1 & 0 & -Y_O \\ 0 & 0 & -1 & Z_O - L_f \\ 0 & 0 & 0 & 1 \end{bmatrix} $$

where $[X_O,\ Y_O,\ Z_O]^T$ are the measured distances between the rotary center and {**M**} along each axis, and L_f is the focal length of the laser nuzzle's lens.

Henceforth, given a cutter location **p** in {**W**}, ${}^{W}\mathbf{p}$, its corresponding coordinates in {**T**} are:

$$ {}^{T}\mathbf{p} = {}^{T}H_{O}\,{}^{O}H_{W}\,{}^{W}\mathbf{p} $$

The laser nuzzle, starting from its home location {**T**}, moves to meet the new location {$\mathbf{T_n}$} by the translation defined by ${}^{T}\mathbf{p}$.

7.4 Experiment Setup and Results

In this study, the author 3D printed a skull model based on the CT model of the second cadaver skull used in Chapter 5. A defect was created at a similar location as described in Chapter 5. An oversized implant was designed using Meshmixer[1] and 3D printed. A PMMA replica of the implant was produced by resin casting, which is compatible for laser cutting. The defect geometry was captured using a handheld 3D laser scanner and registered to the CT space, as described in Chapter 4. An oversized PMMA implant was installed on the laser system and registered to the laser space, as described in the previous

[1]Meshmixer: https://www.meshmixer.com/

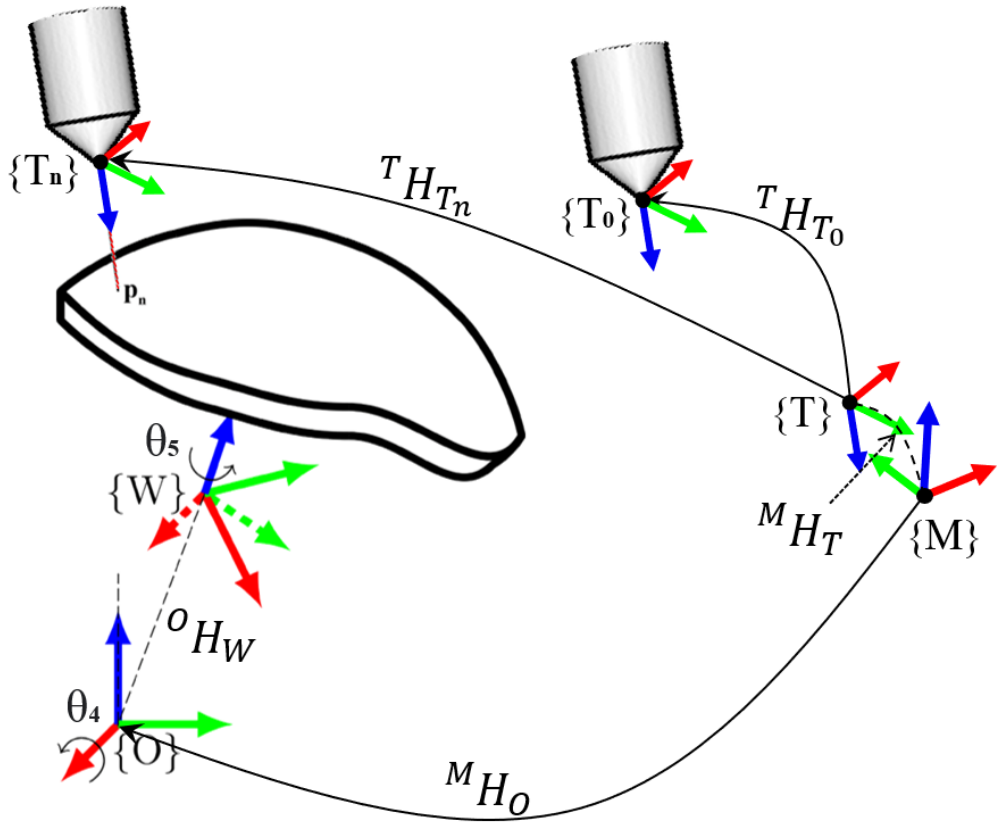

Figure 7.9: Laser system kinematics The homogeneous transformations between the defined coordinates frames.

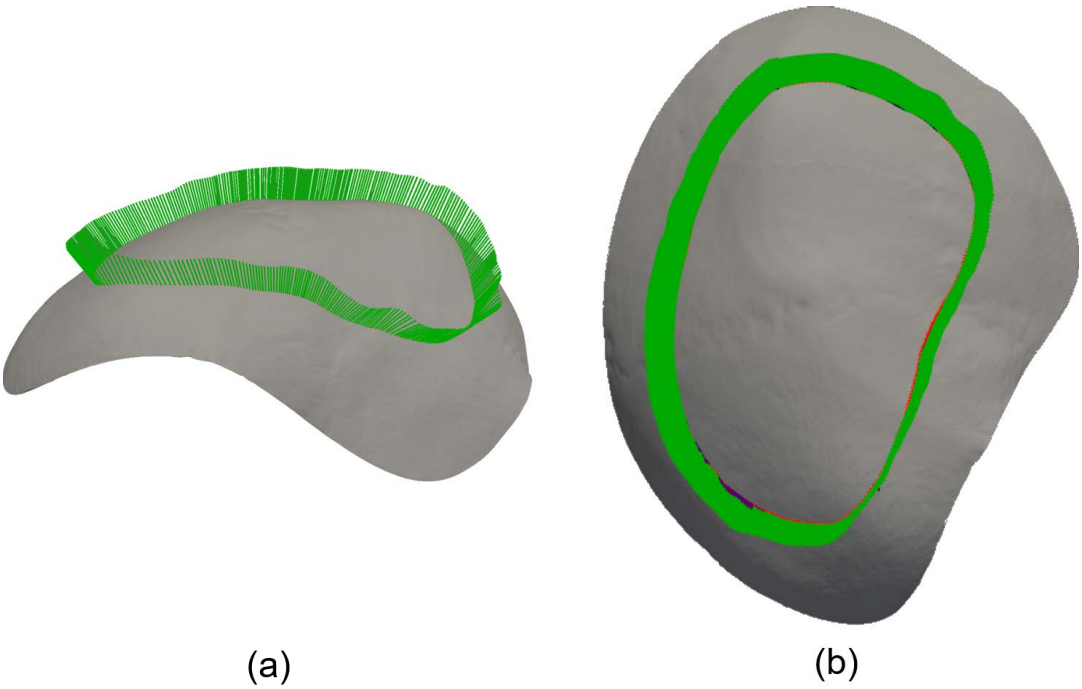

Figure 7.10: Generated 5-axis toolpath A 5-Axis toolpath is generated based on the defect geometry.

section.

A 5-Axis toolpath was generated to resize the implant using the laser system, based on the description of Section 7.3.5, as shown in Figure 7.10. The cutting locations and cutting vectors are similar to that from the original cadaver skull used in the robotic system.

Resizing accuracy was evaluated using the same method as described in Chapters 4 and 5. First, the skull geometry, with the resized implant fitted into the defect, was captured by a 3D scanner, and was then registered to the CT space. Second, the resized implant was scanned by the 3D scanner and registered to the CT space, so that its edge and top surface could be segmented in Meshmixer. The fitting accuracy was quantified by 1) the gap distance

between the edge of the defect and the edge of the resized implant; 2) the signed distance between the "perfect" skull surface and the resized implant's surface.

Both the edge gaps and the signed surface differences are computed using Meshlab[2], as shown in Figure 7.11 and Figure 7.12. The mean gap distance of the resized implants by the laser cutting and by the manual approach are 1.44 *mm* and 6.28 *mm* respectively. The maximum gaps are 2.41 *mm* and 14.48 *mm* respectively. The Root Mean Square (RMS) of the signed surface difference are 0.6 *mm* and 3.7 *mm*. The maximum difference are 0.47 *mm* and 9.18 *mm* respectively.

Since the defect was created at a similar location of the original cadaver's head, it is also valid to directly compare the resizing accuracy between the robot-cut implant and the laser-cut implant. When reviewing the results from Chapter 5, the resized implant from the laser system has higher fitting accuracy compared to that from the robot system.

7.5 Summary and Discussion

This study introduced a 5-axis laser system for the CCI resizing for the single-stage cranioplasty. The improved control system for the laser cutting, together with the accurate registration method discussed in the previous Chapters, has improved the resizing accuracy and shorten the resizing time over the conventional manual method and the robotic system.

The skull model used for testing had the same geometry as the cadaver

[2]Meshlab: https://www.meshlab.net/

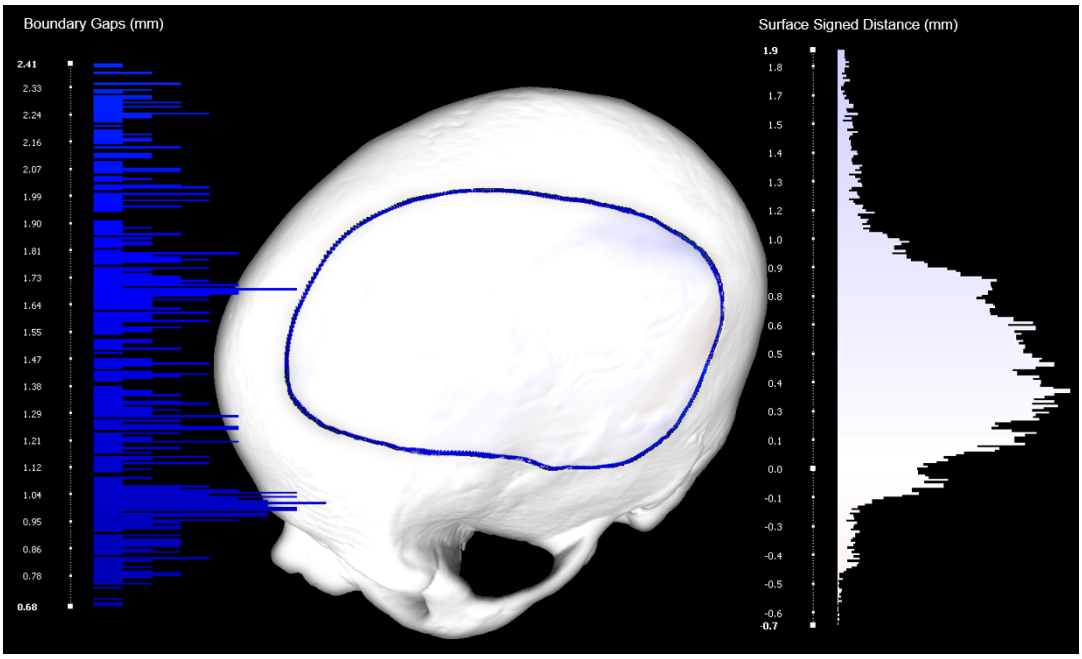

Figure 7.11: Resized implant by laser cutting Evaluation of the resized implant by laser cutting.

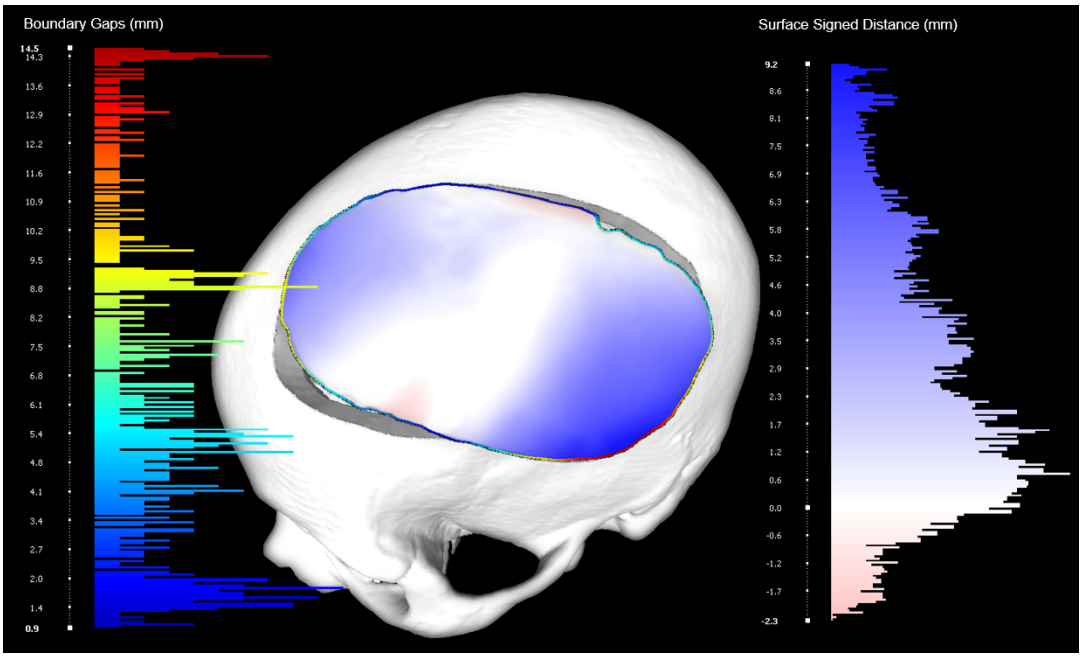

Figure 7.12: Resized implant by manual cutting Evaluation of the resized implant by manual cutting.

skull used by the robotic system. A defect was created on the 3D printed partial skull at a similar position and shape to the defect created on the cadaver skull. Therefore, we can directly compare the laser-resized CCI with robot-resized CCI in terms of accuracy. The laser system improved the resizing accuracy by 47% over the robotic system in terms of mean edge gaps and 77% over the manual approach.

As mentioned in the previous Chapter, another important factor for the implant fitting is the signed distances between the "perfect" skull and the resized implant's surface. Excessive protrusion of the implant is not ideal since it causes noticeable asymmetry. In the previous Chapter, the robot-resized implant had a lower signed distance RMS compared to the manual approach. The laser-resized implant showed a signed distance RMS 84% lower compared to the manual-resized implant. Comparing the signed distance RMS between the laser-resized and robot-resized, the laser-resized implant was 66% smaller compared to the robot-resized implant on a similar defect.

Therefore, the laser-resized implant almost matched the "perfect" skull. The close fit enables the possibility of non-screw fixation for the fitted implant. Usually, titanium plates and strips are used to fixate the implant, which causes protrusions (Figure 7.13). The protrusions may lead to infections requiring revision surgery. The laser-resized implant provides better skull continuity, as the reconstructed skull is very much similar to the "perfect" skull. Although the non-screw fixation requires the surgeon to drill a minimum of three matching holes on the patient's skull and the implant for the internal fixation (Figure 7.14), this internal fixation method may become a superior

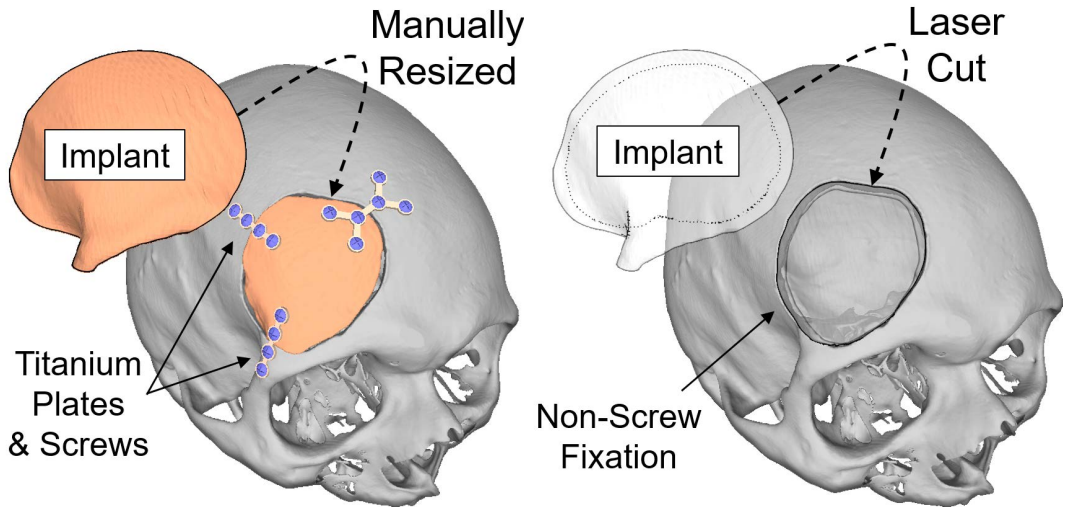

Figure 7.13: Conventional fixation vs. Tangential non-screw fixation Conventional cranial implant fixation uses titanium plates and screws. A non-screw fixation can be utilized when the resized implant attains a close fit to the skull.

choice.

The proposed laser and robotic systems are vastly compatible, as they share a similar registration method and a slightly modified toolpath generation method. Therefore, it is easy to switch between these two systems whenever deemed necessary.

The high resizing accuracy of the laser also implies other applications for the system, such as laser milling. This allows an instrument device to be installed inside the skull for various medical applications, as mentioned in Section 7.1. The details and the preliminary result for laser milling are described in the final Chapter.

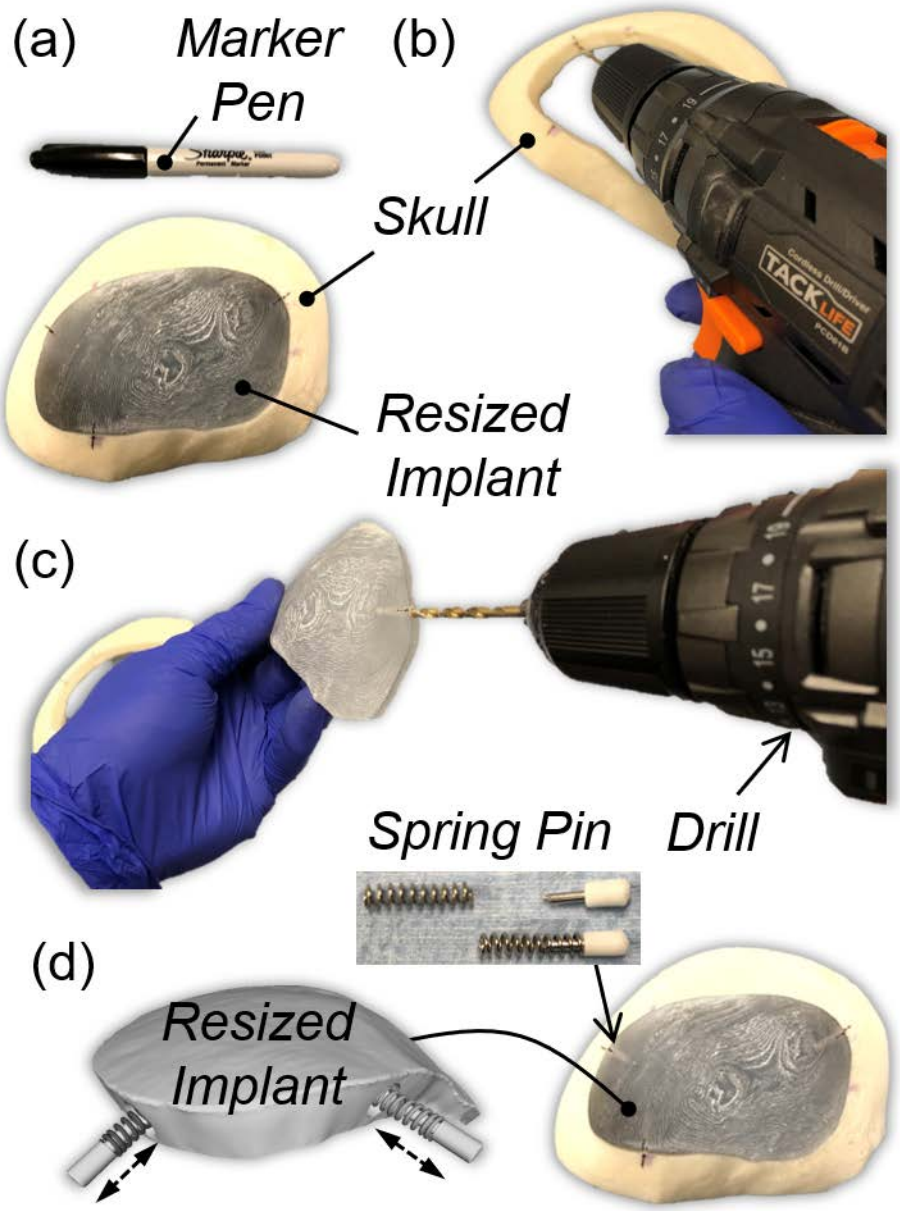

Figure 7.14: Non-screw fixation method (a) Using a marker pen to mark a minimum of three locations for inserting spring pins. (b) Drilling small holes on the edge of the resected skull at the marked location. (c) Drilling holes on the edge of the resized implant at the marked location. (d) Inserting the spring pins into the implant's drilled holes and fitted to the skull.

Chapter 8

Conclusion

8.1 Summary

A clinical approach for single-stage cranioplasty requires the surgeon to manually trim a prefabricated oversized CCI using a surgical cutter to reduce its size until it fits the cranial defect. During this process, the surgeon has to gauge the size and shape of the defect by eyeballing, which is imprecise and time-consuming. The amount of time spent on manual CCI modification may take ten to eighty minutes reported by Berli et al. [12]. Therefore, to improve the intraoperative CCI modification's speed and accuracy, three major systems are developed, as described in this dissertation:

- A Portable Projection Mapping Device (PPMD)
- A robotic cutting workstation
- A 5-axis laser cutting system

A PPMD system is introduced based on projection AR to provide the surgeon visual guidance while outlining the defect boundary on the oversized

CCI. The system comprises a miniature OTS to accomplish real-time surgical navigation and patient-to-CT registration. The projection mapping allows the surgeon to verify the registration immediately and guides the surgeon during the manual resizing process. The digitization and registration of the defect geometry potentially make the automation of the CCI resizing process possible.

Next, the resizing process is automated by introducing a robotic cutting system. It utilizes anatomical features of the skull acquired via 3D scanning to accomplish patient-to-CT registration. However, surgical draping makes these anatomical features unattainable. Therefore, reattachable fiducial markers are designed to provide additional registration correspondence between the patient and the CT. The 2-scan method provides an accurate registration.

A toolpath algorithm is developed to further automate the resizing process to generate cutting locations for the robot based on the 3D scanned defect model. The algorithm is updated to account for the defect's beveled edge wall so that the resized implant's edge matches with the defect. This improves the resizing accuracy of the implant over the manual approach.

To minimize the limitations brought by the mechanical cutting, a 5-axis laser cutting is proposed and developed. Using the same registration method as the robotic system and slightly modified toolpath generation algorithm, the laser cutting system provides a smoother and more accurate implant resizing compared to the manual approach, and presumably, the robotic system. The precise CCI resizing demonstrated by the laser system indicates many potential applications in neuroplastic surgery, as discussed in the next

Section.

8.2 Limitations and Future Work

In Chapter 7, the laser system is tested on a 3D-printed partial skull based on the cadaver's head used in Chapter 5. Although the similar skull geometry and defect location and shape indicate that laser cutting improves the resizing accuracy over the mechanical cutting by the robot, a direct comparison between the laser system and the robotic system will be more convincing to demonstrate the improvement. Therefore, future work should consider conducting a broad sampling of resized CCIs by both laser and robotic systems on a number of skulls with different defect locations and geometries. The broad sampling study is also meaningful to quantify the significance of accuracy improvements by the proposed systems over the conventional approach.

As mentioned in Chapter 7, the laser system has the potential of performing milling, which creates a pocket on the CCI for housing instrumented devices. Some of the examples are shown in Figure 8.1. Depending on the shape of the device, there are generally two types of pocket profiles, as shown in Figure 8.2: a flat or curved bottom, to offset the curvature of the implant's top surface.

Given the dimension of a device, the laser system can produce a pocket with a flat bottom or a curvature bottom using the following algorithm (Figure 8.3). After the implant is registered to the laser space, the surgeon inputs the device's dimension and location on the implant and calculated the intersected volume via boolean operation. To generate flat bottom milling toolpath, the intersected volume is then sliced along Z-axis into multiple layers, and

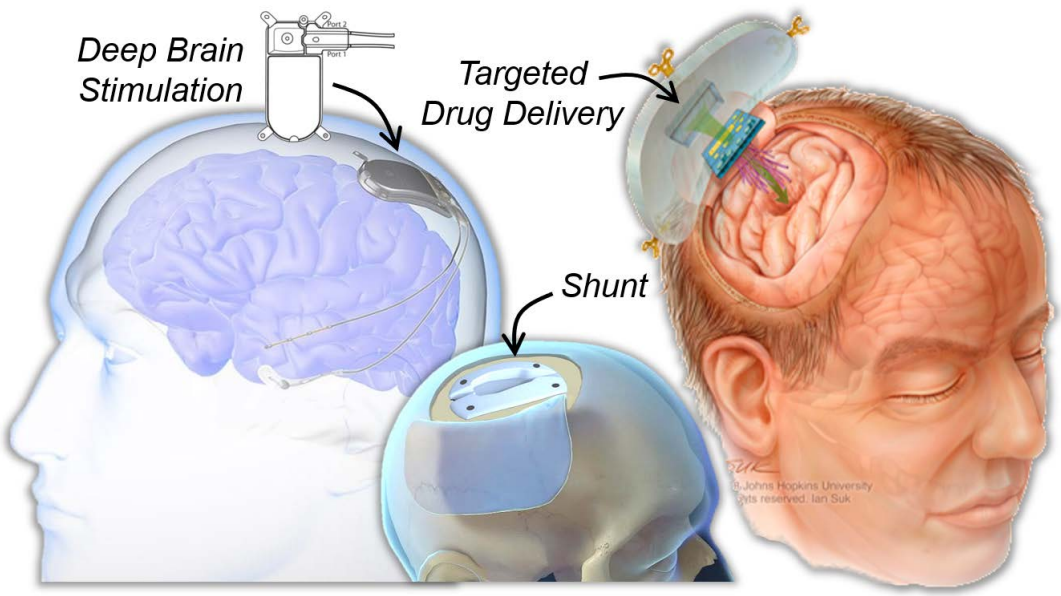

Figure 8.1: Examples of instrumented implants Image courtesy of https://www.neuropace.com, https://clinicalconnection.hopkinsmedicine.org/neurology-and-neurosurgery-articles, https://www.hopkinsmedicine.org/neuroplastic-surgery

each layer is filled with hatching lines. The generated hatching lines can then be post-processed into G-code for the laser system.

To generate curved bottom milling toolpath, the intersected volume is further segmented to get its top surface. The top surface is then used to generate hatching lines along the X-axis and Y-axis. Next, the two types of hatching lines are alternately stacked along the Z-axis to form a cutting volume of height h. Lastly, the generated toolpath can be converted into G-code and inputted into the laser system to create the pocket on the CCI via laser milling.

A preliminary test has demonstrated the laser system's capability in creating a pocket on the CCI for embedding instrumented devices, as shown in Figure 8.4. Further studies are necessary to show the dimensional accuracy of

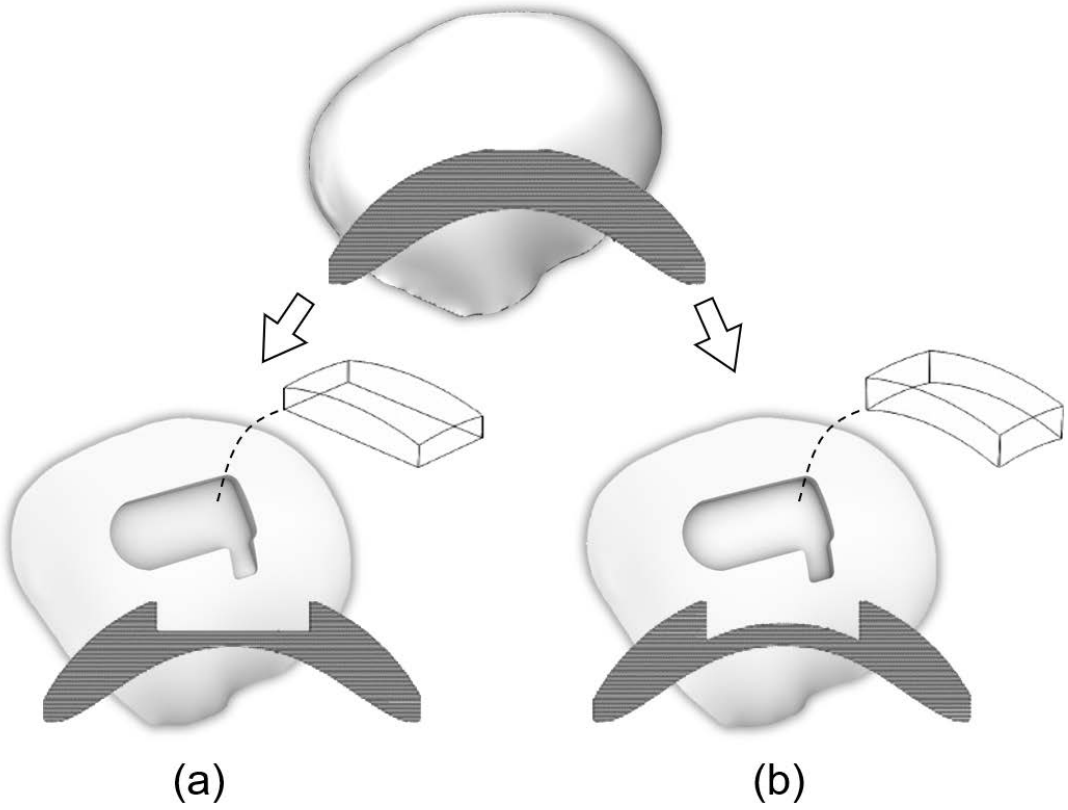

Figure 8.2: Two types of laser milling profiles (a) Flat bottom. (b) Offset bottom.

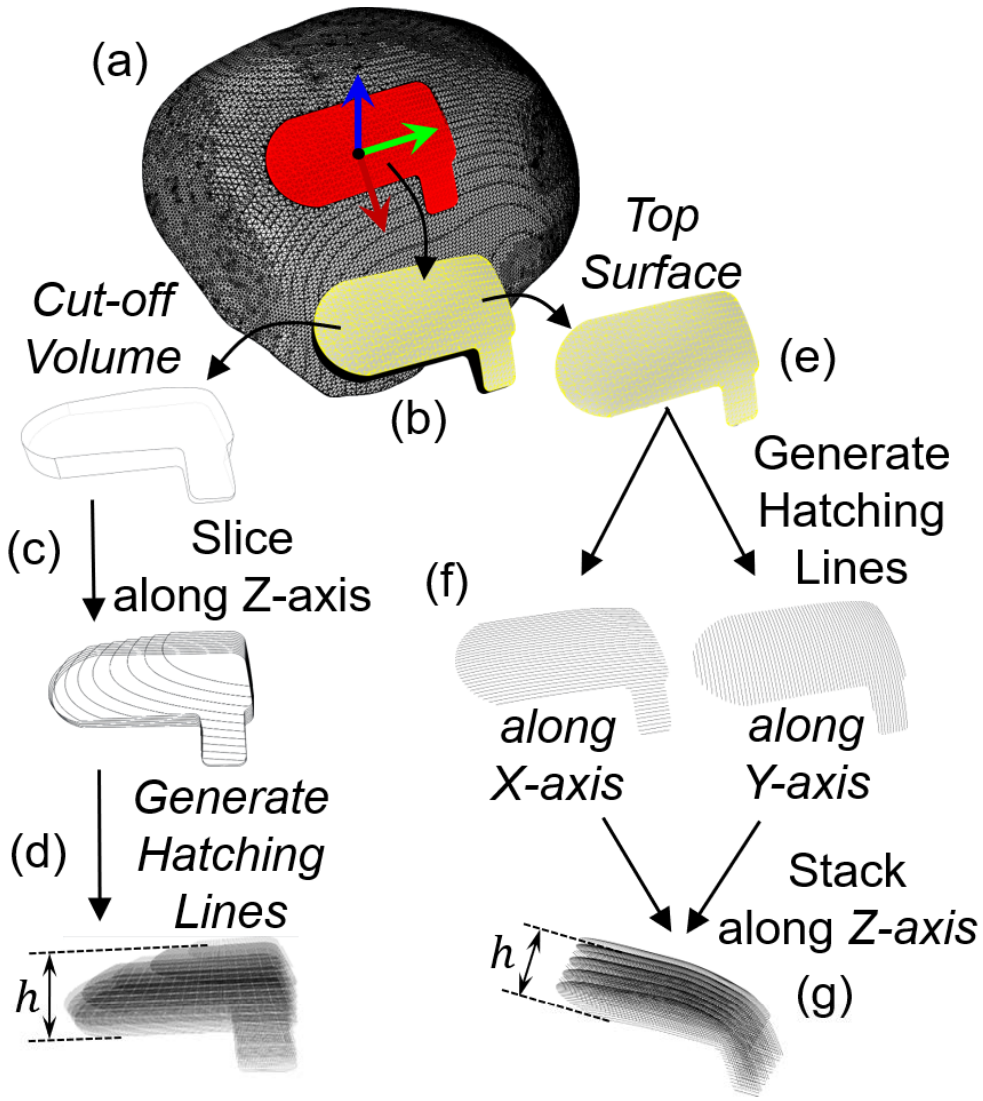

Figure 8.3: Laser milling toolpath generation (a) Inputting the dimension and location of the device on the implant. (b) Generating the cut-off volume. The height of cut-off volume is *h*. (c) Slicing the cut-off volume along Z-axis. (d) Generating hatching lines for each sliced layer. (e) Slicing the top surface of the cut-off volume. (f) Generating a single layer of hatching lines along X-axis and Y-axis. (g) Stacking the layers along Z-axis.

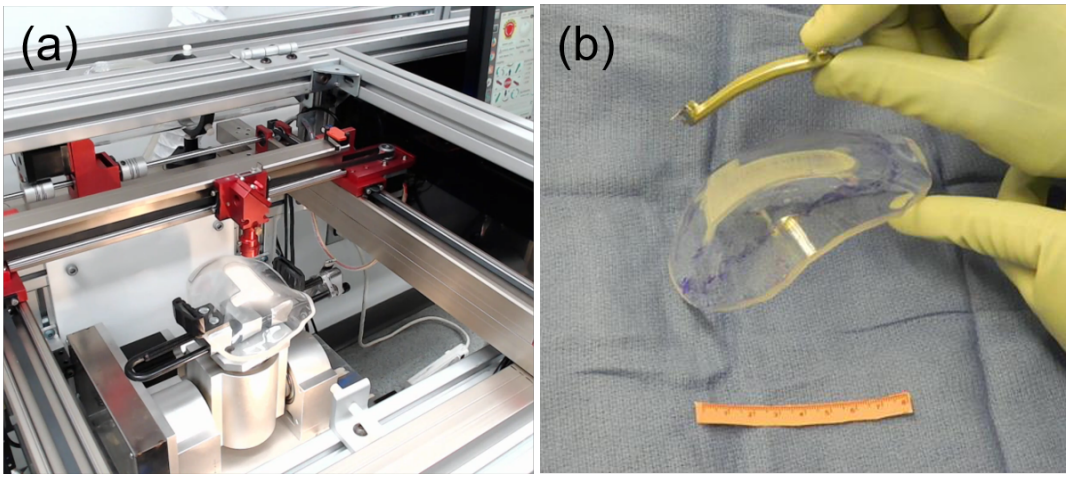

Figure 8.4: Laser milling preliminary test A preliminary laser milling test. (a) A pocket was created on a transparent PMMA implant by the laser system via milling. (b) The created pocket matched the dimension of the Neuropace device.

the created pocket using the same accuracy evaluation method described in the previous Chapters.

References

[1] Chad R Gordon, Judy Huang, and Henry Brem. "Neuroplastic surgery". In: *Journal of Craniofacial Surgery* vol. 29. no. 1 2018, pp. 4–5.

[2] Christina Marie Pasick, Konstantinos Margetis, Gabriel F Santiago, Chad Gordon, and Peter J Taub. "Adult Cranioplasty". In: *Journal of Craniofacial Surgery* vol. 30. no. 7 2019, pp. 2138–2143.

[3] Chad R Gordon. "The special field of neuroplastic surgery". In: *Journal of Craniofacial Surgery* vol. 32. no. 1 2021, pp. 3–7.

[4] Francis C Grant and Nathan C Norcross. "Repair of cranial defects by cranioplasty". In: *Annals of surgery* vol. 110. no. 4 1939, p. 488.

[5] Sanan Abhay and Stephen J Haines. "Repairing holes in the head: a history of cranioplasty". In: *Neurosurgery* vol. 40. no. 3 1997, pp. 588–603.

[6] Seckin Aydin, Baris Kucukyuruk, Bashar Abuzayed, Sabri Aydin, and Galip Zihni Sanus. "Cranioplasty: review of materials and techniques". In: *Journal of neurosciences in rural practice* vol. 2. no. 2 2011, p. 162.

[7] Abdullah H Feroze, Graham G Walmsley, Omar Choudhri, H Peter Lorenz, Gerald A Grant, and Michael SB Edwards. "Evolution of cranioplasty techniques in neurosurgery: historical review, pediatric considerations, and current trends". In: *Journal of neurosurgery* vol. 123. no. 4 2015, pp. 1098–1107.

[8] Mirko S Gilardino, Mihiran Karunanayake, Taghreed Al-Humsi, Ali Izadpanah, Hasan Al-Ajmi, Judith Marcoux, Jeffrey Atkinson, and Jean-Pierre Farmer. "A comparison and cost analysis of cranioplasty techniques: autologous bone versus custom computer-generated implants". In: *Journal of Craniofacial Surgery* vol. 26. no. 1 2015, pp. 113–117.

[9] Chad R Gordon, Mark Fisher, Jason Liauw, Ioan Lina, Varun Puvanesarajah, Srinivas Susarla, Alexander Coon, Michael Lim, Alfredo Quinones-Hinojosa, Jon Weingart, et al. "Multidisciplinary approach for improved outcomes in secondary cranial reconstruction: introducing the pericranial-onlay cranioplasty technique". In: *Operative neurosurgery* vol. 10. no. 2 2014, pp. 179–190.

[10] Manuel Dujovny, Alberto Aviles, Celso Agner, Patricia Fernandez, and Fady T Charbel. "Cranioplasty: cosmetic or therapeutic?" In: *Surgical neurology* vol. 47. no. 3 1997, pp. 238–241.

[11] Amir Wolff, Gabriel F Santiago, Micah Belzberg, Charity Huggins, Michael Lim, Jon Weingart, William Anderson, Alex Coon, Judy Huang, Henry Brem, et al. "Adult cranioplasty reconstruction with customized cranial implants: preferred technique, timing, and biomaterials". In: *Journal of Craniofacial Surgery* vol. 29. no. 4 2018, pp. 887–894.

[12] Jens U Berli, Lauren Thomaier, Shuting Zhong, Judy Huang, Alfredo Quinones, Michael Lim, Jon Weingart, Henry Brem, and Chad R Gordon. "Immediate single-stage cranioplasty following calvarial resection for benign and malignant skull neoplasms using customized craniofacial implants". In: *Journal of Craniofacial Surgery* vol. 26. no. 5 2015, pp. 1456–1462.

[13] Sai-Cheung Lee, Chieh-Tsai Wu, Shih-Tseng Lee, and Po-Jen Chen. "Cranioplasty using polymethyl methacrylate prostheses". In: *Journal of clinical neuroscience* vol. 16. no. 1 2009, pp. 56–63.

[14] Corrado Iaccarino, Angelos G Kolias, Louis-Georges Roumy, Kostas Fountas, and Amos Olufemi Adeleye. "Cranioplasty following decompressive craniectomy". In: *Frontiers in neurology* vol. 10 2020, p. 1357.

[15] David J Bonda, Sunil Manjila, Warren R Selman, and David Dean. "The recent revolution in the design and manufacture of cranial implants: modern advancements and future directions". In: *Neurosurgery* vol. 77. no. 5 2015, pp. 814–824.

[16] A Matsuno, H Tanaka, H Iwamuro, S Takanashi, S Miyawaki, M Nakashima, H Nakaguchi, and T Nagashima. "Analyses of the factors influencing bone graft infection after delayed cranioplasty". In: *Acta neurochirurgica* vol. 148. no. 5 2006, pp. 535–540.

[17] J Joffe, M Harris, F Kahugu, S Nicoll, A Linney, and R Richards. "A prospective study of computer-aided design and manufacture of titanium plate for cranioplasty and its clinical outcome". In: *British journal of neurosurgery* vol. 13. no. 6 1999, pp. 576–580.

[18] Stephan Weihe, Michael Wehmöller, Henning Schliephake, Stefan Haßfeld, Alexander Tschakaloff, Jörg Raczkowsky, and Harald Eufinger. "Synthesis of CAD/CAM, robotics and biomaterial implant fabrication: single-step reconstruction in computer aided frontotemporal bone resection". In: *International journal of oral and maxillofacial surgery* vol. 29. no. 5 2000, pp. 384–388.

[19] David Dean, Kyoung-June Min, and Angus Bond. "Computer aided design of large-format prefabricated cranial plates". In: *Journal of Craniofacial Surgery* vol. 14. no. 6 2003, pp. 819–832.

[20] Aatman M Shah, Henry Jung, and Stephen Skirboll. "Materials used in cranioplasty: a history and analysis". In: *Neurosurgical focus* vol. 36. no. 4 2014, E19.

[21] E Heissler, F-S Fischer, S Boiouri, T Lehrnann, W Mathar, A Gebhardt, W Lanksch, and J Bler. "Custom-made cast titanium implants produced with CAD/CAM for the reconstruction of cranium defects". In: *International journal of oral and maxillofacial surgery* vol. 27. no. 5 1998, pp. 334–338.

[22] André Luiz Jardini, Maria Aparecida Larosa, Cecília Amélia de Carvalho Zavaglia, Luis Fernando Bernardes, Carlos Salles Lambert, Paulo Kharmandayan, Davi Calderoni, and Rubens Maciel Filho. "Customised titanium implant fabricated in additive manufacturing for craniomaxillofacial surgery: This paper discusses the design and fabrication of a metallic implant for the reconstruction of a large cranial defect". In: *Virtual and physical prototyping* vol. 9. no. 2 2014, pp. 115–125.

[23] Ciaran Scott Hill, Astri Maria Valpuri Luoma, Sally R Wilson, and Neil Kitchen. "Titanium cranioplasty and the prediction of complications". In: *British journal of neurosurgery* vol. 26. no. 6 2012, pp. 832–837.

[24] Soumya Mukherjee, Bhaskar Thakur, Imran Haq, Samantha Hettige, and Andrew J Martin. "Complications of titanium cranioplasty—a retrospective analysis of 174 patients". In: *Acta neurochirurgica* vol. 156. no. 5 2014, pp. 989–998.

[25] Gary J Huang, Susan Zhong, Srinivas M Susarla, Edward W Swanson, Judy Huang, and Chad R Gordon. "Craniofacial reconstruction with poly (methyl methacrylate) customized cranial implants". In: *Journal of Craniofacial Surgery* vol. 26. no. 1 2015, pp. 64–70.

[26] Luigi Chiarini, Sabina Figurelli, Giuseppe Pollastri, Elio Torcia, Francesca Ferrari, Massimo Albanese, and Pier Francesco Nocini. "Cranioplasty using acrylic material: a new technical procedure". In: *Journal of craniomaxillofacial surgery* vol. 32. no. 1 2004, pp. 5–9.

[27] Tamir Shay, Kerry-Ann Mitchell, Micah Belzberg, Ian Zelko, Smruti Mahapatra, Jason Qian, Luis Mendoza, Judy Huang, Henry Brem, and Chad Gordon. "Translucent Customized Cranial Implants Made of Clear Polymethylmethacrylate: An Early Outcome Analysis of 55 Consecutive Cranioplasty Cases". In: *Annals of plastic surgery* vol. 85. no. 6 2020, e27–e36.

[28] Bernd Lethaus, Monique Bloebaum, Brigitte Essers, Marielle Poort ter Laak, Timm Steiner, and Peter Kessler. "Patient-specific implants compared with stored bone grafts for patients with interval cranioplasty". In: *Journal of Craniofacial Surgery* vol. 25. no. 1 2014, pp. 206–209.

[29] Jibo Zhang, Weiqun Tian, Jiayi Chen, Jin Yu, Jianjian Zhang, and Jincao Chen. "The application of polyetheretherketone (PEEK) implants in cranioplasty". In: *Brain research bulletin* vol. 153 2019, pp. 143–149.

[30] Harald Eufinger, Albert RM Wittkampf, Michael Wehmöller, and Frans W Zonneveld. "Single-step fronto-orbital resection and reconstruction with individual resection template and corresponding titanium implant: a new method of computer-aided surgery". In: *Journal of Cranio-Maxillofacial Surgery* vol. 26. no. 6 1998, pp. 373–378.

[31] Giovanni Gerbino, Francesca Antonella Bianchi, Emanuele Zavattero, Fulvio Tartara, Diego Garbossa, and Alessandro Ducati. "Single-step resection and reconstruction using patient-specific implants in the treatment of benign cranio-orbital tumors". In: *Journal of Oral and Maxillofacial Surgery* vol. 71. no. 11 2013, pp. 1969–1982.

[32] P Bast, A Popovic, T Wu, S Heger, M Engelhardt, W Lauer, K Radermacher, and K Schmieder. "Robot-and computer-assisted craniotomy: resection planning, implant modelling and robot safety". In: *The International Journal of Medical Robotics and Computer Assisted Surgery* vol. 2. no. 2 2006, pp. 168–178.

[33] F Jalbert, S Boetto, F Nadon, F Lauwers, E Schmidt, and R Lopez. "One-step primary reconstruction for complex craniofacial resection with PEEK custom-made implants". In: *Journal of Cranio-Maxillofacial Surgery* vol. 42. no. 2 2014, pp. 141–148.

[34] Marcos Vinicius Marques Anchieta, Fábio Andrey Salles, Bruno D Cassaro, Marcelo Marques Quaresma, and Bruno Fernandes de Oliveira Santos. "Skull reconstruction after resection of bone tumors in a single surgical time by the association of the techniques of rapid prototyping and surgical navigation". In: *International journal of computer assisted radiology and surgery* vol. 11. no. 10 2016, pp. 1919–1925.

[35] Philippe Dodier, Fabian Winter, Thomas Auzinger, Gabriel Mistelbauer, Josa M Frischer, Wei-Te Wang, Ammar Mallouhi, Wolfgang Marik, Stefan Wolfsberger, Lukas Reissig, et al. "Single-stage bone resection and cranioplastic reconstruction: comparison of a novel software-derived PEEK workflow with the standard reconstructive method". In: *International journal of oral and maxillofacial surgery* vol. 49. no. 8 2020, pp. 1007–1015.

[36] Ali-Reza Fathi, Serge Marbacher, and Anton Lukes. "Cost-effective patient-specific intraoperative molded cranioplasty". In: *Journal of craniofacial surgery* vol. 19. no. 3 2008, pp. 777–781.

[37] Serge Marbacher, Lukas Andereggen, Salome Erhardt, Ali-Reza Fathi, Javier Fandino, Andreas Raabe, and Jürgen Beck. "Intraoperative template-molded bone flap reconstruction for patient-specific cranioplasty". In: *Neurosurgical review* vol. 35. no. 4 2012, pp. 527–535.

[38] Bum-Joon Kim, Ki-Sun Hong, Kyung-Jae Park, Dong-Hyuk Park, Yong-Gu Chung, and Shin-Hyuk Kang. "Customized cranioplasty implants using three-dimensional printers and polymethyl-methacrylate casting". In: *Journal of Korean Neurosurgical Society* vol. 52. no. 6 2012, p. 541.

[39] Eun-Kyung Park, Jun-Young Lim, In-Sik Yun, Ju-Seong Kim, Su-Heon Woo, Dong-Seok Kim, and Kyu-Won Shim. "Cranioplasty enhanced by three-dimensional printing: custom-made three-dimensional-printed titanium implants for skull defects". In: *Journal of Craniofacial Surgery* vol. 27. no. 4 2016, pp. 943–949.

[40] Jesús A Morales-Gómez, Everardo Garcia-Estrada, Jorge E Leos-Bortoni, Miriam Delgado-Brito, Luis E Flores-Huerta, A Adriana, Luis J Torres-Díaz, and Ángel R Martínez-Ponce de León. "Cranioplasty with a low-cost customized polymethylmethacrylate implant using a desktop 3D printer". In: *Journal of neurosurgery* vol. 130. no. 5 2018, pp. 1721–1727.

[41] Christian A Bowers, Jaron H McMullin, Cameron Brimley, Linsey Etherington, Faizi A Siddiqi, and Jay Riva-Cambrin. "Minimizing bone gaps when using custom pediatric cranial implants is associated with implant success". In: *Journal of Neurosurgery: Pediatrics* vol. 16. no. 4 2015, pp. 439–444.

[42] Ryan J Murphy, Kevin C Wolfe, Peter C Liacouras, Gerald T Grant, Chad R Gordon, and Mehran Armand. "Computer-assisted single-stage cranioplasty". In: *2015 37th Annual International Conference of the IEEE Engineering in Medicine and Biology Society (EMBC)*. IEEE. 2015, pp. 4910–4913.

[43] Ryan J Murphy, Peter C Liacouras, Gerald T Grant, Kevin C Wolfe, Mehran Armand, and Chad R Gordon. "A craniomaxillofacial surgical assistance workstation for enhanced single-stage reconstruction using patient-specific implants". In: *Journal of Craniofacial Surgery* vol. 27. no. 8 2016, pp. 2025–2030.

[44] Ivan E Sutherland. "A head-mounted three dimensional display". In: *Proceedings of the December 9-11, 1968, fall joint computer conference, part I*. 1968, pp. 757–764.

[45] Michael Bajura, Henry Fuchs, and Ryutarou Ohbuchi. "Merging virtual objects with the real world: Seeing ultrasound imagery within the patient". In: *ACM SIGGRAPH Computer Graphics* vol. 26. no. 2 1992, pp. 203–210.

[46] J-P Tardif, S Roy, and J Meunier. "Projector-based augmented reality in surgery without calibration". In: *Proceedings of the 25th annual international conference of the IEEE engineering in medicine and biology society (IEEE Cat. No. 03CH37439)*. Vol. 1. IEEE. 2003, pp. 548–551.

[47] Christoph Bichlmeier, Felix Wimmer, Sandro Michael Heining, and Nassir Navab. "Contextual anatomic mimesis hybrid in-situ visualization method for improving multi-sensory depth perception in medical augmented reality". In: *2007 6th IEEE and ACM international symposium on mixed and augmented reality*. IEEE. 2007, pp. 129–138.

[48] Yi Zhou, Shuangjiu Xiao, Ning Tang, Zhiyong Wei, and Xu Chen. "Pmomo: Projection mapping on movable 3D object". In: *Proceedings of the 2016 CHI Conference on Human Factors in Computing Systems*. 2016, pp. 781–790.

[49] Florian Kral, Elisabeth J Puschban, Herbert Riechelmann, and Wolfgang Freysinger. "Comparison of optical and electromagnetic tracking for navigated lateral skull base surgery". In: *The International Journal of Medical Robotics and Computer Assisted Surgery* vol. 9. no. 2 2013, pp. 247–252.

[50] Hongliang Ren, Wei Liu, and Andy Lim. "Marker-based surgical instrument tracking using dual kinect sensors". In: *IEEE transactions on automation science and engineering* vol. 11. no. 3 2013, pp. 921–924.

[51] Abid Haleem and Mohd Javaid. "3D scanning applications in medical field: a literature-based review". In: *Clinical Epidemiology and Global Health* vol. 7. no. 2 2019, pp. 199–210.

[52] Shuya Liu, Wei-Lun Huang, Austin Shin, Chad Gordon, and Mehran Armand. "A portable projection mapping device for medical augmented reality in single-stage cranioplasty". In: *Optical Architectures for Displays and Sensing in Augmented, Virtual, and Mixed Reality (AR, VR, MR)*. Vol. 11310. International Society for Optics and Photonics. 2020, p. 1131007.

[53] Zhengyou Zhang. "A flexible new technique for camera calibration". In: *IEEE Transactions on pattern analysis and machine intelligence* vol. 22. no. 11 2000, pp. 1330–1334.

[54] Bingyao Huang, Samed Ozdemir, Ying Tang, Chunyuan Liao, and Haibin Ling. "A single-shot-per-pose camera-projector calibration system for imperfect planar targets". In: *2018 IEEE International Symposium on Mixed and Augmented Reality Adjunct (ISMAR-Adjunct)*. IEEE. 2018, pp. 15–20.

[55] Bo Sun, Li Liu, Chao Hu, and Max Q-H Meng. "Surgical instrument recognition and calibration for optical tracking system". In: *2010 IEEE International Conference on Robotics and Biomimetics*. IEEE. 2010, pp. 1376–1381.

[56] Zhentian Zhou, Bo Wu, Juan Duan, Xu Zhang, Nan Zhang, and Zhiyuan Liang. "Optical surgical instrument tracking system based on the principle of stereo vision". In: *Journal of biomedical optics* vol. 22. no. 6 2017, p. 065005.

[57] Thomas Pintaric and Hannes Kaufmann. "Affordable infrared-optical pose-tracking for virtual and augmented reality". In: *Proceedings of Trends and Issues in Tracking for Virtual Environments Workshop, IEEE VR*. 2007, pp. 44–51.

[58] Ken Cai, Rongqian Yang, Qinyong Lin, and Zhigang Wang. "Tracking multiple surgical instruments in a near-infrared optical system". In: *Computer Assisted Surgery* vol. 21. no. 1 2016, pp. 46–55.

[59] K Somani Arun, Thomas S Huang, and Steven D Blostein. "Least-squares fitting of two 3-D point sets". In: *IEEE Transactions on pattern analysis and machine intelligence* no. 5 1987, pp. 698–700.

[60] Shuya Liu, Wei-Lun Huang, Chad Gordon, and Mehran Armand. "A Robotic System for Implant Modification in Single-stage Cranioplasty". In: *arXiv preprint arXiv:2101.04303* 2021.

[61] Paul J Besl and Neil D McKay. "Method for registration of 3-D shapes". In: *Sensor fusion IV: control paradigms and data structures*. Vol. 1611. International Society for Optics and Photonics. 1992, pp. 586–606.

[62] C Bane Sullivan and Alexander A Kaszynski. "PyVista: 3D plotting and mesh analysis through a streamlined interface for the Visualization Toolkit (VTK)". In: *Journal of Open Source Software* vol. 4. no. 37 2019, p. 1450.

[63] Mark Meyer, Mathieu Desbrun, Peter Schröder, and Alan H Barr. "Discrete differential-geometry operators for triangulated 2-manifolds". In: *Visualization and mathematics III*. Springer, 2003, pp. 35–57.

[64] Wolfgang Birkfellner, Franz Watzinger, Felix Wanschitz, Rolf Ewers, and Helmar Bergmann. "Calibration of tracking systems in a surgical environment". In: *IEEE transactions on medical imaging* vol. 17. no. 5 1998, pp. 737–742.

[65] Paolo Cignoni, Marco Callieri, Massimiliano Corsini, Matteo Dellepiane, Fabio Ganovelli, and Guido Ranzuglia. "Meshlab: an open-source mesh processing tool." In: *Eurographics Italian chapter conference*. Vol. 2008. Salerno. 2008, pp. 129–136.

[66] Shuya Liu, Wei-Lun Huang, Chad Gordon, and Mehran Armand. "Automated Implant Resizing for Single-Stage Cranioplasty". In: *IEEE Robotics and Automation Letters* 2021.

[67] J Michael Fitzpatrick and Jay B West. "The distribution of target registration error in rigid-body point-based registration". In: *IEEE transactions on medical imaging* vol. 20. no. 9 2001, pp. 917–927.

[68] Radu Horaud and Fadi Dornaika. "Hand-eye calibration". In: *The international journal of robotics research* vol. 14. no. 3 1995, pp. 195–210.

[69] Frank C Park and Bryan J Martin. "Robot sensor calibration: solving AX= XB on the Euclidean group". In: *IEEE Transactions on Robotics and Automation* vol. 10. no. 5 1994, pp. 717–721.

[70] Brian Curless and Marc Levoy. "A volumetric method for building complex models from range images". In: *Proceedings of the 23rd annual conference on Computer graphics and interactive techniques*. 1996, pp. 303–312.

[71] Avanish Kumar Dubey and Vinod Yadava. "Laser beam machining—A review". In: *International Journal of Machine Tools and Manufacture* vol. 48. no. 6 2008, pp. 609–628.

[72] Pedram Parandoush and Altab Hossain. "A review of modeling and simulation of laser beam machining". In: *International journal of machine tools and manufacture* vol. 85 2014, pp. 135–145.

[73] Bai Hua Zhou and SM Mahdavian. "Experimental and theoretical analyses of cutting nonmetallic materials by low power CO2-laser". In: *Journal of materials processing technology* vol. 146. no. 2 2004, pp. 188–192.

[74] Joshua Liu, Jerry Fang, Ryan J Murphy, Chad Gordon, and Mehran Armand. "Design and development of 5-axis cranial implant laser cutting system". In: *International Design Engineering Technical Conferences and Computers and Information in Engineering Conference*. Vol. 58110. American Society of Mechanical Engineers. 2017, V001T02A051.

[75] Kevin J Gibbons, Wesley L Hicks Jr, and Lee R Guterman. "A technique for rigid fixation of methyl methacrylate cranioplasty: the vault-locking method". In: *Surgical neurology* vol. 52. no. 3 1999, pp. 310–315.

[76] Basel A Khader and Mark R Towler. "Materials and techniques used in cranioplasty fixation: A review". In: *Materials Science and Engineering: C* vol. 66 2016, pp. 315–322.

Vita

In January 2016, Shuya (Joshua) Liu enrolled in the Mechanical Engineering Ph.D. program at Johns Hopkins University. He received his M.S.E. degree in Mechanical Engineering/Robotics from Johns Hopkins University in 2015. Before joining the Johns Hopkins University, Joshua received a B.Sc. degree in Mechanical Engineering from Changsha University of Science and Technology, China, in 2013. His research interests are medical robotics, mechatronics system design, and computer-integrated surgical systems.